The Astrophysical Journal Supplement Series, 233:18 (31pp), 2017 December https://doi.org/10.3847/1538-4365/aa94cb

SkyNet: A Modular Nuclear Reaction Network Library

Jonas Lippuner[1,2,3,4] and Luke F. Roberts[5,6]
[1] TAPIR, Walter Burke Institute for Theoretical Physics, California Institute of Technology, Pasadena, CA 91125, USA; jlippuner@lanl.gov
[2] CCS-2, Los Alamos National Laboratory, P.O. Box 1663, Los Alamos, NM 87545, USA
[3] Center for Nonlinear Studies, Los Alamos National Laboratory, P.O. Box 1663, Los Alamos, NM 87545, USA
[4] Center for Theoretical Astrophysics, Los Alamos National Laboratory, P.O. Box 1663, Los Alamos, NM, 87545, USA
[5] National Superconducting Cyclotron Laboratory, Michigan State University, East Lansing, MI 48824, USA
[6] Department of Physics and Astronomy, Michigan State University, East Lansing, MI 48824, USA
Received 2017 June 19; revised 2017 October 16; accepted 2017 October 17; published 2017 December 5

Abstract

Almost all of the elements heavier than hydrogen that are present in our solar system were produced by nuclear burning processes either in the early universe or at some point in the life cycle of stars. In all of these environments, there are dozens to thousands of nuclear species that interact with each other to produce successively heavier elements. In this paper, we present SkyNet, a new general-purpose nuclear reaction network that evolves the abundances of nuclear species under the influence of nuclear reactions. SkyNet can be used to compute the nucleosynthesis evolution in all astrophysical scenarios where nucleosynthesis occurs. SkyNet is free and open source, and aims to be easy to use and flexible. Any list of isotopes can be evolved, and SkyNet supports different types of nuclear reactions. SkyNet is modular so that new or existing physics, like nuclear reactions or equations of state, can easily be added or modified. Here, we present in detail the physics implemented in SkyNet with a focus on a self-consistent transition to and from nuclear statistical equilibrium to non-equilibrium nuclear burning, our implementation of electron screening, and coupling of the network to an equation of state. We also present comprehensive code tests and comparisons with existing nuclear reaction networks. We find that SkyNet agrees with published results and other codes to an accuracy of a few percent. Discrepancies, where they exist, can be traced to differences in the physics implementations.

Key words: methods: numerical – nuclear reactions, nucleosynthesis, abundances

1. Introduction

Nuclear and weak reactions play a crucial role in many astrophysical scenarios. Nuclear reactions typically occur at high temperatures and densities, because a large amount of energy is required to overcome the Coulomb repulsion between positively charged nuclei. Inside the cores of main-sequence stars, nuclear fusion converts hydrogen into helium, which releases nuclear binding energy as heat, keeping the star from collapsing (Bethe 1939). When massive stars undergo core collapse at the end of their lives, nuclear and weak reactions serve as important energy sinks and sources (neutrino cooling and heating). In core-collapse and Type Ia supernovae (SNe Ia), explosive nuclear burning mainly creates iron-group elements that are ejected into the interstellar medium (Nomoto et al. 1997; Woosley et al. 2002). According to our current understanding, a weak version of the rapid neutron capture process (r-process) can also occur (Wanajo 2013) in core-collapse supernovae. However, it appears that the full r-process that can synthesize all of the heavy elements predominantly happens during neutron star mergers (Freiburghaus et al. 1999b). Heavy elements up to bismuth can also be created in stars via the slow neutron capture process (s-process; Burbidge et al. 1957). Finally, when hydrogen and helium gas accretes onto a white dwarf, the accumulated material can undergo a thermonuclear explosion that creates a short-lived bright flash of light called a nova. If the accretor is a neutron star instead, the thermonuclear explosion results in an X-ray burst (José 2016, ch. 6) or a superburst (Strohmayer & Brown 2002).

To adequately understand these astrophysical objects and phenomena, one needs to account for the nuclear reactions that drive them. In some cases, reaction networks are mainly used to track the nuclear energy generation (e.g., Weaver et al. 1978; Müller 1986; Timmes et al. 2000). But in most cases, the evolution of the entire composition due to nuclear reactions is of interest. Because of the many ways that nuclei can react with each other to form other nuclides, the number of nuclear species that are relevant for many astrophysical processes ranges from dozens to thousands, and the number of nuclear reactions involved is hundreds to tens of thousands. For this reason, a large number of variables (i.e., nuclide abundances) that are coupled together by non-linear nuclear reaction rates (see Section 2) need to be evolved. Mathematically and computationally, the ensemble of coupled nuclear reactions is described by a nuclear reaction network.

Large-scale (several dozen species or more) nuclear reaction networks were first developed in the late 1960s and early 1970s (e.g., Truran et al. 1966, 1967; Arnett & Truran 1969; Woosley et al. 1973). These first networks were mainly for explosive nuclear burning in massive stellar evolution and supernovae, although earlier stellar evolution models also took nuclear reactions into account and evolved a handful of nuclear species (e.g., Hayashi et al. 1962; Hofmeister et al. 1964; Iben 1967). Early networks ranged in size from a few dozen to around a hundred species, with up to a few hundred reactions connecting the nuclei. Since then, nuclear reaction networks of different sizes have been used to study various astrophysical scenarios. Big bang nucleosynthesis calculations require the smallest networks with typically fewer than a dozen nuclear species, although some authors utilize much bigger networks of up to several dozen species (e.g., Wagoner 1973; Nollett & Burles 2000; Orlov et al. 2000; Coc et al. 2012; Cyburt et al. 2016). Networks with dozens to hundreds of species are employed in

stellar evolution codes (e.g., Arnett 1977; Weaver et al. 1978; Maeder & Meynet 2000; Paxton et al. 2011; Bressan et al. 2012; Jones et al. 2015). Similar-sized or larger (up to hundreds of species) networks are also used to compute explosive nucleosynthesis in SNe Ia (e.g., Thielemann et al. 1986a; Iwamoto et al. 1999; Hillebrandt et al. 2013; Seitenzahl et al. 2013; Leung et al. 2015), core-collapse supernovae (e.g., Thielemann et al. 1996; Limongi & Chieffi 2003; Heger & Woosley 2010; Harris et al. 2014), novae (e.g., Weiss & Truran 1990; José & Hernanz 1998; Iliadis et al. 2002; Starrfield et al. 2016), and X-ray bursts (e.g., Schatz et al. 2001; Woosley et al. 2004; Cyburt et al. 2010; Parikh et al. 2013).

The largest nuclear networks are needed to simulate neutron capture processes. For the s-process in massive stars, it may be sufficient to use a few hundred to about a thousand nuclei (e.g., Prantzos et al. 1990; Käppeler et al. 2011; Nishimura et al. 2017). Larger nuclear reaction networks (typically thousands of isotopes) have been used for r-process nucleosynthesis calculations in neutrino-driven winds from core-collapse supernovae (e.g., Woosley & Hoffman 1992; Hoffman et al. 1997; Freiburghaus et al. 1999a; Arcones et al. 2010; Farouqi et al. 2010; Roberts et al. 2010; Wanajo 2013), in the jets of magnetorotational core-collapse supernovae (e.g., Winteler et al. 2012; Nishimura et al. 2015), in the dynamical ejecta of neutron star mergers (e.g., Freiburghaus et al. 1999b; Goriely et al. 2011; Bauswein et al. 2013; Wanajo et al. 2014; Eichler et al. 2015; Just et al. 2015; Fernández et al. 2017), in accretion disk ejecta following neutron star mergers (e.g., Surman et al. 2008; Perego et al. 2014; Martin et al. 2015; Lippuner et al. 2017), and in broader astrophysical contexts (e.g., Panov et al. 1995, 2001; Blinnikov & Panov 1996; Mumpower et al. 2012).

To evolve a nuclear reaction network, the rates of all reactions in the network are required. Most reaction rates, e.g., interactions between two or more nuclides, depend strongly on the energies of the incoming particles, due to Coulomb barrier penetration, resonances in the compound nuclear system, and other effects (e.g., Clayton 1968, Section 4). The rates of reactions only involving a single particle in the entrance channel, like β-decays and spontaneous fission, are constant.[7] Some reaction rates involving nuclides sufficiently close to the valley of stability can be measured experimentally as a function of energy, although in many cases astrophysical reactions occur at energies that are much lower than the experimentally accessible energy ranges (e.g., Rolfs & Rodney 1988, Section 4). Furthermore, most astrophysical processes involve unstable nuclei that may be very far away from stability and are not experimentally accessible for rate measurements. Therefore, theoretical models are necessary to compute the reaction rates needed by the reaction network (e.g., Cyburt et al. 2010). The Hauser–Feshbach approach, which assumes that the reactants form a single compound nucleus that subsequently decays into the reaction products, has been used extensively to compute nuclear reaction rates for astrophysics applications (e.g., Hauser & Feshbach 1952; Holmes et al. 1976; Woosley et al. 1978; Thielemann et al. 1986b; Rauscher & Thielemann 2000; Goriely et al. 2008).

Nuclear reaction networks also require the properties, such as masses and internal nuclear partition functions (e.g., Arcones & Martínez-Pinedo 2011; Brett et al. 2012; Mendoza-Temis et al. 2015; Mumpower et al. 2016), of all nuclides evolved in the network. These properties are needed to compute nuclear statistical equilibrium (NSE) and inverse reaction rates (see Section 2.3), as well as β-decay rates. Some of these nuclear properties, such as the masses, also enter the theoretical reaction rate calculations. Since many of the nuclides of interest are extremely unstable, special radioactive ion beam facilities are needed to produce and measure these exotic nuclei (see, e.g., Lunney et al. 2003; Schatz 2013; Mumpower et al. 2016 and references therein). Current radioactive beam facilities have made great progress in measuring unstable nuclei and new facilities or upgrades to current facilities are being built and planned. These new facilities will extend the reach to more exotic nuclei that are highly relevant to nuclear astrophysics scenarios (e.g., Schatz 2013, 2016; Mumpower et al. 2016). For the foreseeable future, however, it is necessary to use theoretical models to compute nuclear masses and β-decay properties for a large fraction of the nuclear species present in r-process networks (e.g., Lunney et al. 2003; Möller et al. 2003; Mumpower et al. 2016 and references therein).

Many authors who use nuclear reaction networks do not make the code of these networks publicly available. This makes it hard to reproduce and verify published results and also presents a barrier to new researchers joining the field since they first have to write their own nuclear reaction network. Notable exceptions of nuclear reaction networks that are publicly available are the various networks by Timmes (1999),[8] XNet by Hix & Thielemann (1999),[9] and NucNet by Meyer & Adams (2007).[10] In this paper, we present a new nuclear reaction network called SkyNet that is publicly available as an open-source software at https://bitbucket.org/jlippuner/skynet (Lippuner & Roberts 2017b). This paper is based on version 1.0 of SkyNet (Lippuner & Roberts 2017a).

SkyNet was initially designed for evolving large reaction networks for r-process nucleosynthesis calculations, but thanks to its modularity and flexibility, SkyNet can easily be used for nucleosynthesis computations in many other astrophysical situations. Besides correctness, the main design goals behind SkyNet are usability and flexibility, making SkyNet an easy to use and versatile nuclear reaction network that is available for anyone to use. SkyNet can evolve an arbitrary set of nuclear species under various different types of nuclear reactions (Section 5.2). SkyNet can also compute NSE compositions (Section 2.3) and switch between evolving NSE and the full network in an automated and self-consistent way (Section 3.4). SkyNet contains electron screening corrections (Section 4) and an equation of state (EOS) that takes the entire composition into account (Appendix A.2). For ease of use, SkyNet can be used from within Python (Section 5), and SkyNet can make movies of the nucleosynthesis evolution (see examples at http://stellarcollapse.org/lippunerroberts2015).

SkyNet has been used for r-process nucleosynthesis calculations in different scenarios by various authors: Lippuner & Roberts (2015), Radice et al. (2016), Roberts et al. (2017), Lippuner et al. (2017), Siegel & Metzger (2017), Vlasov et al. (2017), and Fernández et al. (2017). Here, we discuss the physics used in SkyNet, provide details on how it is

[7] Strictly speaking, β-decay rates are only constant in vacuum. In the medium, electron phase-space blocking introduces a dependency on the electron chemical potential and temperature (e.g., Arnett 1996, Section 11.3).

[8] http://cococubed.asu.edu/code_pages/burn.shtml

[9] http://eagle.phys.utk.edu/xnet/trac

[10] https://sourceforge.net/projects/nucnet-tools

implemented, and perform code tests and comparisons with other nuclear reaction networks.

This paper is organized as follows. In Section 2, we derive the equations that govern nuclear abundance evolution and equilibrium. Section 3 deals with the numerical implementation of the reaction network. We discuss in detail the electron screening corrections implemented in SkyNet in Section 4. In Section 5, we describe code implementation details. The code tests and comparisons are the subject of Section 6. We summarize in Section 7. In Appendix A, we briefly present the physics of an ideal Boltzmann gas and the EOS implemented in SkyNet. We show how SkyNet computes NSE in Appendix B, and in Appendix C we discuss neutrino interaction reactions.

Throughout this paper, we set the Boltzmann constant $k_B = 1$ (i.e., all temperatures are measured in energy), the speed of light $c = 1$, and the reduced Planck constant $\hbar = 1$.

2. Nuclear Reaction Network Basics

Astrophysical nuclear reaction networks track the composition of a system containing many species of nuclei, electrons, positrons, photons, and sometimes neutrinos. Essentially, they evolve the numbers of different nuclei in a system given a set of reactions and rates for those reactions that transmute nuclei into other nuclei. Although it is straightforward to heuristically write down a system of rate equations (Hix & Meyer 2006), it is useful to start from kinetic theory to tie the rate equations to the microscopic processes driving the nuclear transmutations.

2.1. Kinetic Theory

Consider a homogeneous system of different species of particles (including nuclei, electrons, etc.) connected by a set of interactions, a subset of which changes particles of one type into another. A reaction indexed by n converts a set of reactants into a set of products and vice versa. We write reaction n as

$$\sum_{\alpha\in\tilde{\mathcal{R}}_n} [\alpha] \rightleftharpoons \sum_{\beta\in\tilde{\mathcal{P}}_n} [\beta], \tag{1}$$

where $[\alpha]$ is a reactant, $[\beta]$ is a product, and $\tilde{\mathcal{R}}_n$ and $\tilde{\mathcal{P}}_n$ are the sets of all reactants and products, respectively. We emphasize that all particles are individually labeled, even if they are of the same species. For example, for the reaction $^{12}\mathrm{C} + {}^{4}\mathrm{He} \rightleftharpoons {}^{16}\mathrm{O} + \gamma$, we have $\tilde{\mathcal{R}}_n = \{0, 1\}$ and $\tilde{\mathcal{P}}_n = \{2, 3\}$ with $[0] = {}^{12}\mathrm{C}$, $[1] = {}^{4}\mathrm{He}$, $[2] = {}^{16}\mathrm{O}$, and $[3] = \gamma$. For $^{12}\mathrm{C} + {}^{12}\mathrm{C} \rightleftharpoons {}^{20}\mathrm{Ne} + {}^{4}\mathrm{He} + \gamma$, we have $\tilde{\mathcal{R}}_n = \{0, 1\}$ and $\tilde{\mathcal{P}}_n = \{2, 3, 4\}$ with $[0] = [1] = {}^{12}\mathrm{C}$, $[2] = {}^{20}\mathrm{Ne}$, $[3] = {}^{4}\mathrm{He}$, and $[5] = \gamma$. Note that reaction n includes both the forward process (going from reactants to products) and the inverse process (going from products to reactants). Of course, it is arbitrary which set we call reactants and which we call products. In the following, we use the convention that if we consider particle $[\epsilon]$, then we choose the reactants and products such that $\epsilon \in \tilde{\mathcal{R}}_n$.

If the particles are uncorrelated, the system can be described in terms of the individual particle distribution functions f_ϵ. Kinetic theory then gives the time evolution of the distribution functions as (e.g., Danielewicz & Bertsch 1991; Buss et al. 2012)

$$\begin{aligned}
&\left(\partial_t + \frac{\partial k_\epsilon^0}{\partial \boldsymbol{k}_\epsilon}\cdot\nabla\right) f_\epsilon\left(x^\mu, k_\epsilon^\mu\right) \\
&\quad = -f_\epsilon \sum_n \mathcal{N}_n^{\text{forward}} \left[\prod_{\alpha\in\tilde{\mathcal{R}}_n,\alpha\neq\epsilon} \int_{[\alpha]} f_\alpha\right]\left[\prod_{\beta\in\tilde{\mathcal{P}}_n} \int_{[\beta]} (1 \pm f_\beta)\right] \\
&\quad\quad \times \delta^4\left(\sum_{\alpha\in\tilde{\mathcal{R}}_n} k_\alpha^\mu - \sum_{\beta\in\tilde{\mathcal{P}}_n} k_\beta^\mu\right) \boldsymbol{r}_n(k_{\{\alpha\}}^\mu, k_{\{\beta\}}^\mu) \\
&\quad\quad + (1 \pm f_\epsilon) \sum_n \mathcal{N}_n^{\text{inverse}} \left[\prod_{\alpha\in\tilde{\mathcal{R}}_n,\alpha\neq\epsilon} \int_{[\alpha]} (1 \pm f_\alpha)\right] \\
&\quad\quad \times \left[\prod_{\beta\in\tilde{\mathcal{P}}_n} \int_{[\beta]} f_\beta\right] \delta^4\left(\sum_{\alpha\in\tilde{\mathcal{R}}_n} k_\alpha^\mu - \sum_{\beta\in\tilde{\mathcal{P}}_n} k_\beta^\mu\right) \boldsymbol{r}_n(k_{\{\alpha\}}^\mu, k_{\{\beta\}}^\mu),
\end{aligned} \tag{2}$$

where the sum over n only includes interactions that have $\epsilon \in \tilde{\mathcal{R}}_n$. $\mathcal{N}_n^{\text{forward}}$ and $\mathcal{N}_n^{\text{inverse}}$ are factors that avoid double counting if the interaction involves multiple particles of the same species. These will be defined later after introducing some additional notation. $k_\epsilon^\mu = (k_\epsilon^0, \boldsymbol{k}_\epsilon)$ is the four-momentum of particle $[\epsilon]$ and δ^4 is the four-dimensional delta function that enforces conservation of momentum. $\boldsymbol{r}_n$ denotes the differential rate of reaction n. The upper $(+)$ signs are for bosons and the lower $(-)$ signs are for fermions. We use the shorthand

$$\int_{[\epsilon]} = g_\epsilon \int \frac{d^3k_\epsilon}{(2\pi)^3} \tag{3}$$

for the phase-space integral of particle $[\epsilon]$, where g_ϵ is the spin degeneracy factor. Note that the differential rate $\boldsymbol{r}_n$ depends on the momenta of all particles (reactants and products). The first sum over n in Equation (2) is due to the forward process of interaction n, and the second sum over n is due to the inverse process. The second sum over n is required by the assumption of reversibility of interactions. Note that the differential rate is the same for the forward and inverse processes, and the delta function is also identical since it is an even function.

For simple interactions, e.g., weak interactions between nucleons and neutrinos, $\boldsymbol{r}$ is given by

$$\boldsymbol{r}(k_{\{\alpha\}}^\mu, k_{\{\beta\}}^\mu) = (2\pi)^4 \frac{\langle|\mathcal{T}^2|\rangle}{2\prod_{\alpha\in\tilde{\mathcal{R}}} 2k_\alpha^0 \prod_{\beta\in\tilde{\mathcal{P}}} 2k_\beta^0}, \tag{4}$$

where $\langle|\mathcal{T}^2|\rangle$ is the spin-averaged reduced matrix element (averaged over the spins of both the initial and final states) of the interaction (see Brown & Sawyer 1997 for a discussion in the non-relativistic context). For more complicated interactions between nuclei, $\boldsymbol{r}_n$ could include transition probabilities between multiple internal states.

Generally, a reaction network only evolves some subset of the particles present in the system. For instance, photons are assumed to be in equilibrium at all times, and the electron and positron densities are determined by charge neutrality, so their number evolution does not need to be tracked explicitly. Therefore, it is useful to define the part of a reaction that only

includes particles that will be tracked by the network as

$$\sum_{j\in\mathcal{R}_n} N_j^n[j] \rightleftharpoons \sum_{l\in\mathcal{P}_n} N_l^n[l], \tag{5}$$

where $[j]$ is a reactant species, $[l]$ is a product species, and $\mathcal{R}_n$ and $\mathcal{P}_n$ (without tildes) are the sets of distinct reactant species and product species including only species that are present in the network, respectively. The positive integers N_j^n and N_l^n are the numbers of particles of reactant species $[j]$ destroyed and the number of particles of product species $[l]$ created, respectively. Note that we use Latin indices to refer to particle species, and we use Greek indices to refer to individual particles. In the earlier example of $^{12}\mathrm{C} + {}^4\mathrm{He} \rightleftharpoons {}^{16}\mathrm{O} + \gamma$, we now have $\mathcal{R}_n = \{0, 1\}$ and $\mathcal{P}_n = \{2\}$ with $[0] = {}^{12}\mathrm{C}$, $[1] = {}^4\mathrm{He}$, $[2] = {}^{16}\mathrm{O}$, and $N_0^n = N_1^n = N_2^n = 1$. The photon that is contained in $\tilde{\mathcal{P}}_n$ is not in $\mathcal{P}_n$, because it is not explicitly tracked in the network. Similarly, for $^{12}\mathrm{C} + {}^{12}\mathrm{C} \rightleftharpoons {}^{20}\mathrm{Ne} + {}^4\mathrm{He} + \gamma$, we get $\mathcal{R}_n = \{0\}$ and $\mathcal{P}_n = \{1, 2\}$ with $[0] = {}^{12}\mathrm{C}$, $[1] = {}^{20}\mathrm{Ne}$, and $[2] = {}^4\mathrm{He}$. But in this case, we have $N_0^n = 2$ and $N_1^n = N_2^n = 1$.

Since Equation (2) essentially counts the pairs (or triplets, etc.) of reactants that can interact with each other (or pairs of products for the inverse process), we need to be careful to avoid double counting if the interaction involves multiple particles of the same species. If two distinct particles [0] and [1] interact with each other, then there are $N_0 N_1$ distinct pairs, where N_0 and N_1 are the numbers of particles [0] and [1], respectively. But if we have N particles of the same species where two react with each other, then the total number of distinct pairs is $N^2/2$ and not N^2. If it is three identical particles that react with each other, the number of distinct triplets is $N^3/6$, since there are $6 = 3!$ ways to order a set of three items. Thus, we need to divide by the product of factorials of the multiplicities of the interacting particle species. With the notation introduced in Equation (5), we can write this as

$$\mathcal{N}_n^{\text{forward}} = \prod_{j\in\mathcal{R}_n} \frac{1}{N_j^n!} \quad \text{and} \quad \mathcal{N}_n^{\text{inverse}} = \prod_{l\in\mathcal{P}_n} \frac{1}{N_l^n!}. \tag{6}$$

We can now define the reaction rate of the forward process as

$$\begin{aligned}\lambda_n = n_{\mathrm{B}}^{-1}\mathcal{N}_n^{\text{forward}} &\left[\prod_{j\in\mathcal{R}_n}\left(\frac{n_{\mathrm{B}}}{n_j}\right)^{N_j^n}\right]\left[\prod_{\alpha\in\tilde{\mathcal{R}}_n}\int_{[\alpha]} f_\alpha\right] \\ &\times\left[\prod_{\beta\in\tilde{\mathcal{P}}_n}\int_{[\beta]}(1\pm f_\beta)\right] \\ &\times\delta^4\left(\sum_{\alpha\in\tilde{\mathcal{R}}_n} k_\alpha^\mu - \sum_{\beta\in\tilde{\mathcal{P}}_n} k_\beta^\mu\right) r_n(k_{\{\alpha\}}^\mu, k_{\{\beta\}}^\mu),\end{aligned} \tag{7}$$

where

$$n_m = \int_{[m]} f_m = g_m \int \frac{d^3k_m}{(2\pi)^3} f_m \tag{8}$$

is the number density of species $[m]$ and n_{B} is the total baryon number density. λ_n is the forward process term of reaction n on the right-hand side of Equation (2) integrated over the phase space of particle $[\epsilon]$ and normalized by the number densities of the particles in the entrance channel. The reaction rate is just the rate at which a reaction proceeds per particle in the entrance channel. These reaction rates are only non-zero when the particles in the entrance channel differ from those in the exit channel. The other interactions included in Equation (2) may change the momentum space distribution of the particles in the system, but they cannot change the total number of particles of any species. The reaction rate of the inverse process λ_n' is defined analogously to Equation (7) with the reactant and product sets switched.

Now, the standard reaction network equations follow from integrating over the phase space of particle $[\epsilon]$ in Equation (2) to find

$$\begin{aligned}&\partial_t n_\epsilon + \nabla\cdot(\langle\boldsymbol{v}_\epsilon\rangle n_\epsilon) \\ &\quad = \sum_n\left[-\lambda_n n_{\mathrm{B}}^{1-N_{\mathcal{R}}^n}\prod_{j\in\mathcal{R}_n} n_j^{N_j^n} + \lambda_n' n_{\mathrm{B}}^{1-N_{\mathcal{P}}^n}\prod_{l\in\mathcal{P}_n} n_l^{N_l^n}\right].\end{aligned} \tag{9}$$

Here, $\langle\boldsymbol{v}_\epsilon\rangle = (2\pi)^{-3} n_\epsilon^{-1}\int d^3k_\epsilon f_\epsilon\,\partial_{\boldsymbol{k}_\epsilon} k_\epsilon^0$ is the average velocity of particle $[\epsilon]$, and we define

$$N_{\mathcal{R}}^n = \sum_{j\in\mathcal{R}_n} N_j^n \quad \text{and} \quad N_{\mathcal{P}}^n = \sum_{l\in\mathcal{P}_n} N_l^n. \tag{10}$$

Note that the left-hand side of Equation (9) is for an individual particle, not a particle species, but we need the evolution equations for the particle species. A reaction n that involves N_i^n particles of species $[i]$ will contribute the right-hand side in Equation (9) N_i^n times to the derivative of n_i and so we multiply the right-hand side by N_i^n. Furthermore, due to the symmetry between the forward and inverse processes in Equation (9), it makes sense to treat the forward and inverse processes separately. So far, we have indexed reactions with n and each reaction consisted of the forward and inverse directions. Let us now index reactions with α, where the forward and inverse processes are counted separately. The set of reactions $\{\alpha\}$ is thus twice as big as the set of reactions $\{n\}$, although some inverse reactions may be ignored since they are extremely unlikely to occur. Equation (9) thus becomes

$$\begin{aligned}&\partial_t n_i + \nabla\cdot(\langle\boldsymbol{v}_i\rangle n_i) \\ &\quad = \sum_\alpha \lambda_\alpha(-R_i^\alpha + P_i^\alpha) N_i^\alpha n_{\mathrm{B}}^{1-N_{\mathcal{R}}^\alpha}\prod_{m\in\mathcal{R}_\alpha} n_m^{N_m^\alpha},\end{aligned} \tag{11}$$

where

$$R_i^\alpha = \begin{cases}1 & \text{if } i \in \mathcal{R}_\alpha \\ 0 & \text{otherwise}\end{cases} \quad \text{and} \quad P_i^\alpha = \begin{cases}1 & \text{if } i \in \mathcal{P}_\alpha \\ 0 & \text{otherwise.}\end{cases} \tag{12}$$

For every interaction n, there is a forward reaction α that has $\lambda_\alpha = \lambda_n$, $\mathcal{R}_\alpha = \mathcal{R}_n$, and $N_{\mathcal{R}}^\alpha = N_{\mathcal{R}}^n$. For that reaction, Equation (11) contributes the forward part of Equation (9) with a multiplicative factor $(-R_i^\alpha + P_i^\alpha)N_i^\alpha = -N_i^\alpha$, since N_i^α particles of species $[i]$ are destroyed. Similarly, there is an inverse reaction α' for the same interaction n that has $\lambda_{\alpha'} = \lambda_n'$, $\mathcal{R}_{\alpha'} = \mathcal{P}_n$, and $N_{\mathcal{R}}^{\alpha'} = N_{\mathcal{P}}^n$. This reaction contributes the inverse part of Equation (9) with a factor of $(-R_i^\alpha + P_i^\alpha)N_i^\alpha = N_i^\alpha$, since N_i^α particles of species $[i]$ are

created in the inverse reaction. Note that $N_m^{\alpha} = N_m^{\alpha'} = N_m^n$ for all reactants and products $[m]$.

Finally, it is useful to define the abundance Y_i as

$$Y_i \equiv \frac{n_i}{n_\mathrm{B}} = \frac{N_i/V}{N_\mathrm{B}/V} = \frac{N_i}{N_\mathrm{B}}, \tag{13}$$

where V is the volume of the fluid element, and N_i and N_B are the total numbers of particles of species $[i]$ and baryons, respectively. Since the number density n_i of species $[i]$ changes with both the number of particles of species $[i]$ and the total volume of the system, which is often changing in astrophysical systems undergoing nuclear burning, it is convenient to evolve the abundances Y_i instead of the number densities n_i. Assuming that all of the species move as a single fluid, i.e., $\langle \boldsymbol{v}_i \rangle = \boldsymbol{v}$, and using the Lagrangian time derivative, $d/dt = \partial_t + \boldsymbol{v} \cdot \nabla$, we find

$$\begin{aligned}
\frac{dY_i}{dt} &= (\partial_t + \boldsymbol{v} \cdot \nabla)\left(\frac{n_i}{n_\mathrm{B}}\right) \\
&= \frac{1}{n_\mathrm{B}}\left[\partial_t n_i - \frac{n_i}{n_\mathrm{B}}\partial_t n_\mathrm{B} + \nabla \cdot (\boldsymbol{v} n_i)\right. \\
&\quad \left. - n_i \nabla \cdot \boldsymbol{v} - \frac{n_i}{n_\mathrm{B}}(\nabla \cdot (\boldsymbol{v} n_\mathrm{B}) - n_\mathrm{B} \nabla \cdot \boldsymbol{v})\right] \\
&= \frac{1}{n_\mathrm{B}}\left[\partial_t n_i + \nabla \cdot (\boldsymbol{v} n_i) - \frac{n_i}{n_\mathrm{B}}(\partial_t n_\mathrm{B} + \nabla \cdot (\boldsymbol{v} n_\mathrm{B}))\right] \\
&= \frac{1}{n_\mathrm{B}}[\partial_t n_i + \nabla \cdot (\boldsymbol{v} n_i)],
\end{aligned} \tag{14}$$

where we used the identity $\boldsymbol{v} \cdot \nabla f = \nabla \cdot (\boldsymbol{v} f) - f \nabla \cdot \boldsymbol{v}$ and the baryon number continuity equation $\partial_t n_\mathrm{B} + \nabla \cdot (\boldsymbol{v} n_\mathrm{B}) = 0$. But since $\langle \boldsymbol{v}_i \rangle = \boldsymbol{v}$, the above is the left-hand side of Equation (11) and so we get

$$\frac{dY_i}{dt} = \sum_\alpha \lambda_\alpha (-R_i^\alpha + P_i^\alpha) N_i^\alpha \prod_{m \in \mathcal{R}_\alpha} Y_m^{N_m^\alpha}, \tag{15}$$

which is the familiar abundance evolution equation (e.g., Hix & Thielemann 1999). Essentially, for a given set of rates λ_α, SkyNet solves this coupled, first-order, non-linear system of equations.

Even though it might look somewhat complicated, Equation (15) is very easy to understand. It says that the total time derivative of a species $[i]$ is the sum over all reactions that involve that species, and each reaction contributes a term consisting of the reaction rate multiplied by the abundances of the reactants and a factor that gives the number of particles of species $[i]$ destroyed or created in the reaction. For example, for the forward and inverse reactions $^{12}\mathrm{C} + {}^{4}\mathrm{He} \rightleftharpoons {}^{16}\mathrm{O}$, Equation (15) says

$$\frac{dY_{^{12}\mathrm{C}}}{dt} = -\lambda_\alpha Y_{^{12}\mathrm{C}} Y_{^{4}\mathrm{He}} + \lambda_{\alpha'} Y_{^{16}\mathrm{O}} + \ldots, \tag{16}$$

$$\frac{dY_{^{4}\mathrm{He}}}{dt} = -\lambda_\alpha Y_{^{12}\mathrm{C}} Y_{^{4}\mathrm{He}} + \lambda_{\alpha'} Y_{^{16}\mathrm{O}} + \ldots, \tag{17}$$

$$\frac{dY_{^{16}\mathrm{O}}}{dt} = \lambda_\alpha Y_{^{12}\mathrm{C}} Y_{^{4}\mathrm{He}} - \lambda_{\alpha'} Y_{^{16}\mathrm{O}} + \ldots. \tag{18}$$

For the reactions $^{12}\mathrm{C} + {}^{12}\mathrm{C} \rightleftharpoons {}^{20}\mathrm{Ne} + {}^{4}\mathrm{He}$, we get

$$\frac{dY_{^{12}\mathrm{C}}}{dt} = -2\lambda_\alpha Y_{^{12}\mathrm{C}}^2 + 2\lambda_{\alpha'} Y_{^{20}\mathrm{Ne}} Y_{^{4}\mathrm{He}} + \ldots, \tag{19}$$

$$\frac{dY_{^{20}\mathrm{Ne}}}{dt} = \lambda_\alpha Y_{^{12}\mathrm{C}}^2 - \lambda_{\alpha'} Y_{^{20}\mathrm{Ne}} Y_{^{4}\mathrm{He}} + \ldots, \tag{20}$$

$$\frac{dY_{^{4}\mathrm{He}}}{dt} = \lambda_\alpha Y_{^{12}\mathrm{C}}^2 - \lambda_{\alpha'} Y_{^{20}\mathrm{Ne}} Y_{^{4}\mathrm{He}} + \ldots. \tag{21}$$

2.2. Reaction Rates and Velocity-averaged Cross Sections

Specializing to astrophysical systems consisting of a range of nuclear species, scattering reactions mediated by the nuclear and electromagnetic forces bring particles into thermal equilibrium at temperature T on a much shorter timescale than nuclear reactions bring particles into chemical equilibrium. In that case, the distribution functions only depend on temperature and the chemical potentials, i.e., $f_i = f_i(T, \mu_i)$. As written, the rates defined in Equation (7) depend on the momentum space distribution functions of the particles involved in the reaction and may be quite complicated. Nevertheless, in thermal equilibrium, the reaction rates depend only on the parameters of the distribution functions, i.e., $\lambda_\alpha = \lambda_\alpha(T, n_\mathrm{B}, \mu_{\{m\}})$, where the index m ranges over reactant and products.

If all of the particles involved in a reaction obey Boltzmann statistics or are photons with chemical potential zero, then we find that $\lambda_\alpha = \lambda_\alpha(T, n_\mathrm{B})$ does not depend on the chemical potentials of the particles. This is because we can set the blocking factors $(1 \pm f_i)$ of Boltzmann particles to 1, since quantum effects for Boltzmann particles are negligible. For Boltzmann particles, we have $n_i \propto \exp(\mu_i/T)$ and $f_i \propto \exp(\mu_i/T)$, which means that the dependence on μ_i cancels for Boltzmann particles because every f_α in Equation (7) is divided by an n_α.[11] In most astrophysical scenarios, we can assume that the distribution functions f_i follow a thermal Maxwell–Boltzmann distribution, so the rates of reactions involving only nuclei and photons only depend on the temperature and density.

Nuclei can also undergo weak interactions that may involve leptons with non-zero chemical potentials. The leptons are generally not evolved in the network, but rather the electron (and positron) chemical potential is determined by the requirement of charge neutrality or by the number of electrons per baryon Y_e. Neutrinos are also not evolved in reaction networks since their distribution functions are often non-thermal in astrophysical scenarios in which they play a role. Therefore, weak interaction rates have a dependence $\lambda_{\alpha,\mathrm{weak}} = \lambda_{\alpha,\mathrm{weak}}(T, n_\mathrm{B}, Y_e, f_{\{\nu\}})$, where $f_{\{\nu\}}$ are the externally specified neutrino distribution functions of the relevant neutrino species (see Appendix C). However, weak decay rates of nuclei are just constants when final state blocking by leptons can be safely ignored.

[11] Actually, the f_α are divided by $n_j^{N_j^n}$, but this is just an n_α for every particle of species $[j]$.

For two-particle reactions, it is common to define the cross-section as (Peskin & Schroeder 1995, Section 4)

$$\sigma_\alpha(k_1^\mu - k_2^\mu) = \frac{1}{v_{\rm rel}}\left[\prod_{l\in\mathcal{P}_\alpha}\int_{[l]}\right] \times \delta^4\left(k_1^\mu + k_2^\mu - \sum_{l\in\mathcal{P}_\alpha} k_l^\mu\right) r_\alpha(k_1^\mu, k_2^\mu, k_{\{l\}}^\mu), \tag{22}$$

where $v_{\rm rel}$ is the relative velocity between particles [1] and [2]. Adopting the viewpoint that the $[i]$ are stationary targets and the $[j]$ are incoming projectiles impinging on the targets, the cross-section σ_α can be interpreted as (e.g., Clayton 1968, Section 4)

$$\sigma_\alpha = \frac{\text{number of reactions per second per target}[i]}{\text{flux of incoming projectiles }[j]} = \frac{R_{i,j}/(n_i V)}{v_{\rm rel} n_j} = \frac{r_{i,j}}{v_{\rm rel} n_i n_j}, \tag{23}$$

where $R_{i,j}$ is the number of reactions per second, $r_{i,j} = R_{i,j}/V$ is the number of reactions per second per volume, and n_i, n_j are the number densities of $[i]$ and $[j]$. Assuming Boltzmann statistics so that $(1 \pm f_l) \to 1$ for the products, Equation (7) gives

$$\lambda_\alpha = \mathcal{N}_\alpha n_{\rm B} \int_{[1]} \frac{f_1}{n_1} \int_{[2]} \frac{f_2}{n_2} v_{\rm rel}\sigma_\alpha = \mathcal{N}_\alpha n_{\rm B}\langle\sigma_\alpha v_{\rm rel}\rangle, \tag{24}$$

where $\mathcal{N}_\alpha$ is the double counting factor from Equation (6). Since the distribution functions are normalized by the densities of species [1] and [2], this expression shows that λ_α is proportional to the cross-section averaged over the relative velocities between the two particles (after transforming to the center of mass frame; see, e.g., Clayton 1968). Therefore, using Equation (23), one arrives at the standard relation between the reaction rate and the velocity-averaged cross-section (e.g., Clayton 1968, Section 4; Rolfs & Rodney 1988, Section 3),

$$r_{i,j} = n_{\rm B}^{-1}\lambda_\alpha n_1 n_2 = n_1 n_2 \mathcal{N}_\alpha \langle\sigma_\alpha v_{\rm rel}\rangle. \tag{25}$$

2.3. Nuclear Statistical Equilibrium (NSE) and Inverse Reaction Rates

Equation (2) shows that for every reaction, there is an inverse reaction. The relationship between the forward and reverse rates, which only depends on the density, temperature, and the internal properties of the nuclei, is generally called detailed balance. In some cases, for example for β-decays or fission reactions, the inverse reactions are extremely unlikely to occur and can be ignored. For other reactions, e.g., a neutron capture reaction, the inverse reaction can occur very frequently and sometimes even more often than the forward reaction. Thus, it is important to take inverse reactions into account. At temperatures of about 5 GK and above, inverse strong reactions such as photodissociation of nuclides can be in equilibrium with their forward reactions. In that case, the reaction is said to be in chemical equilibrium. For example, the reactions $^{196}\text{Au} + \text{n} \rightleftharpoons {}^{197}\text{Au} + \gamma$ and $^{20}\text{Ne} + \gamma \rightleftharpoons {}^{16}\text{O} + {}^{4}\text{He}$ can be in chemical equilibrium at sufficiently high temperatures. The situation of all strong reactions being in equilibrium is called NSE. This situation can also be thought of as an equilibrium between the reaction of forming a nucleus (Z, N) from Z free protons and N free neutrons, and its inverse reaction, namely, completely dissociating a nucleus (Z, N) into Z protons and N neutrons. In other words, if NSE holds, then the forward and inverse reactions,

$$(Z, N) \rightleftharpoons Z[\text{p}] + N[\text{n}], \tag{26}$$

are in equilibrium for all nuclides that are part of the composition. Of course, there are no reactions that directly create a nuclide (Z, N) out of Z protons and N neutrons. But there is a chain of strong reactions that connects (Z, N) to free neutrons and protons. So if all strong reactions are in equilibrium, then we effectively have the reactions shown above and they are also in equilibrium. When nucleons are in chemical equilibrium with all other nuclear species, the energetic cost of turning Z_i protons and N_i neutrons into a single nucleus must be zero, which requires

$$\mu_i = Z_i\mu_{\rm p} + N_i\mu_{\rm n}, \tag{27}$$

where μ_i is the chemical potential of species $[i]$.

When the composition moves into NSE, the forward and inverse strong reactions approach equilibrium. In order to ensure that the equilibrium composition determined by the forward and inverse reaction rates is the same as the NSE composition computed from the equality of the chemical potentials, we need to compute the inverse reaction rates directly from the forward rates and nuclide properties. Consider the reaction α and its inverse reaction α'. In equilibrium, each set of terms on the right-hand side of Equation (2) must be zero. Then, by the symmetry of the differential rate $\boldsymbol{r}_\alpha = \boldsymbol{r}_{\alpha'}$ and casting Equation (2) into Equation (9), we have

$$\lambda_\alpha \prod_{j\in\mathcal{R}_\alpha} Y_{j,\rm eq}^{N_j^\alpha} = \lambda_{\alpha'} \prod_{l\in\mathcal{P}_\alpha} Y_{l,\rm eq}^{N_l^\alpha}, \tag{28}$$

where $Y_{i,\rm eq}$ is the abundance of species $[i]$ in chemical equilibrium. For a Boltzmann gas, the abundance is given by (Equation (125))

$$Y_i = \frac{G_i(T)}{n_{\rm B}}\left(\frac{m_i T}{2\pi}\right)^{3/2}\exp[(\mu_i - m_i)/T], \tag{29}$$

where $G_i(T)$ is the internal partition function of species $[i]$ (see Equation (117)) and m_i is its rest mass. Substituting the above into Equation (28) yields

$$\frac{\lambda_{\alpha'}}{\lambda_\alpha} = \frac{\prod_{j\in\mathcal{R}_\alpha}[G_j/n_{\rm B}(m_j T/2\pi)^{3/2}]^{N_j^\alpha}}{\prod_{l\in\mathcal{P}_\alpha}[G_l/n_{\rm B}(m_l T/2\pi)^{3/2}]^{N_l^\alpha}} \exp\left[\frac{1}{T}\sum_{j\in\mathcal{R}_\alpha} N_j^\alpha(\mu_{j,\rm eq} - m_j) - \frac{1}{T}\sum_{l\in\mathcal{P}_\alpha} N_l^\alpha(\mu_{l,\rm eq} - m_l)\right]. \tag{30}$$

Since the forward and reverse reactions are in equilibrium, the chemical potentials on both sides are equal, hence

$$\sum_{j\in\mathcal{R}_\alpha} N_j^\alpha \mu_{j,\rm eq} = \sum_{l\in\mathcal{P}_\alpha} N_l^\alpha \mu_{l,\rm eq}, \tag{31}$$

and the chemical potentials in the exponential of Equation (30) cancel. Then, the inverse reaction rate $\lambda_{\alpha'}$ is

$$\lambda_{\alpha'}(T, \rho) = \lambda_{\alpha}(T, \rho)\, e^{-Q_{\alpha}/T}\Gamma_{\alpha}(T) M_{\alpha}^{3/2}\left(\frac{T}{2\pi}\right)^{3\Delta N_{\alpha}/2} n_{\mathrm{B}}^{-\Delta N_{\alpha}}, \quad (32)$$

where we define

$$Q_{\alpha} = \sum_{j\in\mathcal{R}_{\alpha}} N_j^{\alpha} m_j - \sum_{l\in\mathcal{P}_{\alpha}} N_l^{\alpha} m_l, \quad (33)$$

$$\Gamma_{\alpha}(T) = \frac{\prod_{j\in\mathcal{R}_{\alpha}} G_j(T)^{N_j^{\alpha}}}{\prod_{l\in\mathcal{P}_{\alpha}} G_l(T)^{N_l^{\alpha}}}, \quad (34)$$

$$M_{\alpha} = \frac{\prod_{j\in\mathcal{R}_{\alpha}} m_j^{N_j^{\alpha}}}{\prod_{l\in\mathcal{P}_{\alpha}} m_l^{N_l^{\alpha}}}, \quad (35)$$

$$\Delta N_{\alpha} = \sum_{j\in\mathcal{R}_{\alpha}} N_j^{\alpha} - \sum_{l\in\mathcal{P}_{\alpha}} N_l^{\alpha} = N_{\mathcal{R}}^{\alpha} - N_{\mathcal{P}}^{\alpha}. \quad (36)$$

Although the above is derived under the assumption that the abundances are such that the two reactions are in equilibrium, it still holds for any abundances because the reaction rates only depend on the temperature and density. In Appendix B, we show how calculating NSE is implemented in SkyNet.

3. Network Evolution

In this section, we focus on the specific implementation of the physics described in the previous section in SkyNet. In essence, evolving the reaction network means solving the large coupled system of first-order, non-linear ordinary differential equations ODEs given in Equation (15). But there are various other pieces that are needed to make the evolution robust and efficient, which are also discussed this section.

3.1. Implicit Integration Method

The system of ODEs (Equation (15)) we need to solve is extremely stiff because of the enormous range of reaction rates, which can span many orders of magnitude (e.g., Timmes 1999; Hix & Meyer 2006). Thus, an explicit integration method would be constrained to taking extremely small time steps. This is why nuclear reaction networks are typically integrated with an implicit method (e.g., Arnett & Truran 1969; Woosley et al. 1973; Timmes 1999; Winteler 2013; Longland et al. 2014). However, some authors have proposed various explicit methods specifically tuned to integrate stiff reaction networks (e.g., Feger 2011; Guidry 2012; Guidry & Harris 2013; Guidry et al. 2013a, 2013b; Brock et al. 2015). Currently, SkyNet uses the first-order implicit backward Euler method (e.g., Gear 1971; Hix & Thielemann 1999), but it is straightforward to implement higher-order implicit integration methods as well. We plan to do this in the future, since Timmes (1999) recommends using higher-order methods, such as the variable-order Bader–Deuflhard method (Bader & Deuflhard 1983). Let the vector $\boldsymbol{Y}(t) = Y_i(t)$ denote the composition at time t. If we want to take a time step Δt using the first-order implicit backward Euler method, we write

$$\begin{aligned}\dot{\boldsymbol{Y}}(t+\Delta t) &= \frac{\boldsymbol{Y}(t+\Delta t) - \boldsymbol{Y}(t)}{\Delta t} \\ \Leftrightarrow \mathbf{0} &= \dot{\boldsymbol{Y}}(\boldsymbol{x}, T(t+\Delta t), \rho(t+\Delta t)) - \frac{\boldsymbol{x} - \boldsymbol{Y}(t)}{\Delta t} \\ &= \boldsymbol{F}(\boldsymbol{x}, T(t+\Delta t), \rho(t+\Delta t)),\end{aligned} \quad (37)$$

where $\boldsymbol{x} = \boldsymbol{Y}(t+\Delta t)$ are the unknown abundances at the end of the time step we are trying to find and $\boldsymbol{Y}(t)$ are the known abundances at the beginning of the time step. $\dot{\boldsymbol{Y}}(\boldsymbol{Y}, T, \rho)$ is the function defined in Equation (15) that gives the time derivatives of the abundances as a function of a given set of abundances $\boldsymbol{Y}$, a temperature T, and density ρ. Note that we need to know the temperature T and density ρ as a function of time. The function $\boldsymbol{F}$ is simply the right-hand side of the above equation. We thus have a multidimensional root-finding problem $\mathbf{0} = \boldsymbol{F}(\boldsymbol{x}, T, \rho)$, where T and ρ are known functions of time. SkyNet uses the Newton–Raphson (NR) method to find the root. For every time step, the following iteration is performed to find the solution $\boldsymbol{x}$ to Equation (37):

$$\boldsymbol{x}_{n+1} = \boldsymbol{x}_n - [J_{\boldsymbol{F}}(\boldsymbol{x}_n)]^{-1}\boldsymbol{F}(\boldsymbol{x}_n, T(t+\Delta t), \rho(t+\Delta t)), \quad (38)$$

where the iteration starts with $\boldsymbol{x}_0 = \boldsymbol{Y}(t)$, the abundances from the previous time step, and

$$(J_{\boldsymbol{F}})_{ij} = \frac{\partial F_i}{\partial Y_j} = \frac{\partial \dot{Y}_i}{\partial Y_j} - \frac{\delta_{ij}}{\Delta t} \quad (39)$$

is the Jacobian matrix and δ_{ij} is the Kronecker delta. The partial derivatives $\partial \dot{Y}_i / \partial Y_j$ are computed from Equation (15) as

$$\begin{aligned}\frac{\partial \dot{Y}_i}{\partial Y_j} &= \sum_{\alpha} \lambda_{\alpha}(-R_i^{\alpha} + P_i^{\alpha}) N_i^{\alpha} \sum_{n\in\mathcal{R}_{\alpha}} \delta_{nj} \frac{N_n^{\alpha}}{Y_n} \prod_{m\in\mathcal{R}_{\alpha}} Y_m^{N_m^{\alpha}} \\ &= \sum_{\alpha} \lambda_{\alpha}(-R_i^{\alpha} + P_i^{\alpha}) N_i^{\alpha} R_j^{\alpha} N_j^{\alpha} Y_j^{N_j^{\alpha}-1} \prod_{m\in\mathcal{R}_{\alpha}, m\neq j} Y_m^{N_m^{\alpha}}.\end{aligned} \quad (40)$$

The size of the Jacobian matrix $J_{\boldsymbol{F}}$ is $N \times N$, where N is the number of nuclear species in the network. For large networks ($N \sim 8000$), inverting this large matrix can be quite costly, because the linear system in Equation (37) has to be solved for every NR iteration. Since the Jacobian matrix depends on the unknown abundances at the end of the time step, we have to recompute the Jacobian matrix after every NR iteration that updates our guess for the abundances at the end of the time step. Fortunately, however, the Jacobian matrix is very sparse (only 0.24% of the N^2 entries are non-zero for large networks), because most nuclear species are not directly connected by a single reaction. By exploiting the sparseness of the Jacobian, we drastically reduce the memory requirement to store the Jacobian and we can also use matrix solver packages that are specifically designed for sparse systems (see Section 5). The most expensive parts of the evolution are computing the Jacobian entries from Equation (40) and then solving the sparse linear system given by Equation (37). These two operations have to be performed at every NR iteration. The method for choosing the time step Δt and when to terminate the NR iteration will be discussed in Section 3.3.

3.2. Self-heating Evolution

In the previous section, we showed how SkyNet integrates the nuclear abundances forward in time if both the temperature and density are given as functions of time. In most applications, the density history $\rho(t)$ is given (for example, when SkyNet is used to post-process nucleosynthesis for tracer particles from a hydrodynamical simulation), but the temperature is not necessarily known as a function of time. Even if we do have a temperature history available, it most likely would not include heating due to the nuclear reactions that SkyNet evolves. But based on the kinetic theory description of the reaction network equations in Section 2.1, as well as the discussion of detailed balance in Section 2.3, it is clear that the reaction network and the thermodynamic state of the fluid are intimately related and need to be treated consistently. Therefore, we want the temperature to be evolved in the network under the influence of nuclear reactions, which release nuclear binding energy as heat. This is referred to as a self-heating network evolution (e.g., Freiburghaus et al. 1999b). We still require knowing the density as a function of time, though.

Recall the first law of thermodynamics,

$$dU = \delta Q - \delta W = \delta Q - PdV, \tag{41}$$

where dU is the infinitesimal change in internal energy, δQ is the infinitesimal heat added to the system from the surroundings, and δW is the infinitesimal mechanical work performed by the system. If the system expands or contracts, the work performed is $\delta W = PdV$, where P is the pressure and dV is the infinitesimal change in volume. We use the entropy S, volume V, and composition $\{N_k\}$ as our independent thermodynamic variables. Note that the index k ranges over all particles in the system, not just nuclides. The total differential of the internal energy is thus

$$\begin{aligned} dU &= \left(\frac{\partial U}{\partial S}\right)_{V,\{N_k\}} dS + \left(\frac{\partial U}{\partial V}\right)_{S,\{N_k\}} dV \\ &\quad + \sum_k \left(\frac{\partial U}{\partial N_k}\right)_{S,V,\{N_{l\neq k}\}} dN_k \\ &= TdS - PdV + \sum_k \mu_k dN_k, \end{aligned} \tag{42}$$

where T is the temperature and μ_k is the chemical potential of particle k. Equating Equations (41) and (42) yields

$$\delta Q = TdS + \sum_k \mu_k dN_k. \tag{43}$$

If we divide the above by N_B, the total number of baryons, and replace the infinitesimal changes by the differences of the quantities from one time step to the next (i.e., $\Delta X = X(t + \Delta t) - X(t)$), we find

$$\Delta q = T\Delta s + \sum_k \mu_k \Delta Y_k, \tag{44}$$

since $Y_k = N_k/N_\mathrm{B}$ (Equation (13)). Note that the sum over k includes all particles, and hence also electrons, which can be created or destroyed in weak nuclear reactions. Δq is the change in the heat per baryon due to external heating sources. Let $\dot{\epsilon}_\mathrm{ext}$ be an imposed external heating rate (per baryon), then

$$\Delta q = (\dot{\epsilon}_\mathrm{ext} - \dot{\epsilon}_\nu)\Delta t, \tag{45}$$

where $\dot{\epsilon}_\nu$ is the neutrino heating/cooling rate of the system on the environment given by Equation (191). Since we do not include neutrinos in the internal state of the system, the neutrino heating/cooling must be treated as an external source of heat. And because we define $\dot{\epsilon}_\nu$ as the heating/cooling on the environment, it has a minus sign in Equation (44). Combining Equation (44) with Equation (45) and solving for Δs yields

$$\begin{aligned} \Delta s &= \frac{\Delta q}{T} - \frac{1}{T}\sum_i \Delta Y_i(\mu_i + Z_i\mu_{e^-}) \\ &= (\dot{\epsilon}_\mathrm{ext} - \dot{\epsilon}_\nu)\frac{\Delta t}{T} \\ &\quad - \sum_i \Delta Y_i \left(\frac{m_i}{T} + \frac{Z_i\mu_{e^-}}{T} + \ln\left[\frac{n_i}{G_i(T)}\left(\frac{2\pi}{m_i T}\right)^{3/2}\right]\right), \end{aligned} \tag{46}$$

where we used Equation (125) and switched to index i that runs only over the nuclides. So, we explicitly include the contribution from the Z_i electrons that come with nuclide i. To make the rest mass terms in the sum closer to unity, we define the mass excess $\mathcal{M}_i$ as

$$\mathcal{M}_i = m_i - A_i m_u, \tag{47}$$

where A_i is the number of neutrons and protons of species i, and m_u is the atomic mass unit, defined such that the mass excess of ^{12}C is exactly 0 (i.e., $m_u = m_{^{12}\mathrm{C}}/12$). Since $Y_i = N_i/N_\mathrm{B}$ (with N_i being the number of particles of species $[i]$; see Equation (13)), we find

$$\sum_i Y_i A_i = \frac{1}{N_\mathrm{B}}\sum_i N_i A_i = \frac{N_\mathrm{B}}{N_\mathrm{B}} = 1, \tag{48}$$

because species $[i]$ is made up of A_i neutrons and protons, and hence A_i baryons. Thus, we have $\sum_i Y_i(t)A_i = 1$ for all times t, which is another way of saying that the total baryon number N_B is conserved. Using this, we find

$$\begin{aligned} \sum_i \Delta Y_i m_i &= \sum_i \Delta Y_i(\mathcal{M}_i + m_u A_i) \\ &= \sum_i \Delta Y_i \mathcal{M}_i + m_u\left(\sum_i Y_i(t + \Delta t)A_i - \sum_i Y_i(t)A_i\right) \\ &= \sum_i \Delta Y_i \mathcal{M}_i + m_u(1 - 1) = \sum_i \Delta Y_i \mathcal{M}_i. \end{aligned} \tag{49}$$

Using the above and the fact that $n_i = Y_i n_\mathrm{B}$, we can write Equation (46) as

$$\begin{aligned} \Delta s &= (\dot{\epsilon}_\mathrm{ext} - \dot{\epsilon}_\nu)\frac{\Delta t}{T} \\ &\quad - \sum_i \Delta Y_i \left(\frac{\mathcal{M}_i}{T} + \frac{Z_i\mu_{e^-}}{T} + \ln\left[\frac{Y_i n_\mathrm{B}}{G_i(T)}\left(\frac{2\pi}{m_i T}\right)^{3/2}\right]\right). \end{aligned} \tag{50}$$

Note that the external heating is accounted for with a first-order forward Euler method. We plan to improve this in the future when we implement higher-order integration methods for the network itself. With the above, SkyNet can update the entropy after every time step and then obtain the new temperature at the end of the time step from the EOS. Therefore, we only need to know the initial entropy (or temperature, from which the

entropy is determined). This changes the evolution (Equation (37)) slightly, because we now have to use the entropy at the beginning of the time step to estimate the temperature at the end of the time step. That is, we solve

$$\mathbf{0} = \boldsymbol{F}(\boldsymbol{x}, T^*, \rho(t + \Delta t)), \tag{51}$$

where T^* is given by the EOS as

$$T^* = \mathrm{EOS}(s(t), \rho(t + \Delta t), \boldsymbol{Y}(t)). \tag{52}$$

Equation (51) is solved with the NR method, as described in the previous section. Note that Δt is fixed during the NR iterations, which means that the temperature and density are also fixed. After the NR iterations have converged, we have found the new abundances $Y_i(t + \Delta t)$ and then we can compute Δs according to Equation (50) and update the entropy as

$$s(t + \Delta t) = s(t) + \Delta s. \tag{53}$$

Hence, we have a hybrid implicit/explicit scheme where the abundances are evolved implicitly but the entropy is evolved explicitly. One could also evolve the entropy implicitly together with the abundances, which would require computing $\partial \dot{Y}_i / \partial s$ and $\partial \dot{s} / \partial Y_i$ and adding these terms to the Jacobian. We may extend SkyNet in the future to support such a fully implicit scheme, but for now, we have achieved good results with the hybrid approach.

The energy released as nuclear binding energy due to nuclear reactions is

$$\dot{\epsilon}_{\mathrm{nuc}} = -\frac{1}{\Delta t} \sum_i \Delta Y_i m_i = -\frac{1}{\Delta t} \sum_i \Delta Y_i \mathcal{M}_i, \tag{54}$$

where we used Equation (49) and $\Delta Y_i / \Delta t$ is an approximation for $\dot{Y}_i$ over the time step. Note that the minus sign comes from the fact that some rest mass (or mass excess) is converted into energy, and hence the heating rate is positive if there is a net reduction in the total rest mass. Some authors (e.g., Hix & Thielemann 1999) treat $\dot{\epsilon}_{\mathrm{nuc}}$ as an external heat source. This is necessary if the EOS does not depend on the entire composition but only on $\bar{A}$ and $\bar{Z}$, the average mass and charge numbers, for example. In order to compare the nuclear heating in SkyNet to other codes, SkyNet computes and records a total heating rate $\dot{\epsilon}_{\mathrm{tot}}$, regardless of whether self-heating is enabled. $\dot{\epsilon}_{\mathrm{tot}}$ is computed as

$$\dot{\epsilon}_{\mathrm{tot}} = \frac{\Delta q}{\Delta t} + \dot{\epsilon}_{\mathrm{nuc}} = -\dot{\epsilon}_{\nu} + \dot{\epsilon}_{\mathrm{ext}} - \frac{1}{\Delta t} \sum_i \Delta Y_i \mathcal{M}_i. \tag{55}$$

Note that the above has units of erg s^{-1} baryon^{-1}. To convert it to the more commonly used units of erg s^{-1} g^{-1}, we simply multiply $\dot{\epsilon}_{\mathrm{tot}}$ by the Avogadro constant N_A.

Currently, SkyNet records the total heating rate shown above. In reality, this heating rate is composed of multiple components that are thermalized in the material in different ways (e.g., Barnes et al. 2016). For example, emitted electrons and positrons, as well as the kinetic energy of fission fragments, thermalize with very high efficiency, while only a small fraction of the energy released as neutrinos might thermalize. In a future version of SkyNet, we plan to record the different heating rate components, so that thermalization can be taken into account in kilonova light curve calculations, for example.

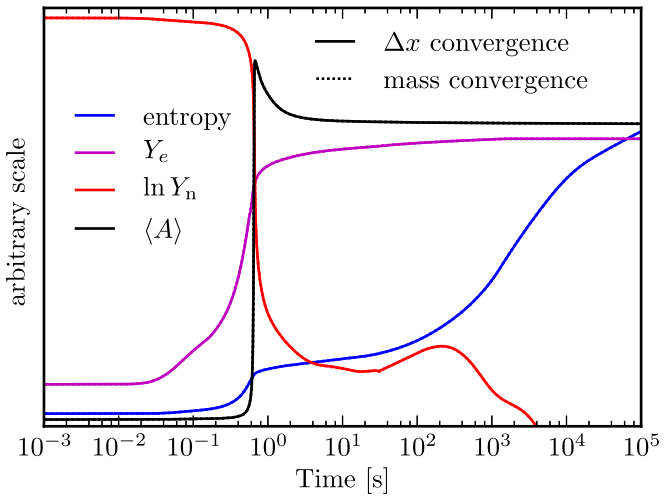

Figure 1. Comparison of the two convergence criteria. The solid lines show the entropy, electron fraction Y_e, logarithm of the neutron abundance Y_n, and average mass number $\langle A \rangle$ as a function of time using the Δx convergence criterion (Equation (56)) with $\varepsilon_{\mathrm{tol},\Delta x} = 10^{-6}$. The dotted lines plotted on top of the solid lines are the same quantities using the mass conservation convergence criterion (Equation (57)) with $\varepsilon_{\mathrm{tol,mass}} = 10^{-10}$. For all quantities, the two lines are exactly on top of each other and so the dotted lines are not visible. All quantities have been scaled by an arbitrary amount to fit on one figure. The networks evolve an r-process starting at 6 GK with initial $Y_e = 0.1$, $s = 10\, k_{\mathrm{B}}$ baryon^{-1} and an analytic density profile described in Lippuner & Roberts (2015) with expansion timescale 7.1 ms. The networks contain 7843 nuclides and 140,000 reactions.

3.3. Convergence Criteria and Time Stepping

The time step for the network evolution needs to be adjusted depending on how well the NR iteration (Equation (38)) converges. All of the default values and thresholds mentioned in this section are adjustable by the user. To check that the NR iterations have completely converged, a standard criterion is (Press et al. 2007)

$$\sum_{x_i^{(n+1)} \geqslant Y_{\mathrm{thr}}} \left| \frac{x_i^{(n+1)} - x_i^{(n)}}{x_i^{(n+1)}} \right| < \varepsilon_{\mathrm{tol},\Delta x}, \tag{56}$$

where $x_i^{(n+1)}$ is the ith component of the vector $\boldsymbol{x}_{n+1}$, and $\boldsymbol{x} = \boldsymbol{Y}(t + \Delta t)$ are the unknown abundances at the end of the current time steps that we want to find. The sum only runs over the indices i for which $x_i^{(n+1)} \geqslant Y_{\mathrm{thr}}$ for some abundance threshold Y_{thr}, which we usually set to 10^{-20}. The default value is $\varepsilon_{\mathrm{tol},\Delta x} = 10^{-6}$. Although this convergence criterion ensures that any subsequent NR iterations would no longer change the solution $\boldsymbol{x}_{n+1}$, we found that this criterion is too strict in practice. Instead, SkyNet typically uses mass conservation as a heuristic convergence criterion (which is also used by Hix & Thielemann 1999), which takes the form

$$\left| 1 - \sum_i x_i^{(n+1)} A_i \right| < \varepsilon_{\mathrm{tol,mass}}, \tag{57}$$

where we usually use $\varepsilon_{\mathrm{tol,mass}} = 10^{-10}$. Note that the sum now runs over all nuclear species, and there is no threshold for $x_i^{(n+1)}$. Since $x_i^{(n+1)} = Y_i(t + \Delta t)$, this convergence criterion is simply the conservation of the total baryon number. The user of SkyNet can choose to use Equations (56), (57), or both as the convergence criterion for Equation (38).

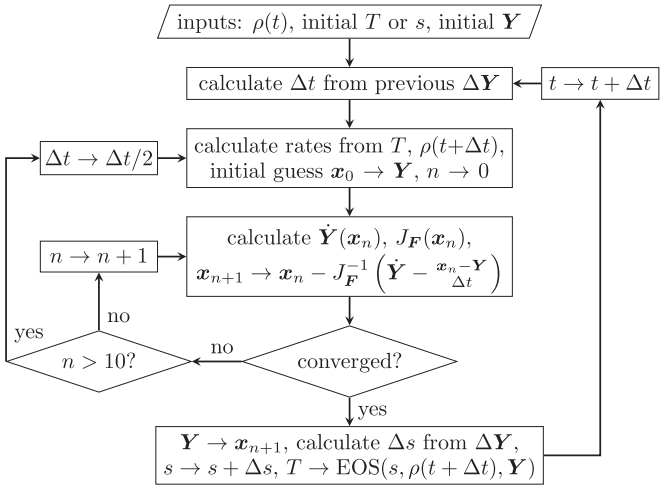

Figure 2. Simplified overview of the adaptive time-stepping mechanism used in SkyNet. If the NR iterations do not converge after 10 iterations, the time-step size Δt is cut in half and the time step is attempted again. There are other conditions that can result in a failed step and a subsequent retry with a smaller time-step size. See the text for details. After a successful time step, the next Δt is computed from the size of the abundance changes $\Delta \boldsymbol{Y}$ (Equation (58)), and at that point Δt can increase or decrease.

Figure 1 shows an r-process evolution with the two different convergence criteria using $\varepsilon_{\mathrm{tol},\Delta x} = 10^{-6}$ and $\varepsilon_{\mathrm{tol,mass}} = 10^{-10}$. These convergence thresholds result in almost exactly the same time-step sizes, but if we made $\varepsilon_{\mathrm{tol},\Delta x}$ smaller, that would result in much smaller time steps. However, using the Δx convergence criterion requires an average of 3.1 NR iterations per time step, while mass conservation only needs 1.2 NR iterations per time step. Since the total number of time steps is almost the same, using mass conservation as the convergence criterion is about 2.1 times faster for this particular case. As Figure 1 shows, however, the nucleosynthesis evolution is identical in the two cases. No differences are visible in the entropy, electron fraction, neutron abundance, or average mass number as a function of time. The maximum absolute difference in the final abundances of the two cases (using the Δx or mass conservation convergence criterion) is about 1.6×10^{-7}.

SkyNet adjusts the time-step size Δt dynamically. Once the NR iterations have converged according to the chosen criterion, SkyNet checks that the composition did not change too much over the last time step. The temperature and entropy are allowed to change by at most 1%. If either of them changes by more than this threshold, then the time step is considered failed and Δt is reduced by a factor of two, and the whole step is attempted again with the reduced time-step size. SkyNet also considers the time step as failed if the NR iterations do not converge after 10 iterations, or if the error measure used for the NR convergence criterion increases compared to the error of the previous iteration, or if the error decreases by less than 10%. In all of those cases, Δt is reduced and the time step is attempted again. A simplified schematic of this mechanism is shown in Figure 2.

After a successful time step, SkyNet attempts to increase the step size for the next time step. SkyNet tries to double Δt after every successful step, but this new time step can be limited if the abundance of a particular nuclide changed by a large amount in the previous time step. If that is the case, then the new time step is limited to the approximate step size necessary to keep the abundance of the nuclide that changed the most over the last time step from changing by more than 10%. Hence, the new time step is computed as

$$\Delta t^{(n+1)} = \min\left\{\Delta t_{\max},\, 2\Delta t^{(n)},\, \frac{10\%\ \Delta t^{(n)}}{\max_i(\Delta Y_i / Y_i)}\right\}, \tag{58}$$

where $\Delta t_{\max}$ is the maximum allowed time step and $\Delta t^{(n)}$ is the previous time step. Using this adaptive time-stepping mechanism, we typically get a time-step size that grows exponentially with time in freely expanding trajectories while keeping the error measure used for the convergence criterion below its prescribed tolerance.

Very rarely, it is necessary to renormalize the composition. In that case, every abundance is divided by the total mass, i.e.,

$$Y_{i,\mathrm{new}} = \frac{Y_i}{\sum_i A_i Y_i}, \tag{59}$$

and then the new composition satisfies $\sum_i A_i Y_i = 1$ exactly. Although this artificially injects or removes energy from the system, it is useful as a last resort if the time-step size is kept small because the composition is far away from mass conservation (but still within the error tolerance). After renormalization, the evolution usually proceeds normally with a larger time step than before. We renormalize if the time step falls below a certain limit (usually 10^{-16}), or if there are more than 25 time steps in a row that tried to increase the step size but subsequently failed and had to keep the step size constant. In such cases, it could be that the time step is small because the mass conservation convergence criterion is preventing the time step from increasing. If this is the case, then renormalizing the abundances usually helps to increase the time step, because after renormalizing, mass conservation in Equation (57) is fulfilled exactly. But in some cases, for example when trying to evolve the network near NSE with reaction rates that are inconsistent with NSE (see Section 6.1.1), the time step is small because the abundances are changing rapidly and so renormalizing the composition does not help.

3.4. NSE Evolution Mode

If the abundances approach the NSE composition, the forward and inverse strong rates exactly balance (Section 2.3). In that case, all the partial derivatives in the Jacobian (Equation (40)) would be zero, resulting in a singular Jacobian. The Jacobian is not exactly singular, however, because the weak reactions (that are not in equilibrium with their inverses) contribute non-zero derivatives to the Jacobian. Nevertheless, as the strong reactions move into equilibrium, the network time step becomes very small as the Jacobian becomes close to being numerically singular. To alleviate this problem, SkyNet automatically switches from a full network evolution to an NSE evolution scheme, if the strong nuclear reaction timescale becomes shorter than the timescale over which the density changes, and if the temperature is above some threshold (a user setting with a default value of 7 GK). The full network is turned back on when these conditions are no longer satisfied. A similar approach is used by other groups (e.g., Iwamoto et al. 1999; Brachwitz et al. 2000).

If SkyNet determines that switching to NSE evolution is appropriate, it computes the NSE composition from the current

internal energy, density, and electron fraction. If the entropy and temperature of that NSE composition differs by less than 1% (user setting) from the current network entropy and temperature, then the switch to NSE is allowed. Otherwise, the full network evolution will continue and SkyNet will try to switch to the NSE evolution mode again after the next step. A test of the NSE evolution mode that demonstrates its necessity and consistency is presented in Section 6.3.

In the NSE evolution mode, SkyNet no longer evolves the abundances of all nuclear species. Instead, SkyNet only evolves the entropy s and electron fraction Y_e of the composition, which can change due to weak reactions, such as β-decays or neutrino interactions, which can change the charge of nuclides and heat the material. Recall that the electron fraction is $Y_e = \sum_i Z_i Y_i$, and so

$$\dot{Y}_e = \sum_i Z_i \dot{Y}_i, \tag{60}$$

where $\dot{Y}_i$ is given by Equation (15) as a function of T, ρ, and $\boldsymbol{Y}$. The temperature is given by the EOS as a function of s, ρ, and $\boldsymbol{Y}$. $\boldsymbol{Y}$ is given by NSE as a function of s, ρ, and Y_e (see Appendix B.2). Thus, we have

$$\boldsymbol{Y} = \mathrm{NSE}(s,\, \rho,\, Y_e), \tag{61}$$

$$T = \mathrm{EOS}(s,\, \rho,\, \boldsymbol{Y}), \tag{62}$$

$$\dot{\boldsymbol{Y}} = [\text{weak reactions}](T,\, \rho,\, \boldsymbol{Y}), \tag{63}$$

$$\dot{Y}_e = \sum_i Z_i \dot{Y}_i. \tag{64}$$

The rate of change of the entropy is obtained from dividing Equation (50) by Δt, namely,

$$\begin{aligned}\dot{s} &= \frac{\dot{\epsilon}_{\mathrm{ext}} - \dot{\epsilon}_\nu}{T} - \sum_i \dot{Y}_i \left(\frac{\mathcal{M}_i}{T} + \frac{Z_i \mu_{e^-}}{T} \right. \\ &\quad \left. + \ln\left[\frac{Y_i n_{\mathrm{B}}}{G_i(T)} \left(\frac{2\pi}{m_i T} \right)^{3/2} \right] \right) \\ &= \dot{s}(\dot{\epsilon}_\nu,\, \dot{\epsilon}_{\mathrm{ext}},\, T,\, \dot{\boldsymbol{Y}},\, \boldsymbol{Y},\, \rho) = \dot{s}(\dot{\epsilon}_\nu,\, \dot{\epsilon}_{\mathrm{ext}},\, s,\, \rho,\, Y_e).\end{aligned} \tag{65}$$

Since $\dot{\epsilon}_\nu(t)$, $\dot{\epsilon}_{\mathrm{ext}}(t)$, and $\rho(t)$ are known, we thus have two coupled ODEs for Y_e and s, which SkyNet integrates with the Runge–Kutta–Fehlberg 4(5) method (e.g., Burden et al. 2015, Section 5.5). This is a fourth-order explicit integration method that also computes a fifth-order error estimate that is used to adaptively control the integration time step. The heating rate can be calculated analogously to Equation (55) as

$$\dot{\epsilon} = -\dot{\epsilon}_\nu + \dot{\epsilon}_{\mathrm{ext}} - \sum_i \dot{Y}_i \mathcal{M}_i. \tag{66}$$

Note that in the NSE evolution mode, we only evolve two variables and they are changing on similar timescales because they are both influenced by the weak reactions. In this case, however, even though the weak reactions span a large range of timescales, this does not introduce any stiffness because we only deal with the sum of the abundance derivatives in both Equations (60) and (65). Thus, we can safely use an explicit integration method.

4. Electron Screening

Nuclear reaction rates strongly depend on the Coulomb interaction between the nuclides in the entrance channel (e.g., Salpeter 1954). In conditions where nuclear burning can occur, the nuclides are almost all fully ionized. Therefore, nuclear reaction rates can be computed assuming that bare nuclei of charge Z_i interact with each other. At high temperature, the Coulomb interaction energy of the electrons with the nuclei is small compared to the thermal energies of the particles and so the screening effect is negligible. But if the density of the medium is sufficiently high and the temperature sufficiently low, electron screening is likely important. In these conditions, a nucleus will repel neighboring nuclei and attract nearby electrons, thus creating an electron charge cloud around the nucleus. This charge cloud partially screens or shields the nuclear charge $Z_i e$, where e is the elementary charge unit. Thus, the Coulomb repulsion between the two positively charged nuclei is reduced by the screening effect, which can enhance the nuclear reaction rates, which depend strongly on the probability of Coulomb barrier penetration. Obviously, screening corrections are only important for charged particle reactions. Neutron capture reactions are unaffected by the polarization of the electron gas.

In this section, we present how electron screening is implemented in SkyNet. Our focus will be on writing down the equations that SkyNet uses to compute the screening corrections in a useful way with adequate justification. We will not develop the screening theory from first principles but refer the reader to the established literature on this subject (e.g., Salpeter 1954; Dewitt et al. 1973; Graboske et al. 1973; Itoh et al. 1979; Ichimaru & Utsumi 1984; Brown & Sawyer 1997; Bravo & García-Senz 1999; Yakovlev et al. 2006, to name but a few). For a handful of reactions, screening has been investigated experimentally (e.g., Engstler et al. 1988; Rolfs & Somorjai 1995; Chen et al. 2004; Gatu Johnson et al. 2017). We use Gaussian cgs units throughout this section.

The strength of the electron screening effect depends mainly on the ratio of the Coulomb interaction energy between a nucleus and the nearby electrons to the thermal energy. If the thermal energy is large compared to the Coulomb interaction energy, then the electron charge cloud around the nucleus will be large and diffuse, providing less screening to the nuclear charge. We define the ion density

$$n_I = \sum_i n_i = \sum_i Y_i n_{\mathrm{B}} = n_{\mathrm{B}} \sum_i Y_i. \tag{67}$$

The average interionic spacing is

$$a = \left(\frac{3}{4\pi n_I} \right)^{1/3}. \tag{68}$$

Now, we define the dimensionless screening parameter Λ_0 as

$$\Lambda_0 = \sqrt{4\pi n_I}\, e^3 \beta^{3/2}, \tag{69}$$

where $\beta = 1/T$. For some average (dimensionless) charge per ion ζ (defined later on in Equation (92)), let

$$\Lambda = \zeta^3 \Lambda_0 = \left(\frac{3^{1/3} \zeta^2 e^2}{aT} \right)^{3/2}. \tag{70}$$

Thus, Λ is a measure of the ratio of the average Coulomb interaction energy $\zeta^2 e^2 / a$ to the average thermal energy T. If Λ is large, we expect the screening effect to be strong, and when Λ is small, screening should be weak. The screening corrections in these two regimes, as well as the intermediate regime where $\Lambda \sim 1$, are the subject of the following sections,

after we introduce the general screening factor that modifies the nuclear reaction rate.

4.1. General Screening Factor

For the two-body reaction $[1] + [2] \rightarrow [3]$, the total Coulomb potential can be written as

$$U_{\rm tot}(r_{12}) = \frac{Z_1 Z_2 e^2}{r_{12}} + U(r_{12}), \tag{71}$$

where $U(r_{12})$ is a potential correction to the bare Coulomb interaction between the two nuclei due to screening, r_{12} is the separation of the two reactants, and Z_1 and Z_2 are the charge numbers. Salpeter (1954) showed that the screening correction to the nuclear reaction rate λ_{12} is given by

$$\lambda_{12} = e^{-U_0/T} \lambda_{12,\text{no-sc}} = f_{\rm sc}\, \lambda_{12,\text{no-sc}}, \tag{72}$$

where $U_0 = U(r_{12} = 0)$, $\lambda_{12,\text{no-sc}}$ is the unscreened reaction rate, and $f_{\rm sc} = e^{-U_0/T}$ is the general screening factor. Note that $f_{\rm sc}$ is sometimes written as $\exp(H_{12}(0))$ in the literature. An approximation for the screening factor $f_{\rm sc}$ can be found in terms of Z_1, Z_2, density, temperature, and other quantities determined by the composition. However, it is advantageous to (equivalently) write down the screening factor in terms of a chemical potential correction $\mu_{\rm sc}(Z)$ that depends on the charge of a single nucleus. This way, we can apply the screening corrections in NSE as well, and we are not constrained to only correcting reaction rates with two reactants. In this section, we show how to compute the reaction screening factor if we have the chemical potential correction $\mu_{\rm sc}(Z)$. In the following sections, we will show how to compute $\mu_{\rm sc}(Z)$ in different screening regimes.

For the same two-body reaction $[1] + [2] \rightarrow [3]$, Dewitt et al. (1973) found that the screening factor can also be written as

$$f_{\rm sc} = \exp\left(\beta\mu_{\rm sc}(Z_1) + \beta\mu_{\rm sc}(Z_2) - \beta\mu_{\rm sc}(Z_3)\right), \tag{73}$$

where $\beta = 1/T$, $\mu_{\rm sc}(Z)$ is the correction to the chemical potential for the addition of a charge Z to the system when the electron gas is non-uniform, and $Z_3 = Z_1 + Z_2$ is the charge of the product. It is straightforward to generalize this result to an arbitrary (i.e., not just two-body) reaction α as

$$f_{\rm sc} = \exp\left(\sum_{i\in\mathcal{R}_\alpha} N_i^\alpha \beta\mu_{\rm sc}(Z_i) - \beta\mu_{\rm sc}(Z_{\mathcal{R}}^\alpha)\right), \tag{74}$$

where $\mathcal{R}_\alpha$ is the set of reactant species of the reaction and N_i^α is the number of species $[i]$ destroyed or produced in the reaction (see Section 2.1 and Equation (5)). We also define

$$Z_{\mathcal{R}}^\alpha = \sum_{i\in\mathcal{R}_\alpha} N_i^\alpha Z_i. \tag{75}$$

The above expression for the screening factor $f_{\rm sc}$ for reactions with an arbitrary number of particles in the entrance channel holds for multistep reactions. This can be shown by breaking up the multibody reaction into two-body reactions, e.g., treating $[1] + [2] + [3] \rightarrow X$ as $[1] + [2] \rightarrow [12]$ followed by $[12] + [3] \rightarrow X$, and then calculating the overall screening factor. To justify the general form of $f_{\rm sc}$, consider a two-body reaction that produces an arbitrary set of products $\mathcal{P}_\alpha$, i.e.,

$$[1] + [2] \rightarrow \sum_{j\in\mathcal{P}_\alpha} N_j^\alpha [j], \tag{76}$$

where $Z_1 + Z_2 = \sum_{j\in\mathcal{P}_\alpha} N_j^\alpha Z_j$ due to charge conservation. Let $\lambda_{\alpha,\text{no-sc}}$ and $\lambda_{\alpha',\text{no-sc}}$ be the reaction rates of the forward and inverse reactions without the screening corrections. The corrected forward rate is

$$\lambda_\alpha = \lambda_{\alpha,\text{no-sc}} \exp\left(\beta\mu_{\rm sc}(Z_1) + \beta\mu_{\rm sc}(Z_2) - \beta\mu_{\rm sc}(Z_1 + Z_2)\right). \tag{77}$$

Equation (125) gives the chemical potential of nuclear species $[i]$ without the screening correction, which we call $\mu_{i,\text{no-sc}}$. The corrected chemical potential is $\mu_i = \mu_{i,\text{no-sc}} + \mu_{\rm sc}(Z_i)$. Note that the chemical potential correction $\mu_{\rm sc}(Z_i)$ enters on the same level as the term m_i in Equation (125) and therefore, $\mu_{\rm sc}(Z_i)$ can be absorbed into Q_α, the rest mass difference between the reactants and products, defined in Equation (33). Q_α thus becomes

$$\begin{aligned} Q_\alpha &= Q_{\alpha,\text{no-sc}} + \sum_{i\in\mathcal{R}_\alpha} N_i^\alpha \mu_{\rm sc}(Z_i) - \sum_{j\in\mathcal{P}_\alpha} N_j^\alpha \mu_{\rm sc}(Z_j) \\ &= Q_{\alpha,\text{no-sc}} + \mu_{\rm sc}(Z_1) + \mu_{\rm sc}(Z_2) - \sum_{j\in\mathcal{P}_\alpha} N_j^\alpha \mu_{\rm sc}(Z_j). \end{aligned} \tag{78}$$

Substituting the above corrected expressions for λ_α and Q_α into Equation (32) yields

$$\begin{aligned} \lambda_{\alpha'} &= \lambda_{\alpha',\text{no-sc}} \exp\left(\beta\mu_{\rm sc}(Z_1) + \beta\mu_{\rm sc}(Z_2) - \beta\mu_{\rm sc}(Z_1 + Z_2)\right) \\ &\quad \times \exp\left(\sum_{j\in\mathcal{P}_\alpha} N_j^\alpha \beta\mu_{\rm sc}(Z_j) - \beta\mu_{\rm sc}(Z_1) - \beta\mu_{\rm sc}(Z_2)\right) \\ &= \lambda_{\alpha',\text{no-sc}} \exp\left(\sum_{j\in\mathcal{P}_\alpha} N_j^\alpha \beta\mu_{\rm sc}(Z_j) - \beta\mu_{\rm sc}(Z_1 + Z_2)\right) \\ &= \lambda_{\alpha',\text{no-sc}} \exp\left(\sum_{j\in\mathcal{P}_\alpha} N_j^\alpha \beta\mu_{\rm sc}(Z_j) - \beta\mu_{\rm sc}(Z_{\mathcal{P}}^\alpha)\right), \end{aligned} \tag{79}$$

where we used charge conservation, i.e., $Z_1 + Z_2 = \sum_{j\in\mathcal{P}_\alpha} N_j^\alpha Z_j = Z_{\mathcal{P}}^\alpha$. Thus, the screening factor for the inverse reaction (whose set of reactants is $\mathcal{P}_\alpha$) is indeed exactly the generalized screening factor postulated in Equation (74). Thus, we only need to know how to compute $\mu_{\rm sc}(Z)$, which is the subject of the following sections. Note that in terms of the screened forward rate, we combine the above with detailed balance (Equation (32)) to obtain the screened inverse rate

$$\begin{aligned} \lambda_{\alpha'} &= \lambda_\alpha(T, \rho) \\ &\quad \times \exp\left(\sum_{j\in\mathcal{P}_\alpha} N_j^\alpha \beta\mu_{\rm sc}(Z_j) - \sum_{i\in\mathcal{R}_\alpha} N_i^\alpha \beta\mu_{\rm sc}(Z_i)\right) \\ &\quad \times e^{-Q_\alpha/T} \Gamma_\alpha(T) M_\alpha^{3/2} \left(\frac{T}{2\pi}\right)^{3\Delta N_\alpha/2} (\rho N_A)^{-\Delta N_\alpha}, \end{aligned} \tag{80}$$

where we used $Z_{\mathcal{P}}^\alpha = Z_{\mathcal{R}}^\alpha$ since strong reactions conserve charge.

It now remains to find the screening chemical potential correction $\mu_{\rm sc}(Z)$ for a nuclide of charge Z. Thanks to SkyNet's modularity, arbitrary expressions for $\mu_{\rm sc}(Z)$ can be plugged into the general screening framework. In the following sections, we describe the current implementation of $\mu_{\rm sc}(Z)$ in SkyNet.

4.2. Weak Screening

The weak screening limit is the limiting case where the Coulomb interaction energy is much lower than the thermal energy, hence, where $\Lambda \ll 1$. In this case, the electrostatic Poisson–Boltzmann equation describing the screening can be solved approximately to find (Salpeter 1954)

$$-\frac{U_0}{T} = \frac{Z_1 Z_2 e^2}{\lambda_D T}, \tag{81}$$

where λ_D is the Debye screening length. $\kappa_D = \lambda_D^{-1}$ is called the Debye wave number, and it is given by (Brown & Sawyer 1997)

$$\kappa_D^2 = \sum_i \kappa_{D,i}^2, \tag{82}$$

where the Debye wave number of species $[i]$ is

$$\kappa_{D,i}^2 = 4\pi (Z_i e)^2 \int \frac{d^3p}{(2\pi)^3} \frac{\partial f_i(p, \mu_i)}{\partial \mu_i}, \tag{83}$$

where $Z_i e$ is the charge, μ_i is the chemical potential (defined in Equation (125)), and $f_i(p, \mu_i)$ is the distribution function of species $[i]$.

SkyNet assumes that the ions (nuclides) are non-degenerate and non-relativistic. Therefore, they obey Boltzmann statistics with $E(p) = p^2/(2m_i) + m_i$, where p is the momentum and m_i is the mass of species $[i]$. Hence,

$$\begin{aligned} f_i(p, \mu_i) &= \exp(-\beta(E(p) - \mu_i)) \\ &= \exp\left(\beta\mu_i - \frac{p^2\beta}{2m_i} - \beta m_i\right), \end{aligned} \tag{84}$$

and so

$$\int \frac{d^3p}{(2\pi)^3} \frac{\partial f_i(p, \mu_i)}{\partial \mu_i} = \int \frac{d^3p}{(2\pi)^3} \beta f_i(p, \mu_i) = \beta n_i, \tag{85}$$

and hence

$$\kappa_{D,i}^2 = 4\pi Z_i^2 e^2 \beta n_i, \tag{86}$$

where n_i is the number density of ion species $[i]$.

The electrons and positrons are allowed to be arbitrarily degenerate and arbitrarily relativistic. They are both fermions and thus follow Fermi–Dirac statistics, so

$$f_{e^\pm}(p, \mu_{e^\pm}) = \frac{1}{\exp(\beta(E(p) - \mu_{e^\pm})) + 1}, \tag{87}$$

where $E(p)$ is the total energy

$$E(p) = \sqrt{m_e^2 + p^2}\,. \tag{88}$$

We find

$$\begin{aligned} \frac{\partial f_{e^\pm}(p, \mu_{e^\pm})}{\partial \mu_{e^\pm}} &= \frac{\beta \exp(\beta(E(p) - \mu_{e^\pm}))}{[\exp(\beta(E(p) - \mu_{e^\pm})) + 1]^2} \\ &= \beta f_{e^\pm}(1 - f_{e^\pm}), \end{aligned} \tag{89}$$

and so

$$\kappa_{D,e^\pm}^2 = 4\pi e^2 \beta \int \frac{d^3p}{(2\pi)^3} 2 f_{e^\pm}(1 - f_{e^\pm}), \tag{90}$$

where the extra factor of 2 in the phase-space integral comes from the fact that fermions have two spin states, and we used $Z_{e^\pm} = \pm 1$.

The Debye length is thus

$$\lambda_D = \kappa_D^{-1} = \sqrt{\frac{1}{4\pi e^2 \beta n_I \zeta^2}}\,, \tag{91}$$

where

$$\begin{aligned} \zeta^2 = \frac{n_{\rm B}}{n_I}\Bigg[&\sum_i Z_i^2 Y_i \\ &+ \frac{2}{n_{\rm B}} \int \frac{d^3p}{(2\pi)^3} \times (f_{e^-}(1 - f_{e^-}) + f_{e^+}(1 - f_{e^+}))\Bigg]. \end{aligned} \tag{92}$$

Note that the factor of $n_{\rm B}/n_I$ in ζ occurs because we define ζ as the rms charge per ion rather than per nucleon. The distribution functions $f_{e^\pm}$ (Equation (87)) depend on the electron and positron chemical potentials $\mu_{e^\pm}$, which are given by the EOS (Equations (131) and (132)). SkyNet uses the adaptive QAG integration routines provided by the GNU Scientific Library[12] to evaluate the above integral numerically. The two-body screening potential in Equation (81) becomes

$$-\frac{U_0}{T} = \frac{Z_1 Z_2 e^2}{\lambda_D T} = Z_1 Z_2 \zeta e^3 \sqrt{4\pi n_I}\, \beta^{3/2} = Z_1 Z_2 \zeta \Lambda_0, \tag{93}$$

and so the screening factor is

$$f_{\rm sc} = e^{-U_0/T} = \exp(-Z_1 Z_2 \zeta \Lambda_0). \tag{94}$$

This is consistent with the result from Dewitt et al. (1973), who showed that in the weak screening case, the chemical potential correction due to screening is

$$\beta\mu_{\rm sc,weak}(Z) = -\frac{1}{2} Z^2 \zeta \Lambda_0. \tag{95}$$

Combining the above with the expression for the general screening factor (Equation (74)) yields

$$\begin{aligned} f_{\rm sc} &= \exp(\beta\mu_{\rm sc,weak}(Z_1) + \beta\mu_{\rm sc,weak}(Z_2) \\ &\quad - \beta\mu_{\rm sc,weak}(Z_1 + Z_2)) \\ &= \exp\left(-\frac{1}{2}\zeta\Lambda_0[Z_1^2 + Z_2^2 - (Z_1 + Z_2)^2]\right) \\ &= \exp(-Z_1 Z_2 \zeta \Lambda_0), \end{aligned} \tag{96}$$

as shown in Equation (94).

4.3. Strong and Intermediate Screening

In the strong screening limit, the Poisson–Boltzmann equation governing screening has to be solved numerically.

[12] https://www.gnu.org/software/gsl/manual/html_node/Numerical-Integration.html

Dewitt et al. (1973) found that

$$\beta\mu_{\rm sc,strong}(Z) = -\frac{Z}{\bar{Z}}\left(Z^{2/3}\bar{Z}^{4/3}\Gamma_0\left(c_0 + c_1\left(\frac{\bar{Z}}{Z}\right)^{1/3} + c_2\left(\frac{\bar{Z}}{Z}\right)^{2/3}\right) + d_0 + d_1\left(\frac{\bar{Z}}{Z}\right)^{1/3}\right), \tag{97}$$

where $c_0 = 9/10$, $c_1 = 0.2843$, $c_2 = -0.054$, $d_0 = -9/16$, and $d_1 = 0.4600$. The parameter Γ_0 is

$$\Gamma_0 = \Lambda_0^{2/3}/3^{1/3}, \tag{98}$$

and the applicable average charge per ion is the arithmetic mean $\bar{Z}$, instead of the rms ζ, which is given by

$$\bar{Z} = \frac{\sum_i Z_i Y_i}{\sum_i Y_i}. \tag{99}$$

We can write Equation (97) in terms of Λ_0 as

$$\beta\mu_{\rm sc,strong}(Z) = -\Lambda_0^{2/3}(0.6240\, Z^{5/3}\bar{Z}^{1/3} + 0.1971\, Z^{4/3}\bar{Z}^{2/3} - 0.0374\, Z\bar{Z}) + \frac{9}{16}\frac{Z}{\bar{Z}} - 0.4600\left(\frac{Z}{\bar{Z}}\right)^{2/3}, \tag{100}$$

which is valid when $\Gamma = \bar{Z}^2\Gamma_0 \gg 1$. Alternatively, if $\zeta \sim \bar{Z}$, then $\Gamma \sim \Lambda^{2/3}$ and so the strong screening limit applies if $\Lambda \gg 1$. The strong screening limit is also applicable if $\Lambda \ll 1$ but the charge Z is such that $Z\zeta^2\Lambda_0 \gg 1$. Then strong screening applies for charge Z (Dewitt et al. 1973).

The intermediate screening regime is where $\Lambda = \zeta^3\Lambda_0 \sim 1$, in which case Dewitt et al. (1973) found

$$\beta\mu_{\rm sc,intermediate}(Z) = -0.380\,\Lambda_0^b\eta_b Z^{b+1}, \tag{101}$$

where $b = 0.860$ and

$$\eta_b = \frac{\sum_i Z_i^{3b-1} n_i/n_I}{\zeta^{3b-2}\bar{Z}^{2-2b}} = \frac{n_{\rm B}}{n_I}\frac{\sum_i Z_i^{3b-1}Y_i}{\zeta^{3b-2}\bar{Z}^{2-2b}}. \tag{102}$$

4.4. Combining the Different Screening Regimes

Equations (95), (100), and (101) give the chemical potential corrections in the limits of weak, strong, and intermediate screenings, respectively. To smoothly transition between these three regimes, we need a single parameter that determines which regime is applicable and a function that smoothly interpolates between the regimes based on the said parameter.

Weak screening applies if $\Lambda = \zeta^3\Lambda_0 \ll 1$ and strong screening if $\Lambda \gg 1$ or $\Lambda \ll 1$ but $Z\zeta^2\Lambda_0 = \Lambda Z/\zeta \gg 1$. We thus define the dimensionless parameter

$$p(Z) = \Lambda + \Lambda\frac{Z}{\zeta} = (\zeta + Z)\zeta^2\Lambda_0. \tag{103}$$

Note that $p(Z) \ll 1$ if and only if $\Lambda \ll 1$ and $\Lambda\, Z/\zeta \ll 1$, in which case weak screening applies. If and only if $\Lambda \gg 1$ or $\Lambda Z/\zeta \gg 1$ is $p(Z) \gg 1$, in which case we are in the strong screening regime. If $p(Z) \sim 1$, then intermediate screening applies. To ensure a smooth transition of $\beta\mu_{\rm sc}$ from one regime to another, we will compute the screening correction as a weighted sum of the corrections computed in the different regimes. Hence, we compute

$$\beta\mu_{\rm sc}(Z) = f_w\,\beta\mu_{\rm sc,weak}(Z) + f_s\,\beta\mu_{\rm sc,strong}(Z) + f_i\,\beta\mu_{\rm sc,intermediate}(Z), \tag{104}$$

where each coefficient f_j is between 0 and 1 and defined as

$$f_w(p) = \frac{1}{2}[\tanh(-2\ln p - \ln 25) + 1], \tag{105}$$

$$f_s(p) = \frac{1}{2}[\tanh(2\ln p - \ln 25) + 1], \tag{106}$$

$$f_i(p) = \frac{1}{2}[\tanh(2\ln p + \ln 25) + \tanh(-2\ln p + \ln 25))]. \tag{107}$$

Note that $f_w(p) + f_s(p) + f_i(p) = 1$ for all values of p. The transition from weak to intermediate screening occurs at $p(Z) = 1/\sqrt{25} = 0.2$, and the transition from intermediate to strong screening occurs at $p(Z) = \sqrt{25} = 5$.

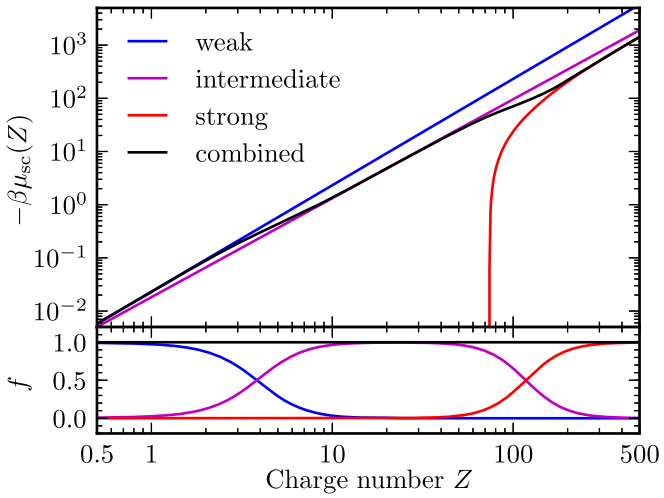

Figure 3. Screening correction to the chemical potential for a test particle with charge Z. The upper panel shows the corrections from the weak, intermediate, and strong regimes, as well as the combined correction. The bottom panel shows the functions f_w, f_i, and f_s that are used to weight the chemical potential corrections due to weak, intermediate, and strong screening. These screening corrections are computed at $T = 3$ GK and $\rho = 2 \times 10^9$ g cm^{-3} with a composition consisting of 59% neutrons, 40% protons, and 1% U^{238} (by mass).

Figure 3 demonstrates the transition between the different screening regimes. We choose a composition consisting of 59% neutrons, 40% protons, and 1% U^{238} (by mass) at $T = 3$ GK and $\rho = 2 \times 10^9$ g cm^{-3}. In this composition, all three screening regimes occur as the charge number of a test particle ranges from $Z = 1$ to $Z \sim 100$. In order to show the transitions more clearly, we plot the chemical potential corrections from the different regimes for Z ranging from 0.5 to 500 in Figure 3. Such charge numbers are not expected to occur in reality, but the expressions for the chemical potential corrections are valid nonetheless. The chosen composition results in $\Lambda_0 = 0.05089$, $\zeta = 0.9104$, $\bar{Z} = 0.4079$, $\eta_b = 0.6214$, and $\Lambda = 0.03840$.

Whereas Figure 3 shows the screening correction for different ion charges in a fixed composition, Figure 4 shows the screening correction for a fixed charge ($Z = 26$) in different compositions determined by the temperature T. Also shown is the Boltzmann chemical potential (Equation (125) without the rest mass) for ^{56}Fe. The composition is determined from NSE with screening corrections (Section 4.5) using a temperature

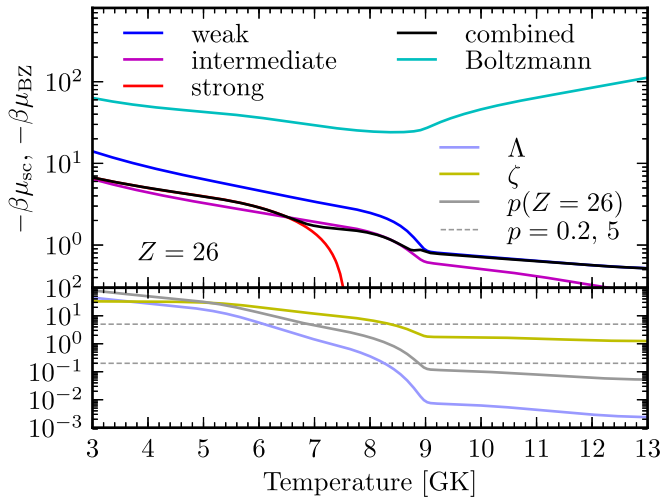

Figure 4. Screening correction to the chemical potential as a function of temperature for a fixed charge $Z = 26$. The composition is computed from NSE with screening corrections with the given temperature, $\rho = 10^8$ g cm^{-3}, and $Y_e = 0.4$. The upper panel shows the screening corrections from the weak, intermediate, and strong screening regimes, as well as the combined correction. The Boltzmann chemical potential μ_{BZ} of ^{56}Fe (Equation (125) without the rest mass) is also shown for comparison. The lower panel shows the screening parameter Λ (Equation (70)) and average charge per ion ζ (Equation (92)) computed from the composition, and the $p(Z)$ parameter used to transition between the different regimes for $Z = 26$. The dashed gray lines show the values of p at which the transitions from strong to intermediate screening ($p = 5$) and from intermediate to weak screening ($p = 0.2$) happen.

ranging from 3 to 13 GK, $\rho = 10^8$ g cm^{-3}, and $Y_e = 0.4$. At low temperatures ($T \lesssim 7$ GK), strong screening is applicable since the thermal energy is small and Coulomb interactions dominate. Electron screening provides a 10% correction over the unscreened Boltzmann chemical potential. Intermediate screening is applicable between 7 and 9 GK. At 9 GK, ^{4}He nuclei are broken up and free neutrons and protons start to dominate the composition. Thus, ζ remains roughly constant at 1, and so Λ and $p(26)$ also stop changing rapidly because Λ_0 does not depend strongly on the temperature. $T \sim 9$ GK is also where weak screening sets in, because the thermal energy now overcomes the Coulomb interaction energy, which has been reduced by the smaller average charge per ion provided by the free protons. In that regime, the screening effect is at the 4% to 0.5% level.

Figure 4 also shows that our screening corrections are indeed approximate. The weak and intermediate screening corrections never meet, so any scheme to transition between them is necessarily approximate and arbitrary to some degree. But considering the fact that our transition scheme needs to work robustly for a wide range of compositions and ion charges, it seems to do reasonably well in interpolating between the different (somewhat disjoint) screening regimes. Although progress has been made in improving screening calculations in various regimes, a unifying theory for screening across all regimes is still elusive (e.g., Itoh et al. 1977; Shaviv & Shaviv 1996, 2000; Chugunov et al. 2007).

4.5. NSE with Screening

As was noted above, in addition to screening nuclear reactions, electronic correlations also change the free energetic cost of adding or removing a charged particle from the medium. Therefore, the chemical potentials of the nuclides have an additional correction due to screening, i.e., $\mu_i = \mu_{i,\text{no-sc}} + \mu_{\rm sc}(Z_i)$, where $\mu_{i,\text{no-sc}}$ is the unscreened chemical potential given by Equation (125) and $\mu_{\rm sc}(Z_i)$ is the screening correction given by Equation (104) with Z_i being the charge number of nuclide i. Appendix B presents in detail how NSE is computed. Here, we briefly discuss how the method shown in Appendix B is modified to take chemical potential corrections into account. Equation (145) becomes

$$\hat{\mu}_i = \mu_{i,\text{no-sc}} + \mu_{\rm sc}(Z_i) - m_i - \text{BE}_i, \tag{108}$$

which means Equation (151) gives

$$Y_i = e^{\eta_i - \beta\mu_{\rm sc}(Z_i) + \beta\text{BE}_i} \frac{G_i(T)}{n_{\rm B}} \left(\frac{m_i T}{2\pi}\right)^{3/2}, \tag{109}$$

where $\beta = 1/T$. Note that $\mu_{\rm sc}(Z_i)$ depends on all Y_i because the screening corrections depend on different types of average ion charges ($\bar{Z}$, ζ, and η_b). Computing NSE involves an NR iteration that requires partial derivatives of Y_i (see Appendix B). Thus, the screening corrections in Equation (109) introduce a large number of complicated partial derivatives to the Jacobian, which we will not attempt to write down. We experimented with using numerical derivatives to compute the Jacobian, with limited success. Another complication is that Equation (109) itself depends on all Y_i on the right-hand side and thus has to be solved iteratively.

We find that it is much more robust to keep the screening corrections fixed during the NR iterations. This does not introduce any additional derivatives in the Jacobian. NSE is computed exactly as shown in Appendix B, with the only difference that Equation (109) is used to compute Y_i from η_i, but the terms $\beta\mu_{\rm sc}(Z_i)$ are constant throughout the NR iterations. In this case, to obtain an NSE composition that is self-consistent with the screening corrections it is based on, the NSE computation itself needs to be iterated.

We start by computing the NSE composition without screening (i.e., $\mu_{\rm sc}(Z_i) = 0$). We denote the resulting composition by $\boldsymbol{Y}^{(0)}$. Then, we compute $\mu_{\rm sc}(Z_i)$ based on $\boldsymbol{Y}^{(0)}$ and use these as the constant screening corrections for the next NSE computation that yields $\boldsymbol{Y}^{(1)}$. From this new composition we compute new screening corrections, which are used to compute $\boldsymbol{Y}^{(2)}$ and so on. This iteration stops once $\max_i(|Y_i^{(n+1)} - Y_i^{(n)}|) < 10^{-12}$ or n reaches 20 (both of these criteria can be changed by the user). This method of iteratively updating the screening corrections and computing NSE with them being fixed is not guaranteed to converge (but neither is the NR method itself). However, in practice, we find that this method works very well and converges quite quickly in a large region of parameter space.

Figure 5 shows the NSE abundance distribution as a function of mass number A for three different temperatures. For all temperatures, $\rho = 10^8$ g cm^{-3} and $Y_e = 0.4$, so this is the same composition as the one shown in Figure 4. To show the impact of the screening corrections, the NSE compositions with and without screening are shown in the left panel. Screening is strongest for $T = 3$ GK and the effect of screening is to reduce the abundances below $A \sim 80$ and slightly increase them above that mass number. Screening is weaker at $T = 8$ GK but still enhances the high-mass abundances above $A \sim 60$. Finally, for $T = 13$ GK, screening has virtually no effect. In the right panel of Figure 5, we show the ratio of the screening chemical potential $\mu_{\rm sc}$ to the Boltzmann chemical potential $\mu_{\rm BZ}$ (Equation (125) without the rest mass). $\mu_{\rm sc}$ depends on the composition and the charge, hence it is the same for all isotopes of a given element. But the Boltzmann chemical potential also

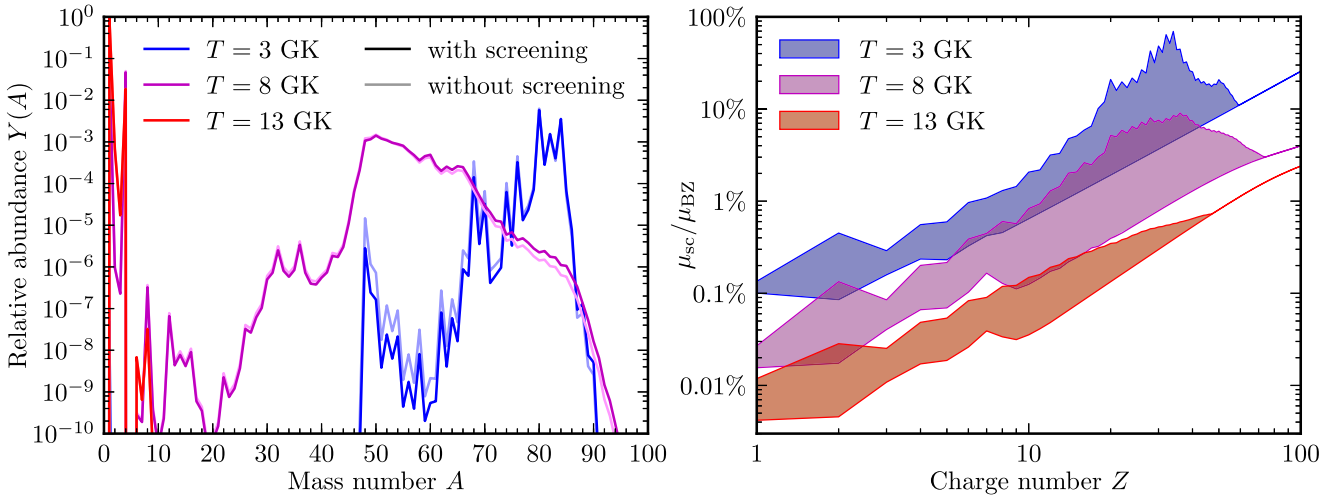

Figure 5. NSE compositions with and without screening at different temperatures. In all cases, $\rho = 10^8$ g cm^{-3} and $Y_e = 0.4$. Left: abundances as a function of mass number A of the compositions with and without screening. Screening pushes the abundance distribution to slightly higher masses. The effect at $T = 3$ GK is clearly visible. At $T = 8$ GK, the screening effect is quite small and at $T = 13$ GK it is practically absent. Right: the ratio of the screening chemical potential correction to the Boltzmann chemical potential (Equation (125) without the rest mass). The bands show the range of this ratio for all isotopes with the same charge number Z. The screening correction can be as large as 70% in the $T = 3$ GK case, and as low as 0.004% for $T = 13$ GK. At high Z where the bands collapse, all isotopes of the same element have the same screening to Boltzmann chemical potential ratio because their abundances are all extremely small.

depends on the mass, partition function, and the abundance of a given isotope. Thus, for a given charge number Z, the ratio μ_{sc}/μ_{BZ} varies for the isotopes of that charge. In Figure 5, we show the range of the chemical potential ratios as colored bands. The bands collapse to a line at large Z, because there the abundances of all isotopes are essentially zero. In the strongest screening case ($T = 3$ GK), the screening effect ranges from 0.1% to 70%. For $T = 8$ GK, it ranges from about 0.02% to 10%, and for $T = 13$ GK, the screening effect is much less than 1% except for very large Z.

5. Implementation Details

The main design goals of SkyNet are usability and flexibility. Since SkyNet is built in a modular fashion, different physics implementations can easily be switched out or new physics can be added, making SkyNet very flexible (see the next sections for details). To achieve the modularity, SkyNet is written in object-oriented C++ and makes use of some C++11 features. SkyNet contains a small amount of Fortran code to provide a minimal interface for SkyNet to be called from Fortran. CMake (http://www.cmake.org) provides a cross-platform, compiler-independent build system for SkyNet that automatically finds the required external libraries. CMake also provides an automated testing facility and SkyNet comes with a suite of tests that check basic functionality and correctness of SkyNet.

To make it easy to use, SkyNet comes with Python bindings that make it possible to use all parts of SkyNet from an interactive Python shell or a Python script. Therefore, one can use standard Python libraries like NumPy (http://www.numpy.org) to read in and manipulate input data, like the list of nuclides to be evolved, the initial composition, density versus time history, etc., and these data can be passed to SkyNet using standard Python data structures. This means that one does not have to deal with C++ to run SkyNet. But of course, SkyNet can also be used from a C++ or Fortran application. One can even run multiple copies of SkyNet in parallel within Python, using Python's `multiprocessing` module—a facility we use extensively whenever post-processing nucleosynthesis on many tracer particles from hydrodynamical simulations (e.g., Lippuner et al. 2017; Roberts et al. 2017). An example of how to run SkyNet in parallel with Python is included with the SkyNet source code available at https://bitbucket.org/jlippuner/skynet. The SkyNet Python bindings are provided by SWIG (http://www.swig.org) and using Python is the most convenient and most flexible way to run SkyNet.

5.1. Modularity and Extendability

SkyNet is a modular library of different C++ classes rather than a monolithic program. Some of the most important classes in SkyNet are the various reaction library classes that contain different types of nuclear reactions (see next section), a nuclide library class that contains all nuclear data, and a reaction network class that implements the actual nuclear reaction network. There are various other types of classes that implement specific functionalities. For example, there are different function interpolation classes, ODE integrators, and general numerical method classes (bisection, line search). On the physics side, there are different classes that are responsible for different pieces of physics. The NSE class computes NSE given an electron fraction and two of the following properties: temperature, density, entropy, or internal energy. There are also separate classes that are responsible for the EOS and screening corrections.

Since SkyNet is built in an object-oriented fashion, different parts of the code are separated from each other and only interact via well-defined interfaces. This makes SkyNet extremely modular because the implementation of a certain class can be changed or extended, without having to modify the rest of the code. For example, one could easily extend the nuclide library class to support reading nuclear data from a different file format. Since all of the nuclear data are handled by this one class, only this class has to be modified to support the new file format. Furthermore, some classes are implemented as abstract base classes, meaning they only specify the interface for a particular physics module without tying it to a specific implementation. Examples of this are the EOS class and the screening corrections class. For both of these, SkyNet currently

has one implementation, namely the extended Timmes EOS described in Appendix A.2 and the screening corrections discussed in Section 4. One can easily add a new EOS class that implements a different EOS but has the same interface as the abstract EOS base class. This new EOS class then plugs into the existing SkyNet framework. In a similar way, one can add additional screening implementations to SkyNet.

The various classes provided in SkyNet can be used individually through the Python bindings. For instance, one can use the NSE class in Python to compute NSE in various conditions or use the nuclide library class to access the nuclear data and partition functions from Python.

5.2. Nuclear Reaction Libraries

SkyNet supports different types of nuclear reactions. Reactions of the same type or from the same data source are grouped into reaction library classes. The network class contains an arbitrary list of reaction library classes that collectively contain all of the reactions that are evolved in the network. The reaction library classes have a common interface that allows the network to be agnostic as to how the reaction rate is determined. Via this interface, the network can tell the reaction libraries to recompute the reaction rates for a given thermodynamic state (temperature, density, electron fraction, electron degeneracy parameter, etc.) to get the contributions to all $\dot{Y}_i$ from the reactions in the network and to get the contributions to $\partial\dot{Y}_i/\partial Y_j$. This makes SkyNet extremely flexible because many different types of reactions can be evolved at the same time, and furthermore, the data for reactions of the same type can be split across multiple files, allowing the user to quickly switch out certain reactions. Finally, thanks to the abstract interface of reaction library classes, it is easy to add new types of reactions to SkyNet.

The following reaction types of nuclear reactions are currently implemented in SkyNet.

1. Constant: These reactions have a constant rate that does not depend on any properties of the thermodynamic state.
2. REACLIB: These are reactions that come from the REACLIB database (Cyburt et al. 2010). The rates of these reactions are given by parametric fitting formulae that depend on temperature and density.
3. Tabulated: This reaction library contains tabulated β-decay (both β^- and β^+) and electron/positron capture rates based on Fuller et al. (1982) and Langanke & Martínez-Pinedo (2001). The rates are tabulated as a function of temperature and $Y_e\rho$.
4. Neutrino interactions: These are neutrino emission and absorption reactions on free neutrons and protons. The rates are calculated according to Equations (181)–(184) given the electron neutrino and electron antineutrino distribution functions.
5. Arbitrary rate functions: This reaction library contains reactions whose rates are given by arbitrary, user-specified functions. This can be used to quickly test a new or modified reaction rate that can depend on various thermodynamic quantities and also time.

Since the different reaction types and rate sources can be used concurrently in SkyNet, care must be taken to ensure that no reaction rate is contained multiple times in the network, since that would effectively multiply the reaction rate by the number of times it occurs. SkyNet provides a facility to remove all reactions in one reaction library that also occur in another library. However, in some cases, there are supposed to be multiple rates for the same reaction. In this case, the total reaction rate is the sum of the individual rates. REACLIB uses this mechanism to capture the different resonant and non-resonant parts of a reaction rate with its limited fitting formula.

6. Code Verification and Tests

In order to verify the correctness of SkyNet, we compare its results to the results of other existing reaction network codes, specifically WinNet (Winteler 2013) and XNet (Hix & Thielemann 1999), and also to results published in the literature. The scripts and input files to reproduce these code tests are distributed with SkyNet in the directory `examples/code_tests`. SkyNet also has a test suite that contains simple code tests, regression tests, and tests that compare very simple networks to analytic solutions. The main purpose of that test suite is to ensure that changes to the code do not break the functionality or correctness of SkyNet.

6.1. Nuclear Statistical Equilibrium

To verify the NSE solver in SkyNet, we perform a consistency test and comparison to literature results of the NSE abundances computed by SkyNet. We use nuclear masses and partition functions distributed with REACLIB (Cyburt et al. 2010), which contains experimental data where available and finite-range droplet macroscopic model (FRDM; see, e.g., Möller et al. 2016) data otherwise. The temperature-dependent partition functions are from Rauscher & Thielemann (2000).

6.1.1. Consistency Test

In this section, we verify that the abundances computed with the NSE solver in SkyNet are consistent with the strong reactions. We perform a test evolution starting with purely free neutrons and protons and let only strong reactions take place. We use the strong reaction rates from REACLIB and the default fission rates distributed with SkyNet. The network contains 7824 nuclear species, ranging from free neutron and protons to ^{337}Cn ($Z = 112$). We keep the temperature constant at $T = 7$ GK and the density $\rho = 10^9$ g cm^{-3} is also fixed. We pick these values to ensure that the composition achieves NSE within a reasonable amount of time. We set $Y_e = 0.4$, so the initial composition is $Y_\mathrm{n} = 0.6$ and $Y_\mathrm{p} = 0.4$, and since the network does not contain any weak reactions, the electron fraction remains constant at $Y_e = 0.4$. Screening corrections are enabled for both the NSE solver and the network evolution. At every step, we compare the network abundances to the NSE abundances and compute the error ΔY as

$$\Delta Y = \max_i |Y_i^{\mathrm{network}} - Y_i^{\mathrm{NSE}}|. \tag{110}$$

We perform two different network evolutions: one where the strong inverse rates are computed from detailed balance (Section 2.3) and another one where the inverse rates from REACLIB are used. We never use inverse fission reactions.

The results are shown in Figure 6. After evolving the network using detailed balance to compute the inverse rates for 850 time steps, corresponding to $t = 1$ s, the network reaches the NSE composition. The error between NSE and the network composition is $\Delta Y \sim 10^{-11}$ and the deviation of Y_e from 0.4 is on the same level. We note that this is comparable to the mass

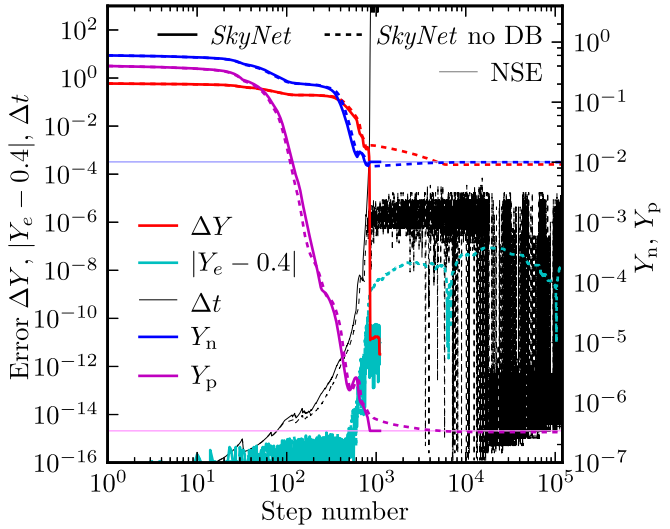

Figure 6. Evolving pure neutrons and protons to NSE with a fixed temperature $T = 7$ GK, density $\rho = 10^9$ g cm^{-3}, and $Y_e = 0.4$. The evolution only includes strong reactions, because weak reactions would change the electron fraction. The horizontal lines show the neutron and proton abundances of the NSE composition. The SkyNet evolutions are done with screening correction turned on. The solid lines are the quantities from the SkyNet evolution where the inverse rates are computed from detailed balance, while the dashed lines are from SkyNet without detailed balance, i.e., the inverse rates are taken from REACLIB. The error ΔY is the maximum abundance difference between the network and the NSE composition. We stop the network evolution without detailed balance after 130,000 time steps, corresponding to 0.053 s of physical time, because the time step Δt remains very small and the error ΔY appears to converge to a few $\times 10^{-4}$. In contrast, the evolution with detailed balance only requires about 850 steps ($\sim$1 s physical time) to reach $\Delta Y \sim 10^{-11}$. We stop that evolution after 1100 steps when it reached $t = 10^{10}$ s.

conservation limit of 10^{-10} that SkyNet uses as the NR iteration convergence criterion. The neutron and proton abundances also match the values from the NSE composition with very high precision. In the subsequent 250 time steps, the network reaches $t = 10^{10}$ s and ΔY decreases another order of magnitude. This demonstrates that the NSE solver in SkyNet and the implementation of detailed balance for the inverse rates are consistent. The NSE compositions computed with SkyNet are indeed the compositions that the network produces if the strong reactions are in equilibrium.

Furthermore, Figure 6 also shows that the inverse rates provided in REACLIB are not completely consistent with the NSE composition that is computed from the nuclear data (masses and partition functions) distributed together with REACLIB. If the REACLIB inverse rates are used ("SkyNet no DB" in Figure 6), the network evolution is extremely slow after about 900 steps. We stopped the network evolution after 130,000 steps at $t \sim 0.053$ s, when it became clear that ΔY converged to 2.5×10^{-4}. The evolution without detailed balance becomes very slow because the inverse rates from REACLIB try to push the composition into a certain equilibrium configuration, but chemical potential balance predicts a different equilibrium composition. This makes the evolution very difficult and keeps the time step between 10^{-15} and 10^{-5} s. Computing the inverse rates from detailed balance so that the inverse rates exactly cancel the forward rates when the chemical potentials balance is therefore necessary for the network evolution to be consistent with NSE (see Section 2.3).

A detailed investigation of the reverse rates in REACLIB reveals that a significant fraction of them were computed with nuclear masses different from the mass model distributed with REACLIB, which we use in SkyNet to compute the inverse rates from detailed balance and to compute NSE. We observe this for the latest REACLIB version (REACLIB V2.2 from 2016 November 14 and also newer pre-release version that is not publicly available yet) as well as previous REACLIB versions. For 74% of the inverse rates, the Q values used in the REACLIB inverse rates differ by 1% or less compared to the Q values computed from our mass model (Equation (33)). About 19% of the Q values agree within 1% to 10%, 5% within 10% to 30%, and almost all the Q values agree within a factor of 2. However, there are some rare cases where the Q value used in REACLIB differs by up to two orders of magnitude from the one given by the mass model used in SkyNet. Fortunately, the impact of the discrepancy between the reverse REACLIB rates and the mass model on the final abundances of a network evolution is very small, as we shall see in Section 6.2. Nevertheless, the test presented in this section highlights the advantage of using detailed balance with the mass model used in the network to compute inverse rates. This is especially important to keep the time step from becoming very small when the composition moves into NSE. Some of the inconsistencies in the inverse rates will be corrected in a future REACLIB version (H. Schatz 2017, private communication). However, because REACLIB is a collection of rates from different sources that use different mass models to compute the rates and their inverses, it seems unlikely that all inverse rates in REACLIB will ever be consistent with a single mass model. We therefore recommend to always directly compute inverse rates from detailed balance with the masses used in the network when consistency with NSE is desired.

6.1.2. Comparison with Published Results

We compare the SkyNet NSE solver to the NSE results with and without electron screening by Seitenzahl et al. (2009). The composition includes 443 nuclides ranging from free neutrons and protons to multiple isotopes of krypton (see Figure 1 in Seitenzahl et al. 2009). We compute NSE with and without screening at a fixed density of $\rho = 5 \times 10^8$ g cm^{-3} and fixed $Y_e = 0.5$ for temperatures ranging from 4 to 10 GK. The results are shown in Figure 7 along with the results from Seitenzahl et al. (2009, Figures 3–6, data used with permission).

We find excellent agreement between the SkyNet results and those presented in Seitenzahl et al. (2009). When screening corrections are included, the deviation between the two results is slightly larger, because Seitenzahl et al. (2009) use a different screening implementation. The effect of the different screening implementation is most pronounced for the proton mass fraction at $T \gtrsim 9$ GK, but even then, the difference is less than 5%. Seitenzahl et al. (2009) use a fit for the screening corrections that has a significant correction even in the weak screening regime at $T \gtrsim 8$ GK. On the other hand, the weak screening correction in SkyNet becomes much smaller at those temperatures. Hence, the differences in the NSE mass fractions are due to the increased disagreement between the different screening corrections as the temperature increases. Furthermore, Seitenzahl et al. (2009) use different nuclear masses, so that could account for the small differences between our results and theirs when screening is turned off.

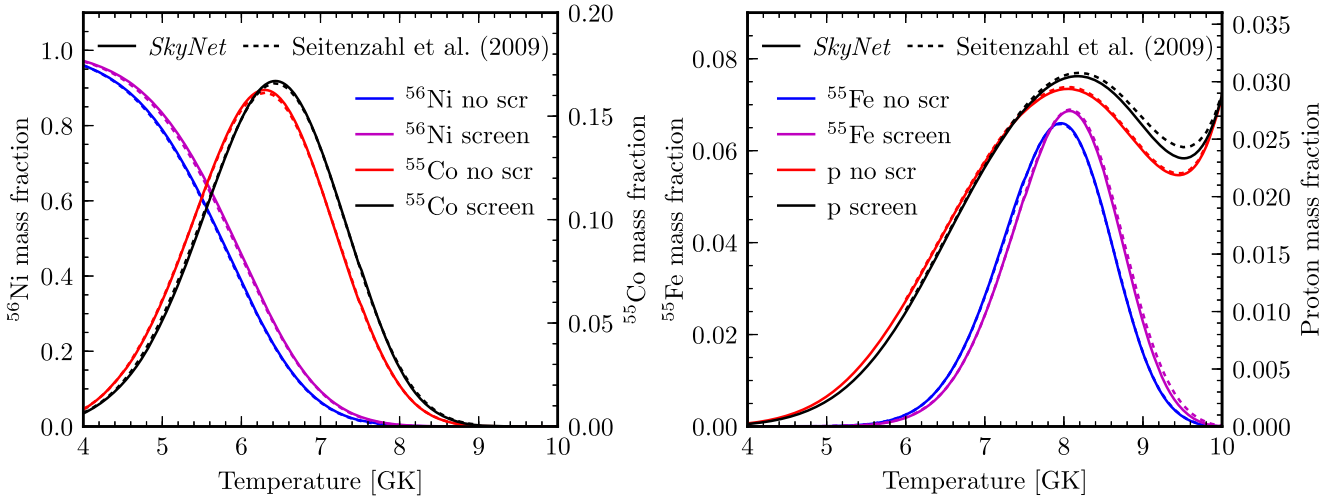

Figure 7. ^{56}Ni, ^{55}Co, ^{55}Fe, and proton mass fractions in an NSE composition with varying temperatures and fixed $\rho = 5 \times 10^8$ g cm^{-3} and $Y_e = 0.5$. The composition includes 443 species and NSE is computed with and without screening corrections. The results are compared to those published in Seitenzahl et al. (2009; data used with permission). We see excellent agreement between SkyNet and the published results. The differences are slightly enhanced when screening is turned on, due to the different screening implementations.

6.2. Network Evolution

In this section, we present comparisons of nucleosynthesis evolutions with SkyNet and other nuclear reaction networks. We compare SkyNet to WinNet and XNet. WinNet was originally developed at the University of Basel by Winteler (2013) based on the earlier BasNet by Thielemann et al. (2011). WinNet has been used by various authors for r-process nucleosynthesis calculations in core-collapse supernovae and neutron star mergers, and to investigate the impact of nuclear physics on the r-process (e.g., Korobkin et al. 2012; Winteler et al. 2012; Eichler et al. 2015; Martin et al. 2015, 2016). XNet was developed at Oak Ridge National Laboratories by Hix & Thielemann (1999) and has been used for r-process nucleosynthesis in accretion disk outflows and neutron star mergers, and for explosive nucleosynthesis in type I X-ray bursts and core-collapse supernovae (e.g., Surman et al. 2006; Fisker et al. 2008; Roberts et al. 2011; Harris et al. 2017).

Since nuclear physics data, such as nuclear masses, partition functions, and nuclear reaction rates, have a significant influence on the nucleosynthesis calculations, we take care in ensuring that exactly the same nuclear physics input data are used for all of the different codes that we consider. However, this means that we are restricted to using the greatest common denominator of nuclear physics data sources that can be used by all codes. For the comparisons in this section, we use the strong and weak reaction rates distributed in REACLIB (Cyburt et al. 2010), neutron-induced fission reactions with symmetric fission fragments from Panov et al. (2010), and spontaneous fission rates calculated from the approximation of Frankel & Metropolis (1947) using the spontaneous fission barriers of Mamdouh et al. (2001). In future versions of SkyNet, we plan to add additional fission reactions and fission fragment distributions. The nuclear masses and partition functions are again the ones distributed with REACLIB, as in Section 6.1.

6.2.1. Neutron-rich r-Process

We run an r-process nucleosynthesis calculation in a neutron-rich environment with all three networks. We use 7836 nuclear species and about 93,000 reactions. The density history is a trajectory from the ejecta of a black hole–neutron star merger (Roberts et al. 2017). The initial composition is NSE with $T = 6.1$ GK, $\rho = 7.4 \times 10^9$ g cm^{-3}, and $Y_e = 0.07$. We run all combinations of screening and self-heating turned on and off. For each case, we perform two separate SkyNet evolutions: one where the inverse rates are computed from detailed balance, and another where the inverse rates from REACLIB are used. We consider these two cases because SkyNet is usually run with inverse rates computed from detailed balance, but WinNet and XNet use the inverse rates from REACLIB, and so we also run SkyNet with those inverse rates for a more direct comparison.

The self-heating method currently implemented in XNet only applies in the case of constant density (J. A. Harris 2017, private communication). Hence, for this r-process computation with an evolving density, we cannot use the self-heating capability of XNet. Instead, to compare XNet to SkyNet and WinNet when self-heating is turned on, we use the SkyNet temperature history (from the SkyNet run without detailed balance) in XNet. However, the temperature provided to XNet has to be limited to a lower bound of 0.01 GK. At temperatures lower than that, the reaction rate fits from REACLIB no longer apply and some of the rates blow up. SkyNet internally also uses a lower bound 0.01 GK for the REACLIB reactions, but the network temperature used in the EOS is allowed to drop below that bound, until the lower limit of the EOS is reached at around 4×10^5 K (this lower bound is due to the tabulated electron/positron part of the Timmes EOS).

Figure 8 shows the results of running the neutron-rich r-process with the three reaction networks with screening and self-heating turned on. We find excellent agreement between the different networks with the temperature evolution of SkyNet and WinNet being virtually indistinguishable (for XNet, we prescribe the SkyNet temperature). The final abundances (at $t = 5 \times 10^8$ s) also agree very well. To compare the results of the three networks quantitatively, we compute the numeric error between the final mass-summed

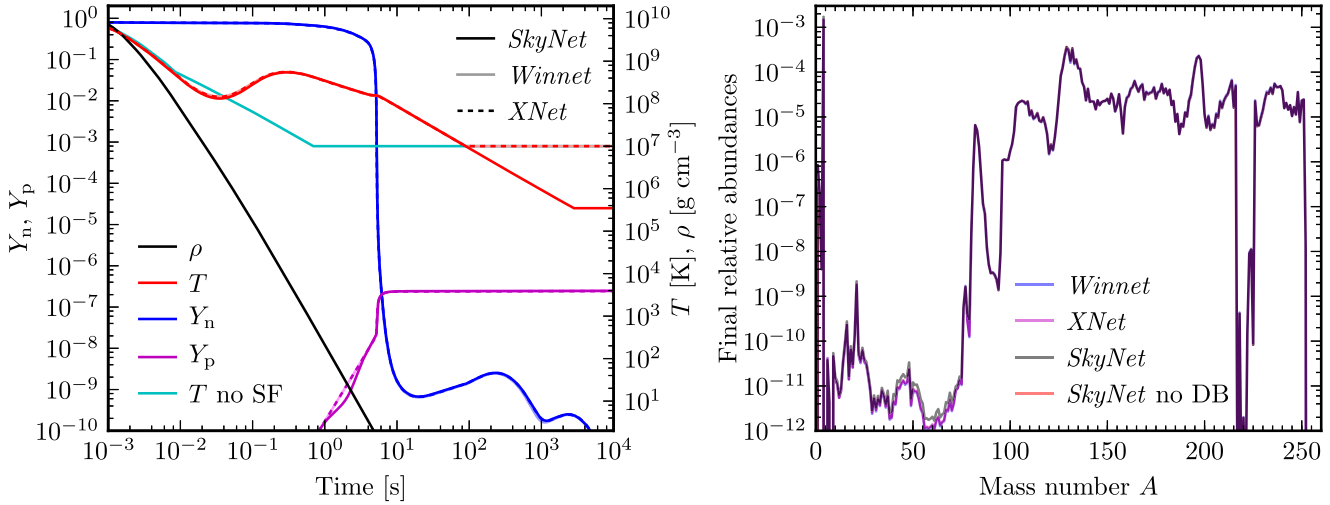

Figure 8. Neutron-rich r-process calculation with three different reaction networks: SkyNet, WinNet, and XNet. Screening corrections are turned on. SkyNet and WinNet evolve the temperature, but XNet's temperature was fixed to that computed by SkyNet (with a lower bound of 0.01 GK). Left: prescribed density ρ as a function of time, resulting temperature T, neutron abundance Y_n, and proton abundance Y_p. For comparison, the temperature without self-heating (SF) from the trajectory is also shown to illustrate the importance of self-heating. The solid dark lines show the SkyNet results, the solid light lines are the WinNet results, and the dashed lines are the XNet results. The three networks agree extremely well with each other, with the lower temperature floor in SkyNet being the largest difference. The small deviation in Y_p at $t \sim 2$ s is because SkyNet uses detailed balance to compute the inverse rates. Detailed balance also accounts for the small temperature difference around $t = 0.01 - 0.1$ s. Right: final abundances as a function of mass number A after 5×10^8 s. Showing two SkyNet results: with detailed balance (DB) and without. We again see excellent agreement between the networks, and the small differences around $A = 50$ are again because of detailed balance. SkyNet without detailed balance matches WinNet and XNet in that region.

Table 1
Errors between the Final Mass-summed Abundances between the Different Networks (Equation (111))

Test Case	Screening	Self-heating	S—SnoDB	S—W	SnoDB—W	S—X	SnoDB—X	X—W
Neutron-rich r-process	yes	yes/no[a]	3.2	5.8	3.4	3.2	0.066	3.4
(Section 6.2.1, Figure 8)	yes	no	33	35	4.5	32	1.8	3.3
	no	yes/no[a]	3.4	5.9	3.4	3.4	0.042	3.4
	no	no	33	36	3.3	33	0.10	3.2
Explosive X-ray burst	yes	yes/no[a]	0.39	2.3	2.1	1.3	1.1	1.0
(Section 6.2.2, Figure 9)	yes	no	13	14	4.0	11	3.5	3.3
	no	yes/no[a]	0.38	2.3	2.0	0.47	0.086	2.0
	no	no	17	18	1.5	18	1.2	0.40
Hydrostatic C/O burn	yes	yes	0.64	0.68	0.57	3.9	4.1	3.9
(Section 6.2.3, Figure 10)	yes	no	0.10	0.22	0.18	0.16	0.22	0.13
	no	yes	0.68	1.5	1.9	4.0	4.4	2.5
	no	no	0.10	0.27	0.17	0.10	0.00036	0.17

Notes. S: SkyNet with detailed balance, SnoDB: SkyNet without detailed balance, W: WinNet, X: XNet. The error measures the average fractional difference between the final abundances. The numbers shown are in percent. The three networks generally agree very well with each other. The error between SkyNet without detailed balance (SnoDB), WinNet (W), and XNet (X) are usually of similar magnitudes and on the few percent level. We also see that using detailed balance for the inverse rates has a big impact on the first two test cases, especially when self-heating is turned off. Since WinNet and XNet do not use detailed balance, the error is bigger when they are compared to SkyNet with detailed balance (S).

[a] Self-heating is turned on in SkyNet and WinNet, but not in XNet, because its self-heating method does not apply in these test cases. Instead, XNet uses the temperature computed by the self-heating SkyNet run without detailed balance (SnoDB).

abundances as

$$\text{error} = \frac{\sum_{A=1}^{A_{\max}} |Y_{\text{net1}}(A) - Y_{\text{net2}}(A)|}{\sum_{A=1}^{A_{\max}} \frac{Y_{\text{net1}}(A) + Y_{\text{net2}}(A)}{2}}, \tag{111}$$

where the mass-summed abundance $Y(A)$ is given by

$$Y(A) = \sum_{\substack{i \text{ where} \\ A_i = A}} Y_i. \tag{112}$$

This error measure is the average absolute difference between the abundance results divided by the average abundances. This effectively measures the fractional error in the final abundances, averaged over all mass numbers A. However, we compute the quotient of the sums rather than the sum of quotients, because the latter would be dominated by tiny abundances ($\sim 10^{-20}$) that may differ by a factor of several between the two networks. This would result in a large overall error, but abundance differences at the 10^{-20} level are not important, even if it is by a factor of several.

Table 1 shows the errors in percent between the different networks. Since this is a neutron-rich environment, we expect that screening plays no important role in the nucleosynthesis evolution. The fact that the errors between the different networks are almost the same regardless whether screening is

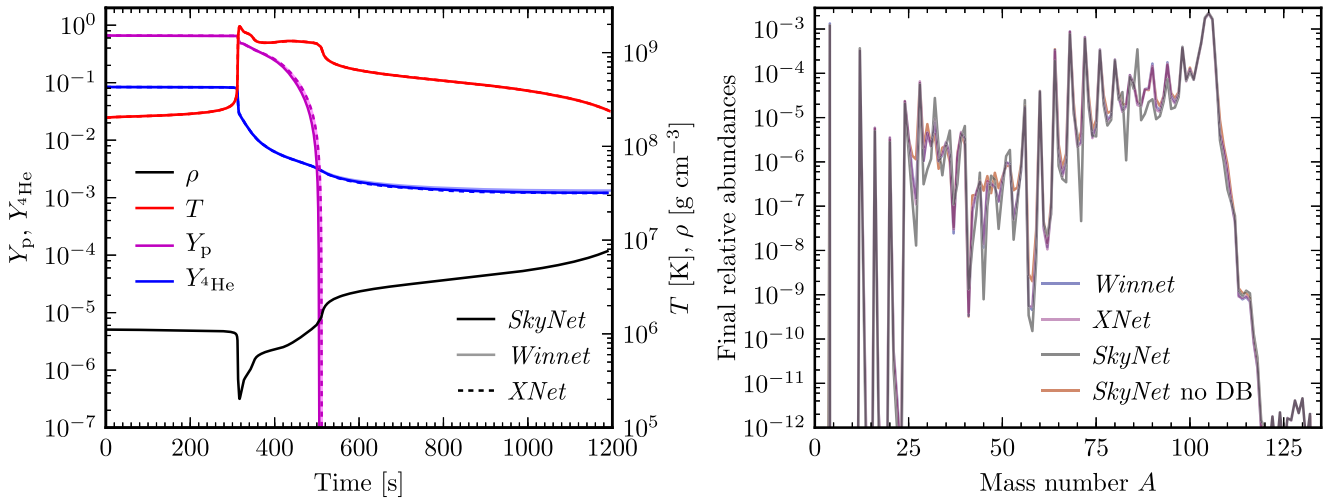

Figure 9. Explosive nucleosynthesis in an X-ray burst with three different reaction networks: SkyNet, WinNet, and XNet. Screening corrections are included, but self-heating is turned off for the computations shown in this figure so that the impact of screening can be presented. We use the temperature and density history from Schatz et al. (2001). Left: prescribed density ρ and temperature T as a function of time, resulting proton abundance Y_p, and helium abundance $Y_{^4He}$. All three networks agree very well with each other. Right: final abundances as a function of mass number A at $t = 1242.6$ s. Showing two SkyNet results: with detailed balance (DB) and without. SkyNet with detailed balance produces final abundances at some specific values of A that differ by up to two orders of magnitude from the other networks. This shows the importance of using detailed balance to compute inverse rates.

turned on or off confirms that screening is not important in this case. Furthermore, the error between SkyNet without detailed balance and WinNet or XNet are comparable to the errors between WinNet and XNet. For example, with screening and self-heating turned on (first row in Table 1), the error between SkyNet without detailed balance and WinNet is 3.4%, while the error between WinNet and XNet is 3.4%, and the error between XNet and SkyNet without detailed balance is 0.066%. SkyNet is closer to XNet in this case because XNet uses the same temperature as SkyNet whereas WinNet evolves its own temperature. This demonstrates that SkyNet produces results that are compatible with WinNet and XNet. The errors between SkyNet and WinNet or XNet are larger if detailed balance is used to compute the inverse rates in SkyNet. For example, again for the first row in Table 1, the error between WinNet and SkyNet with detailed balance is 5.8%, but only 3.4% when compared to SkyNet without detailed balance. This is not surprising, because SkyNet is effectively evolving slightly different reaction rates when inverse rates are computed from detailed balance. It does illustrate, however, that using detailed balance, which produces inverse rates that are consistent with the nuclear masses and partition functions, has a measurable impact and might be a reasonable standard practice. In the self-heating runs, SkyNet is much closer to XNet than WinNet, because XNet uses the temperature from SkyNet.

6.2.2. X-ray Burst

In Figure 9, we show a comparison between the three networks for a different type of trajectory. This trajectory captures the situation of unstable hydrogen burning on the surface of a neutron star, which produces a type I X-ray burst, presented in Schatz et al. (2001). The density and temperature histories as well as the initial and final abundances were graciously provided by Schatz et al. (2001). The temperature starts at 0.2 GK and peaks at 1.9 GK during the burst. The density starts at 1.1×10^6 g cm^{-3}. The initial composition is 66.0% hydrogen (by mass), 33.6% helium, and 0.4% heavier elements, mostly oxygen. For this test, we use a small network containing only 686 species going up to ^{136}Xe and 8400 reactions.

We again see good agreement in Figure 9 between the three networks in the proton and helium abundance evolution (left panel of Figure 9). But there are a handful of mass numbers at which SkyNet with detailed balance produces final abundances that deviate from the other networks by up to two orders of magnitude (right panel of Figure 9). This indicates that it is vital to compute the inverse reaction rates correctly with detailed balance in this scenario. However, the average fractional abundance errors shown in Table 1 are still at the few percent level, and the differences between SkyNet and WinNet or XNet are comparable to the differences between WinNet and XNet. We note that the errors between SkyNet without detailed balance and WinNet or XNet are smaller if screening is turned off. This indicates that screening is somewhat important in this case and we expect the discrepancy between the different codes to increase if screening is turned on due to the different screening implementations. The effect is especially noticeable when comparing SkyNet to XNet with self-heating turned on, because in this case XNet uses the temperature computed from SkyNet, but if screening is switched off, the error between the two codes decreases from 1.1% to 0.086%.

SkyNet's screening implementation is presented in Section 4. WinNet uses a single fit of the two-body screening factor by Chugunov et al. (2007) across all screening regimes. XNet computes the two-body screening function provided by Graboske et al. (1973) for weak and intermediate screening and the one provided by Dewitt & Slattery (1999) for strong screening. XNet then uses a selection rule to select one of the three screening regimes without interpolating between them.

6.2.3. Hydrostatic Carbon–Oxygen Burning

In order to compare the self-heating methods implemented in the three networks, we perform a hydrostatic burn at constant density. We keep $\rho = 10^7$ g cm^{-3} fixed and start with $T = 3$ GK and the initial composition consists of half ^{12}C

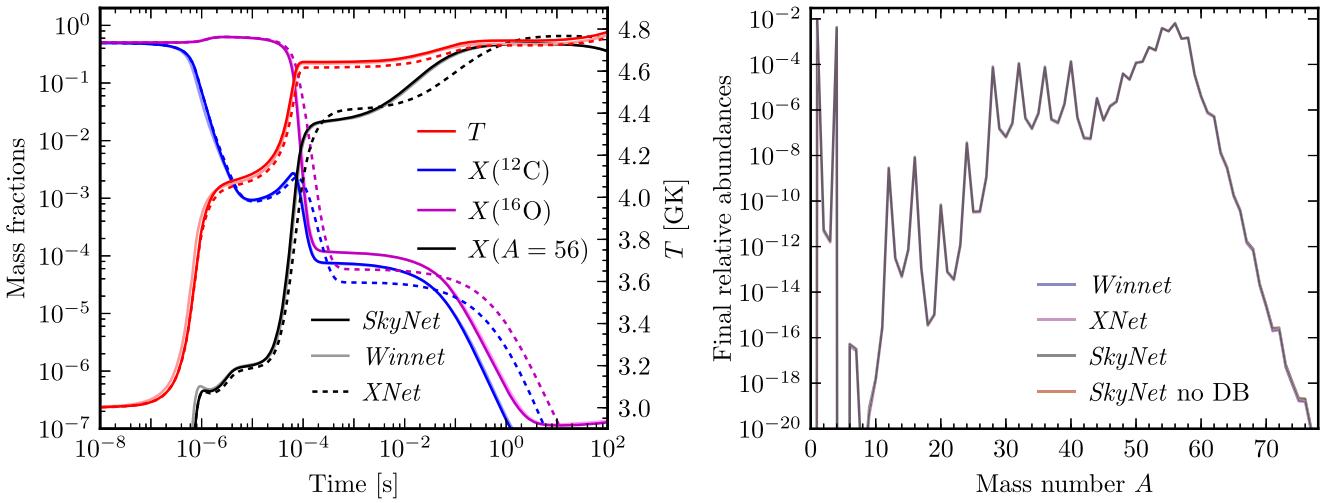

Figure 10. Hydrostatic burning of carbon and oxygen with three different reaction networks: SkyNet, WinNet, and XNet. The density is fixed at $\rho = 10^7$ g cm^{-3} and the evolution starts with $T = 3$ GK and half ^{12}C, half ^{16}O (by mass). Screening and self-heating are enabled in all three networks. Left: resulting temperature T, ^{12}C and ^{16}O mass fractions, and the sum of the mass fractions of all isotopes with $A = 56$. We clearly see the difference in the self-heating implementations. SkyNet and WinNet evolve the entropy and compute the temperature from it, which takes composition changes into account. XNet evolves the temperature directly solely based on the released nuclear binding energy, which becomes small after $t \sim 10^{-4}$ s and so the temperature stops changing in XNet. Right: final abundances as a function of mass number A at $t = 100$ s. Showing two SkyNet results: with detailed balance (DB) and without. All codes produce extremely similar results.

and half ^{16}O (by mass). As a baseline comparison, we also perform non-self-heating runs, where we keep the temperature fixed at 3 GK. The increase in the errors between the networks with self-heating enabled compared to with it disabled must then be due to the difference in the self-heating implementations in the codes. We use a mid-size network containing all nuclides from the full network (Section 6.2.1) with $A \leqslant 100$. This results in a network with 1530 species and 20,000 reactions.

Figure 10 shows the results of this test case with self-heating and screening turned on. We find good qualitative agreement between the three networks, but quantitatively, the differences between XNet and the other two codes are much larger than in the previous test cases. These discrepancies come from the different self-heating implementations in the three codes. WinNet uses the same self-heating method as SkyNet (described in Section 3.2), but WinNet does not include the entropy change due to the electron chemical potential. Also, WinNet uses the original Timmes EOS, which computes the entropy with a single representative heavy ion species, while SkyNet computes the entropy by considering all species in the network separately (Appendix A.2). However, these two differences have virtually no impact on the temperature evolution or the final abundances produced by WinNet and SkyNet. XNet, on the other hand, uses a different self-heating method. It evolves the temperature directly using (J. A. Harris 2017, private communication)

$$\frac{dT}{dt} = \frac{\dot{\epsilon}_{\mathrm{nuc}}}{c_V} = -\frac{1}{c_V}\sum_i \dot{Y}_i \mathcal{M}_i, \tag{113}$$

where c_V is the specific heat capacity at constant volume (provided by the Timmes EOS), $\dot{Y}_i = dY_i/dt$ is the abundance time derivative of species i, and $\mathcal{M}_i$ is the mass excess. As can be seen in the left panel of Figure 10, this method is comparable to the methods in SkyNet and WinNet. Note that XNet is using exactly the same EOS as WinNet. We see only very small differences in the final abundances of the three networks in the right panel of Figure 10.

The differences in the self-heating implementations are also apparent in Table 1. When self-heating is turned on, XNet differs from SkyNet and WinNet by about 4%, and WinNet differs from SkyNet by about 1%. However, when self-heating is disabled, the three networks agree at the 0.2% level, and if screening is turned off, SkyNet without detailed balance and XNet agree to an astounding precision of 0.0004%.

6.3. NSE Evolution Test

To ensure that the NSE evolution mode in SkyNet produces the correct results, we perform a test that evolves a trajectory with and without the NSE evolution mode. Of course, the trajectory must experience some heating that forces the composition into NSE at some point during the evolution, otherwise the NSE evolution mode would not be triggered. We first attempt this test with a trajectory from a neutron star merger accretion disk outflow simulation (Lippuner et al. 2017). That trajectory experiences late-time fallback, which causes a spike in the density that results in late-time heating and forces the composition into NSE. Although SkyNet is able to evolve this trajectory without issues using the NSE evolution mode, when the NSE evolution mode is turned off, SkyNet gets stuck with a time step of $\sim 10^{-16}$ s for at least 350,000 steps at the time when the heating occurs. Thus, we cannot use this trajectory for this test, since we cannot evolve it without the NSE evolution mode. However, this trajectory serves as an illustration of the necessity of the NSE evolution mode in order to evolve certain trajectories.

Since it is challenging to evolve a trajectory without the NSE evolution mode that moves into NSE during the evolution, we use an artificial trajectory that has a temperature peak that is less than 8 GK. In practice, we found that a trajectory with a peak of 7.6 GK can be evolved without the NSE evolution mode, but anything hotter becomes problematic. So, we use an imposed temperature history that starts out at 5.5 GK and remains constant at that value, except for a short peak up to 7.6 GK at 10 s. We keep the density fixed at $\rho = 10^8$ g cm^{-3}. We evolve SkyNet without screening or self-heating, but with

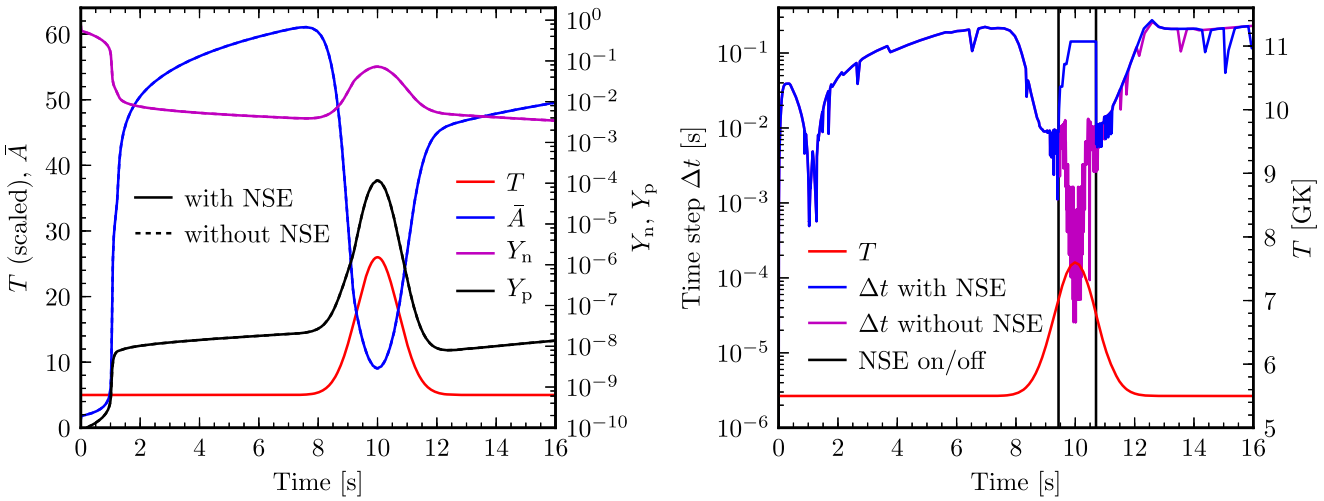

Figure 11. Test of the SkyNet NSE evolution mode. SkyNet is evolved with a constant density of $\rho = 10^8$ g cm^{-3} and a constant temperature of 5.5 GK except for a bump up to 7.6 GK at 10 s. Self-heating and screening corrections are turned off and inverse rates are computed from detailed balance. The initial composition is NSE with $Y_e = 0.1$. Left: the temperature T, average mass number $\bar{A}$, and neutron and proton abundances Y_n and Y_p as a function of time. In the first second or so, neutrons are captured onto seed nuclei and heavy nuclei around the first r-process peak are synthesized with $\bar{A}$ increasing to about 60. Then, at 8 s, as the temperature begins to rise, the heavy nuclei are destroyed again as the material is being forced into NSE. This increases Y_n and Y_p and the average nuclear mass drops to around 10. As the temperature returns back to 5.5 GK, the iron peak is formed and $\bar{A}$ increases to 56 at $T \sim 50$ s, eventually settling around 54. Only the first 16 seconds are shown to highlight the region around $t = 10$ s. We see absolutely no differences between the evolution with and without the NSE evolution mode. Right: the imposed temperature T and resulting time-step size Δt as a function of time showing that using the NSE evolution mode allows SkyNet to evolve more quickly. The vertical black lines indicate the times at which SkyNet decides to turn the NSE evolution mode on and off. As the temperature increases, the composition moves into NSE and the time step decreases because the reaction rates become faster. With the NSE evolution mode, SkyNet can turn off the strong reactions that are all in equilibrium now and hence do not change the composition. The composition is only evolved under the influence of weak reactions that change the electron fraction and entropy. Without the NSE evolution mode, the time step keeps decreasing to a few $\times 10^{-5}$, until the temperature decreases again.

inverse rates from detailed balance, as these are important for consistency with NSE (Section 6.1.1). We use the same full network (7836 species and 93,000 reactions) as in Section 6.2.1. The initial composition is NSE with $Y_e = 0.1$. Figure 11 shows the results of this test. From the left panel, we see that the free neutrons are captured in the first second to make heavy nuclei, raising the average mass number $\bar{A}$ to about 60. The nuclei synthesized are mainly around the first r-process peak and the composition decays toward stability until the temperature starts to rise at around 8 s. The rising temperature forces the material into NSE, which liberates neutrons and protons from nuclei, quickly reducing $\bar{A}$ to around 10. When the temperature drops back to 5.5 GK, the free neutrons and protons are absorbed into nuclei again and the iron peak is formed. In the left panel of Figure 11, there are no visible differences between the SkyNet evolution with and without NSE evolution mode. They produce exactly the same results. The right panel of Figure 11 contains the time step Δt and temperature as a function of time. We see that the time steps with and without the NSE evolution mode are the same until SkyNet turns on the NSE evolution mode when the temperature is sufficiently high. With the NSE evolution mode, SkyNet evolves with $\Delta t \sim 10^{-1}$ s until the temperature drops again and the NSE evolution mode is turned off. Without the NSE evolution mode, however, the time step drops to a few $\times$ 10^{-5} s. After the temperature has returned to 5.5 GK, the time steps in both cases are virtually identical again. Not shown are the final abundances of the two SkyNet evolutions, but we find no discernible differences down to a level of 10^{-30}. The error according to Equation (111) between the two SkyNet evolutions is 0.0098%, indicating that the NSE evolution mode in SkyNet produces correct results, i.e., exactly the same results as would be obtained with the full network, but that the NSE evolution mode prevents the time step from getting stuck at a very small value.

7. Summary and Future Work

We presented the new nuclear reaction network SkyNet and the physics that it currently implements. Details are provided of how the abundance evolution equations implemented in SkyNet are derived from kinetic theory. We discuss how inverse reaction rates are computed with detailed balance and how this is related to NSE. A detailed description is given of the numerical methods used in SkyNet for the network integration and the self-heating evolution that accounts for heating due to nuclear reactions. Further, we show how SkyNet automatically transitions between evolving the full network and evolving only the entropy and electron fraction under the influence of weak reactions when the composition is in NSE and all the strong reactions are in equilibrium. A general treatment of electron screening that computes the screening factors for arbitrary strong reactions from chemical potential corrections that only depend on the nucleus charge and the composition is presented. We then show in detail how SkyNet computes these chemical potential corrections in the weak, strong, and intermediate screening regimes and how it smoothly transitions between the regimes. These screening corrections are also taken into account when computing NSE compositions.

After providing some code implementation details that highlight the modularity and expandability of SkyNet, we present comprehensive code tests and comparisons. The NSE compositions computed by SkyNet are shown to be consistent with the evolved strong reactions, but only if detailed balance is used to compute the inverse rates. Furthermore, we show that SkyNet's NSE results are compatible with results in the

published literature. SkyNet is compared to two other nuclear reaction networks in three different cases: a neutron-rich r-process, a proton-rich explosive X-ray burst, and hydrostatic carbon/oxygen burning. All three tests are conducted with and without electron screening and with and without self-heating. We find that all three networks agree with each other at the few percent level in most cases, although there are some situations where the disagreement is larger due to somewhat different implementations of the physics in the codes. Finally, in the appendices, we discuss the physics of ideal Boltzmann gases and how this is implemented in the SkyNet EOS that accounts for all nuclear species individually. Technical details of how NSE is calculated in SkyNet and how the neutrino interactions are implemented are also presented in the appendices.

We hope that SkyNet will be a useful tool for the nuclear astrophysics community to compute nucleosynthesis in various scenarios. We also hope that the theoretical and experimental nuclear physics communities will find SkyNet useful as a low-barrier entry point to running nucleosynthesis models. SkyNet can be used for testing the impact of newly measured or calculated reaction rates or nuclear properties, or to conduct sensitivity studies in order to determine which nuclides should be the focus of future experiments. SkyNet is available as an open-source software at https://bitbucket.org/jlippuner/skynet. We value any feedback, whether it be bug reports, feature requests, or code contributions.

In the future, we plan to extend the electron screening implementation in SkyNet in a way that screening corrections can be consistently accounted for in the EOS as well. We are also thinking of investigating different screening prescriptions and making them available in SkyNet. Currently, only the first-order backward Euler method is implemented in SkyNet, but we intend to add higher-order integration methods in the future. SkyNet is limited to evolving a one-zone model right now (i.e., there is only one density and temperature). We plan to add support for multiple zones in SkyNet and couple it to existing hydrodynamical simulations. Finally, we plan to investigate offloading some or most of the computations in SkyNet to GPUs, which could significantly speed up the network evolution and might be necessary to efficiently evolve large hydrodynamical simulations that are coupled to SkyNet.

We thank J. Austin Harris and W. Raph Hix for giving us access to XNet, for assisting us with running the code comparison tests with XNet, and for helpful discussion of the test results. We are also very grateful to Moritz Reichert, Dirk Martin, Oleg Korobkin, and Marius Eichler for giving us access to WinNet and for helping us run the code comparisons with it. We thank Hendrik Schatz for providing the X-ray burst trajectories and Ivo Seitenzahl for allowing us to use his NSE data. We are very grateful to Christian D. Ott for carefully reading the manuscript and providing helpful comments and suggestions. We also thank our referee, Friedel Thielemann, for the thoughtful comments and additional reference suggestions. L.R. thanks W. Raph Hix and Stan Woosley for many useful discussions concerning nuclear reaction networks and nucleosynthesis. We are indebted to the authors of the sparse linear solver package PARDISO (Schenk & Gärtner 2004, 2006; Karypis & Kumar 1998) for making their code available for free for academic uses. This work was supported in part by the Sherman Fairchild Foundation and NSF awards NSF CAREER PHY-1151197, TCAN AST-1333520, and AST-1205732. The calculations were performed on the Zwicky computer cluster at Caltech, supported by NSF under MRI award PHY-0960291 and by the Sherman Fairchild Foundation. This work benefited from access to the NSF XSEDE computing network under allocation TG-PHY100033 and to NSF/NCSA Blue Waters under NSF PRAC award ACI-1440083. This work was supported in part by NSF grant PHY-1430152 (JINA Center for the Evolution of the Elements).

Appendix A
Equation of State (EOS)

SkyNet requires an EOS in order to relate different thermodynamic quantities, such as temperature, entropy, chemical potential, etc., to each other. Ions behave as non-relativistic, non-degenerate particles in the majority of situations where nuclear burning occurs and so the EOS in SkyNet treats all ions as non-interacting, non-degenerate, non-relativistic ideal Boltzmann gases. Electrons and positrons, on the other hand, can be both degenerate and relativistic. An important exception to the assumption that the ions are non-interacting is electron screening, which is discussed in detail in Section 4.

In this section, we present a brief summary of the most relevant properties of ideal Boltzmann gases and introduce the notation used in this paper. We also describe the EOS implemented in SkyNet.

A.1. Ideal Boltzmann Gas

The grand partition function $\mathcal{Z}$ of a Maxwell–Boltzmann gas is given by (e.g., Reichl 1980, Section 9.D.3)

$$\ln \mathcal{Z} = \sum_k e^{-\beta(\epsilon_k - \mu)}, \tag{114}$$

where the sum runs over all single-particle states k with energy ϵ_k, $\beta = 1/T$, and μ is the chemical potential. Let the particles be non-relativistic with rest mass m and kinetic energy $E = p^2/(2m)$. Also, let the particles have internal states with excitation energies Δ_l (with respect to the ground state $l = 0$, so $\Delta_0 = 0$) and spins J_l, so that the multiplicity factor is $2J_l + 1$. Thus, a state k is described by the internal state label l and momentum p, and the energy is given by

$$\epsilon_k = \epsilon(l, p) = \frac{p^2}{2m} + m + \Delta_l. \tag{115}$$

Recalling that the momentum phase-space volume element is $V/h^3 d^3p$, we find

$$\begin{aligned}
\ln \mathcal{Z} &= \sum_l (2J_l + 1) \frac{V}{h^3} \int d^3p \; e^{-\beta(p^2/(2m) + m + \Delta_l - \mu)} \\
&= 4\pi \frac{V}{(2\pi)^3} e^{\beta(\mu - m)} \sum_l (2J_l + 1) e^{-\beta\Delta_l} \int_0^\infty dp \; p^2 e^{-\beta p^2/(2m)} \\
&= \frac{V}{2\pi^2} e^{\beta(\mu - m)} G(T) \sqrt{\frac{\pi}{2}} \left(\frac{m}{\beta}\right)^{3/2} \\
&= V G(T) \left(\frac{mT}{2\pi}\right)^{3/2} e^{\beta(\mu - m)},
\end{aligned} \tag{116}$$

where $(2J_l + 1)$ is the multiplicity of the internal state l, we used $\int d^3p = 4\pi \int_0^\infty dp \; p^2$ and $h = 2\pi\hbar = 2\pi$ since $\hbar = 1$,

and we define the internal partition function

$$G(T) = \sum_l (2J_l + 1) e^{-\beta \Delta_l}. \tag{117}$$

Note that the internal partition function is sometimes given normalized to the ground-state spin factor, i.e.,

$$G(T) = (2J_0 + 1) g(T), \tag{118}$$

where J_0 is the ground-state spin of the nuclide and $g(T)$ is a tabulated function (e.g., Rauscher & Thielemann 2000).

The grand potential Ω is defined as

$$\Omega(T, V, \mu) = -T \ln \mathcal{Z} = -VG(T) \left(\frac{m}{2\pi} \right)^{3/2} T^{5/2} e^{\beta(\mu - m)}, \tag{119}$$

and the particle number N, pressure P, entropy S, and internal energy U are given by (e.g., Reichl 1980, Section 9.B.3)

$$N = -\left(\frac{\partial \Omega}{\partial \mu} \right)_{V,T} \tag{120}$$

$$P = -\left(\frac{\partial \Omega}{\partial \mu} \right)_{T,\mu} \tag{121}$$

$$S = -\left(\frac{\partial \Omega}{\partial T} \right)_{V,\mu} \tag{122}$$

$$U = \Omega + TS + \mu N. \tag{123}$$

We find

$$N = -\beta \Omega = VG(T) \left(\frac{mT}{2\pi} \right)^{3/2} e^{\beta(\mu - m)}, \tag{124}$$

which we can solve for the chemical potential μ to find

$$\mu = m + T \ln \left[\frac{n}{G(T)} \left(\frac{2\pi}{mT} \right)^{3/2} \right], \tag{125}$$

where $n = N/V$ is the number density. The pressure P becomes

$$P = -\frac{\Omega}{V} = \frac{NT}{V} = nT, \tag{126}$$

since $\Omega = -NT$. For the entropy S, we obtain

$$\begin{aligned} S &= -\frac{\partial G(T)}{\partial T} \frac{\Omega}{G(T)} - \frac{5}{2} \frac{\Omega}{T} - \Omega \left(-\frac{\mu - m}{T^2} \right) \\ &= -\frac{5}{2} \frac{\Omega}{T} - \frac{\Omega}{T} \left(-\frac{\mu - m}{T} \right) - \frac{\Omega}{T} \frac{\partial \ln G(T)}{\partial \ln T}, \end{aligned} \tag{127}$$

and since $N = -\Omega/T$, the specific entropy per particle $s = S/N$ is

$$s = \frac{5}{2} + \ln \left[\frac{G(T)}{n} \left(\frac{mT}{2\pi} \right)^{3/2} \right] + \frac{\partial \ln G(T)}{\partial \ln T}, \tag{128}$$

where we used Equation (125). Finally, the internal energy per particle is

$$\begin{aligned} u &= \frac{U}{N} = \frac{\Omega}{N} + Ts + \mu \\ &= -\Omega \frac{T}{\Omega} + \frac{5}{2} T - (\mu - m) + T \frac{\partial \ln G(T)}{\partial \ln T} + \mu \\ &= \frac{3}{2} T + m + T \frac{\partial \ln G(T)}{\partial \ln T}. \end{aligned} \tag{129}$$

A.2. Modified Timmes EOS

In the previous section, we found the most relevant thermodynamic properties of a non-interacting, non-relativistic, non-degenerate Boltzmann gas. In this section, we describe the complete EOS implemented in SkyNet. SkyNet uses a modified Timmes EOS developed in Timmes & Arnett (1999) and Timmes & Swesty (2000). The Timmes EOS consists of three independent parts: a photon gas, an arbitrarily degenerate and relativistic electron/positron gas, and a non-degenerate, non-relativistic Boltzmann gas for the heavy ions (Timmes & Arnett 1999). The electron/positron part is implemented via table interpolation of the Helmholtz free energy (Timmes & Swesty 2000).

For the photon gas and electron/positron gas, the code from the original author of the Timmes EOS, which is available at http://cococubed.asu.edu/codes/eos/helmholtz.tbz, is used. That code also provides the electron/positron chemical potential $\eta_{e^-,\text{Timmes}} = \mu_{e^-,\text{Timmes}}/T$, which we need to compute neutrino interactions (Appendix C) and electron screening corrections (Section 4). Note that the electron/positron chemical potential $\mu_{e^-,\text{Timmes}}$ in the Timmes EOS is defined with the electron rest mass subtracted out (Timmes & Arnett 1999, Section 2). The positron chemical potential is

$$\mu_{e^+,\text{Timmes}} = -\mu_{e^-,\text{Timmes}} - 2m_e. \tag{130}$$

So, the electron and positron chemical potentials that include the rest masses are

$$\mu_{e^-} = \mu_{e^-,\text{Timmes}} + m_e = T\eta_{e^-,\text{Timmes}} + m_e, \tag{131}$$

$$\mu_{e^+} = \mu_{e^+,\text{Timmes}} + m_e = -T\eta_{e^-,\text{Timmes}} - m_e = -\mu_{e^-}. \tag{132}$$

For the heavy ions, the Timmes EOS implementation uses a single representative ion species with mass $\bar{A}$ and charge $\bar{Z}$, which are the average mass and charge of all nuclides, respectively. Since SkyNet has the complete composition information at all times, we decided to extend the original Timmes EOS to take into account all ion species individually. Furthermore, we use the expressions derived in the previous section for the ion quantities, which take the internal nuclear partition functions into account.

The overall specific entropy of the system is computed in units of k_B baryon^{-1} as

$$s_\text{tot} = \frac{s_{e^\pm,\text{Timmes}} + s_{\gamma,\text{Timmes}}}{k_\text{B} N_A} + s_\text{ions}, \tag{133}$$

where $s_{e^\pm,\text{Timmes}}$ and $s_{\gamma,\text{Timmes}}$ are the electron/positron and photon entropies provided by the Timmes EOS, respectively. We divide them by $k_\text{B} N_A$, where $N_A \approx 6.022 \times 10^{23}$ baryon g^{-1} is the Avogadro constant, because the Timmes EOS returns the entropies in units of erg g^{-1} K^{-1}. The specific entropy of the ions s_ions is calculated by SkyNet itself according

to Equation (128) as

$$s_{\rm ions} = \sum_i \frac{N_i s_i}{N_{\rm B}} = \sum_i Y_i s_i = \sum_i Y_i \left(\frac{5}{2} + \ln\left[\frac{G_i(T)}{n_i} \left(\frac{m_i T}{2\pi} \right)^{3/2} \right] + \frac{\partial \ln G_i(T)}{\partial \ln T} \right), \quad (134)$$

where the sum runs over all nuclear species labeled by i, N_i is the number of particles of species i, $N_{\rm B}$ is the total number of baryons, and s_i is the entropy per particle of species i given by Equation (128). Recall that the abundance Y_i is (Equation (13))

$$Y_i \equiv \frac{n_i}{n_{\rm B}} = \frac{N_i/V}{N_{\rm B}/V} = \frac{N_i}{N_{\rm B}}, \quad (135)$$

where N_i and $N_{\rm B}$ are the total number of particles species i and the total number of baryons, respectively, and V is the volume. Thus, the abundance Y_i is the fraction of particles of species i compared to the total number of baryons. Note that $N_i s_i$ is the total entropy contribution of species i and so $N_i s_i / N_{\rm B}$ is the entropy per baryon contribution of species i. Also note that

$$n_{\rm B} = \rho N_A, \quad (136)$$

where ρ is the mass density.

In Appendix B.2, we require the partial derivative of the entropy with respect to temperature. From Equation (128), we get

$$\frac{\partial s}{\partial T} = \frac{1}{k_{\rm B} N_A} \left(\frac{\partial s_{e^\pm,\rm Timmes}}{\partial T} + \frac{\partial s_{\gamma,\rm Timmes}}{\partial T} \right) + \frac{\partial s_{\rm ions}}{\partial T}. \quad (137)$$

The first two partial derivatives are provided by the Timmes EOS, and from Equation (134) we find

$$\frac{\partial s_{\rm ions}}{\partial T} = \sum_i Y_i \left(0 + \frac{1}{G_i(T)} \frac{\partial G_i(T)}{\partial T} + \frac{3}{2}\frac{1}{T} + \frac{\partial}{\partial T}\left[\frac{\partial \ln G_i(T)}{\partial \ln T} \right] \right) = \sum_i \frac{Y_i}{T} \left(\frac{3}{2} + \frac{\partial \ln G_i(T)}{\partial \ln T} + \frac{\partial^2 \ln G_i(T)}{\partial (\ln T)^2} \right), \quad (138)$$

since $\partial f / \partial \ln T = T \partial f \partial T$. In the current SkyNet implementation, however, we ignore the second derivative of $\ln G_i(T)$, because the partition functions we currently have available do not have continuous second derivatives. This will be fixed in a future version of SkyNet.

Similar to Equation (133), the specific internal energy is computed as

$$u_{\rm tot} = u_{e^\pm,\rm Timmes} + u_{\gamma,\rm Timmes} + u_{\rm ions} \quad (139)$$

in units of erg g^{-1}. The ion internal energy is computed as

$$u_{\rm ions} = N_A \sum_i Y_i \left[T \left(\frac{3}{2} + \frac{\partial \ln G(T)}{\partial \ln T} \right) - {\rm BE}_i - Z_i (m_n - m_p) \right] + N_A Y_e m_e, \quad (140)$$

where m_n and m_p are the neutron and proton mass, respectively, Z_i is the charge number of nuclide i, and ${\rm BE}_i$ is its binding energy. Note that the sum in the above expression gives the internal energy per baryon, so we multiply by N_A to convert this to the internal energy per gram. We need to add the electron rest mass because it is not accounted for in $u_{e^\pm,\rm Timmes}$ (Timmes & Arnett 1999). The binding energy ${\rm BE}_i$ is defined as

$${\rm BE}_i = N_i m_n + Z_i m_p - m_i, \quad (141)$$

with N_i being the number of neutrons of nuclide i (not to be confused with the same symbol used above for the total number of particles of species i in the composition) and m_i being the rest mass of nuclide i. Thus, the term $-{\rm BE}_i - Z_i(m_n - m_p)$ in Equation (140) is

$$-{\rm BE}_i - Z_i(m_n - m_p) = m_i - N_i m_n - Z_i m_p - Z_i m_n + Z_i m_p = m_i - A_i m_n, \quad (142)$$

where $A_i = Z_i + N_i$ is the mass number of nuclide i. Thus, Equation (140) differs from the expression for the specific internal energy of a single species (Equation (129)) only by the subtraction of $A_i m_n$ from the particle rest mass m_i. Thus, the specific internal energy we calculate is relative to the neutron rest mass, which has the advantage that the numerical value of the specific internal energy is not too large but may be comparable to the thermal energy. However, if we ignored the rest mass altogether, the internal energy would not be conserved under nuclear reactions. Nuclear reactions change particles from one species to another that have different binding energies, and so we have to account for the binding energy and mass difference between neutrons and protons, as we do in Equation (140). Other EOSs use the same convention (e.g., Lattimer & Swesty 1991). Note that we have

$$u_{\rm ions} = N_A \sum_i Y_i (u_i - A_i m_n) = N_A \sum_i Y_i u_i - N_A m_n \sum_i Y_i A_i, \quad (143)$$

where u_i is given by Equation (129). But since $\sum_i Y_i A_i = 1$ (Equation (48)), we find $u_{\rm ions} = N_A \sum_i Y_i u_i - N_A m_n$, which means our definition of specific internal energy only differs by a constant ($N_A m_n c^2 \approx 9.065 \times 10^{20}$ erg g^{-1}) from the specific internal energy we would calculate by using Equation (129) directly.

Currently, the electron screening corrections implemented in SkyNet (Section 4) are not yet included in the modified Timmes EOS. Since screening is implemented as a correction to the ion chemical potential (Equation (125)), it is not straightforward to propagate those corrections to the other thermodynamic quantities of the ions, let alone the electron/positron gas. We plan to incorporate screening into the EOS in a future version of SkyNet.

Appendix B
Calculating NSE

In this section, we show in detail how NSE is computed in SkyNet given a temperature and density (Section B.1) and with an unknown temperature (Appendix B.2).

B.1. From Temperature and Density

The NSE evolution mode requires a robust method for calculating NSE. We have a list of nuclides for which we want

to calculate the NSE composition, given a temperature T, density ρ, and electron fraction Y_e. Recall that NSE is governed by Equation (27):

$$\mu_i = Z_i \mu_p + N_i \mu_n, \tag{144}$$

where μ_i, μ_p, and μ_n are the chemical potentials of the nuclide i, protons, and neutrons, respectively. To make the values of the chemical potentials closer to unity, we introduce a renormalized chemical potential $\hat{\mu}$ given by

$$\hat{\mu}_i = \mu_i - m_i - \mathrm{BE}_i, \tag{145}$$

where BE_i is the binding energy of the nuclide i defined in Equation (141). Recall that

$$\mathrm{BE}_i = Z_i m_p + N_i m_n - m_i, \tag{146}$$

where the proton and neutron masses m_p and m_n are generally chosen such that the binding energies of the neutron and proton are exactly zero. Equation (144) now becomes

$$\begin{aligned} &\hat{\mu}_i + m_i + \mathrm{BE}_i = Z_i \hat{\mu}_p + Z_i m_p + N_i \hat{\mu}_n + N_i m_n \\ \Leftrightarrow\ &\hat{\mu}_i = Z_i \hat{\mu}_p + N_i \hat{\mu}_n, \end{aligned} \tag{147}$$

where we used the definition of BE_i, Equation (146), and the fact that $\mathrm{BE}_p = \mathrm{BE}_n = 0$.

It is always possible to choose any two chemical potentials as the basis vectors and express all other chemical potentials in terms of those two. In terms of the species l and m that have Z_l and Z_m protons and N_l and N_m neutrons, we find

$$\begin{aligned} &\begin{bmatrix} Z_l & N_l \\ Z_m & N_m \end{bmatrix} \cdot \begin{bmatrix} \hat{\mu}_p \\ \hat{\mu}_n \end{bmatrix} = \begin{bmatrix} \hat{\mu}_l \\ \hat{\mu}_m \end{bmatrix} \\ \Leftrightarrow &\begin{bmatrix} \hat{\mu}_p \\ \hat{\mu}_n \end{bmatrix} = \frac{1}{Z_l N_m - Z_m N_l} \begin{bmatrix} N_m & -N_l \\ -Z_m & Z_l \end{bmatrix} \cdot \begin{bmatrix} \hat{\mu}_l \\ \hat{\mu}_m \end{bmatrix}. \end{aligned} \tag{148}$$

And so

$$\begin{aligned} \hat{\mu}_i &= Z_i \hat{\mu}_p + N_i \hat{\mu}_n \\ &= \frac{1}{Z_l N_m - Z_m N_l} \left(Z_i (N_m \hat{\mu}_l - N_l \hat{\mu}_m) + N_i (-Z_m \hat{\mu}_l + Z_l \hat{\mu}_m) \right) \\ &= \frac{Z_i N_m - N_i Z_m}{Z_l N_m - N_l Z_m} \hat{\mu}_l + \frac{Z_i N_l - N_i Z_l}{Z_m N_l - N_m Z_l} \hat{\mu}_m \\ &= \alpha_i \hat{\mu}_l + \beta_i \hat{\mu}_m, \end{aligned} \tag{149}$$

where

$$\alpha_i = \frac{Z_i N_m - N_i Z_m}{Z_l N_m - N_l Z_m} \quad \text{and} \quad \beta_i = \frac{Z_i N_l - N_i Z_l}{Z_m N_l - N_m Z_l}. \tag{150}$$

Clearly, the species l and m must be chosen to have different proton fractions Z/N. However, they do not have to be nuclei in the network. We have had reasonable success with $Z_l = 0$, $N_l = 1$, and $Z_m = -1$, $N_m = 1$.

Using Equation (125), the abundance $Y_i = n_i / n_\mathrm{B}$ in terms of the chemical potential $\hat{\mu}_i$ is given by

$$\begin{aligned} \hat{\mu}_i &= -\mathrm{BE}_i + T \ln \left[\frac{n_i}{G_i(T)} \left(\frac{2\pi}{m_i T} \right)^{3/2} \right] \\ &\Leftrightarrow\ e^{(\hat{\mu}_i + \mathrm{BE}_i)/T} = \frac{Y_i n_\mathrm{B}}{G_i(T)} \left(\frac{2\pi}{m_i T} \right)^{3/2} \\ &\Leftrightarrow\ Y_i = e^{(\hat{\mu}_i + \mathrm{BE}_i)/T} \frac{G_i(T)}{n_\mathrm{B}} \left(\frac{m_i T}{2\pi} \right)^{3/2} \\ &\qquad = e^{\eta_i + \mathrm{BE}_i/T} \frac{G_i(T)}{n_\mathrm{B}} \left(\frac{m_i T}{2\pi} \right)^{3/2}, \end{aligned} \tag{151}$$

where we define $\eta_i = \hat{\mu}_i / T$.

This system of equations is subject to baryon number conservation and charge conservation,

$$f_A = 1 - \sum_i A_i Y_i = 0, \tag{152}$$

$$f_Z = Y_e - \sum_i Z_i Y_i = 0. \tag{153}$$

These equations can be zeroed by a two-dimensional NR iteration, where the Jacobian is given by

$$J_\mathrm{NSE} = \begin{bmatrix} \frac{\partial f_A}{\partial \eta_l} & \frac{\partial f_A}{\partial \eta_m} \\ \frac{\partial f_Z}{\partial \eta_l} & \frac{\partial f_Z}{\partial \eta_m} \end{bmatrix}, \tag{154}$$

so that the chemical potential updates are given by

$$\Delta \boldsymbol{\eta} = -J_\mathrm{NSE}^{-1} \cdot \begin{bmatrix} f_A \\ f_Z \end{bmatrix}. \tag{155}$$

From Equations (152) and (153), we find

$$\frac{\partial f_A}{\partial \eta_l} = -\sum_i A_i \frac{\partial Y_i}{\partial \eta_l} = -\sum_i A_i Y_i \alpha_i, \tag{156}$$

and similarly

$$\frac{\partial f_A}{\partial \eta_m} = -\sum_i A_i Y_i \beta_i, \tag{157}$$

$$\frac{\partial f_Z}{\partial \eta_l} = -\sum_i Z_i Y_i \alpha_i, \tag{158}$$

$$\frac{\partial f_Z}{\partial \eta_m} = -\sum_i Z_i Y_i \beta_i. \tag{159}$$

The trickiest part about calculating NSE is choosing the basis nuclides l and m and the starting guess for $\boldsymbol{\eta} = (\eta_l, \eta_m)$. If one of the basis nuclides is $(Z, N) = (-1, 1)$, then the corresponding η can be set to zero in most cases. To choose the second basis nuclide, compute the chemical potential of the most bound nuclide if it had a mass fraction of 1 and compare this to the chemical potential of the neutron if it had mass fraction 1. The second basis nuclide will be the nuclide corresponding to the larger of those two chemical potentials and the starting guess for that η comes from that chemical potential. Although this method may not work in every case, we have found it to work robustly in a large region of parameter space.

B.2. With an Unknown Temperature

In the previous section, we described how to calculate NSE given a temperature T, density ρ (from which we get the baryon number density $n_\mathrm{B} = N_A\rho$), and electron fraction Y_e. However, there are cases where the temperature is unknown but the entropy s_0 is given instead. In that case, we have an additional unknown variable T, and the additional constraint equation

$$f_s = \frac{s(T, \eta_l, \eta_m)}{s_0} - 1 = 0, \tag{160}$$

where s_0 is the given target entropy and $s(T, \eta_l, \eta_m)$ is the entropy given by the EOS from the current guess for T, η_l, and η_m. The Jacobian becomes

$$J_\mathrm{NSE} = \begin{bmatrix} \frac{\partial f_A}{\partial \eta_l} & \frac{\partial f_A}{\partial \eta_m} & \frac{\partial f_A}{\partial T} \\ \frac{\partial f_Z}{\partial \eta_l} & \frac{\partial f_Z}{\partial \eta_m} & \frac{\partial f_Z}{\partial T} \\ \frac{\partial f_s}{\partial \eta_l} & \frac{\partial f_s}{\partial \eta_m} & \frac{\partial f_s}{\partial T} \end{bmatrix}. \tag{161}$$

Note that Equation (151) gives

$$\frac{\partial Y_i}{\partial T} = \frac{Y_i}{T}\left(\frac{3}{2} - \frac{\mathrm{BE}_i}{T} + \frac{\partial \ln G_i(T)}{\partial \ln T}\right), \tag{162}$$

and so

$$\frac{\partial f_A}{\partial T} = -\sum_i A_i \frac{Y_i}{T}\left(\frac{3}{2} - \frac{\mathrm{BE}_i}{T} + \frac{\partial \ln G_i(T)}{\partial \ln T}\right), \tag{163}$$

$$\frac{\partial f_Z}{\partial T} = -\sum_i Z_i \frac{Y_i}{T}\left(\frac{3}{2} - \frac{\mathrm{BE}_i}{T} + \frac{\partial \ln G_i(T)}{\partial \ln T}\right). \tag{164}$$

Recall that the entropy is calculated as (Equation (133))

$$s = s_{e^\pm} + s_\gamma + s_\mathrm{ions}. \tag{165}$$

The EOS provides $\partial s/\partial T$ (Equation (137)), so

$$\frac{\partial f_s}{\partial T} = \frac{1}{s_0}\frac{\partial s}{\partial T} + \frac{1}{s_0}\sum_i \frac{\partial s}{\partial Y_i}\frac{\partial Y_i}{\partial T}. \tag{166}$$

The electron entropy $s_{e^\pm}$ and photon entropy s_γ only depend on the temperature and electron fraction. Thus, they do not depend on the composition $\boldsymbol{Y}$ and thus also not on η_l and η_m. The ion entropy is calculated as (Equation (134))

$$s_\mathrm{ion} = \sum_i Y_i\left(\frac{5}{2} + \ln\left[\frac{G_i(T)}{n_\mathrm{B} Y_i}\left(\frac{m_i T}{2\pi}\right)^{3/2}\right] + \frac{\partial \ln G_i(T)}{\partial \ln T}\right), \tag{167}$$

so

$$\begin{aligned}\frac{\partial s}{\partial Y_i} &= \frac{5}{2} + \ln\left[\frac{G_i(T)}{n_\mathrm{B} Y_i}\left(\frac{m_i T}{2\pi}\right)^{3/2}\right] \\ &\quad + \frac{\partial \ln G_i(T)}{\partial \ln T} + Y_i\left(-\frac{1}{Y_i}\right) \\ &= \frac{3}{2} + \ln\left[\frac{G_i(T)}{n_\mathrm{B} Y_i}\left(\frac{m_i T}{2\pi}\right)^{3/2}\right] + \frac{\partial \ln G_i(T)}{\partial \ln T}.\end{aligned} \tag{168}$$

From Equation (151), we get

$$\ln\left[\frac{G_i(T)}{n_\mathrm{B} Y_i}\left(\frac{m_i T}{2\pi}\right)^{3/2}\right] = -\left(\eta_i + \frac{\mathrm{BE}_i}{T}\right). \tag{169}$$

Combining the above with Equation (162) yields

$$\begin{aligned}\frac{\partial f_s}{\partial T} &= \frac{1}{s_0}\frac{\partial s}{\partial T} + \frac{1}{s_0}\sum_i\left(\frac{3}{2} - \left(\eta_i + \frac{\mathrm{BE}_i}{T}\right)\right. \\ &\quad \left. + \frac{\partial \ln G_i(T)}{\partial \ln T}\right)\frac{Y_i}{T}\left(\frac{3}{2} - \frac{\mathrm{BE}_i}{T} + \frac{\partial \ln G_i(T)}{\partial \ln T}\right),\end{aligned} \tag{170}$$

where the first partial derivative is provided by the EOS (Equation (137)). We also find

$$\begin{aligned}\frac{\partial f_s}{\partial \eta_l} &= \frac{1}{s_0}\sum_i \frac{\partial s}{\partial Y_i}\frac{\partial Y_i}{\partial \eta_l} \\ &= \frac{1}{s_0}\sum_i\left(\frac{3}{2} - \left(\eta_i + \frac{\mathrm{BE}_i}{T}\right) + \frac{\partial \ln G_i(T)}{\partial \ln T}\right)Y_i\alpha_i,\end{aligned} \tag{171}$$

and similarly

$$\frac{\partial f_s}{\partial \eta_m} = \frac{1}{s_0}\sum_i\left(\frac{3}{2} - \left(\eta_i + \frac{\mathrm{BE}_i}{T}\right) + \frac{\partial \ln G_i(T)}{\partial \ln T}\right)Y_i\beta_i. \tag{172}$$

Unfortunately, the NR iterations with three variables are much less stable than if the temperature is fixed, unless a good initial guess for the temperature is available. For this reason, if NSE is computed from a given entropy and density, SkyNet first uses the bisection method (e.g., Burden et al. 2015, Section 2.1) to find a good guess for the temperature. The bisection attempts to find a guess temperature such that Equation (160) is close to zero. Then, the NR iterations are performed as described in this section, which may lead to a temperature that satisfies the three constraint equations better than the guess temperature found by the bisection method. However, it can also happen that the bisection already found the best temperature.

If NSE needs to be calculated from a given temperature, entropy, and electron fraction, then the bisection method is used to find the density that produces the desired entropy. Similarly, if the internal energy, density, and electron fraction are given, SkyNet uses the bisection method to find the temperature that produces an NSE distribution with the desired internal energy.

Appendix C
Neutrino Interaction Reactions

The rate for a two-particle charged current weak interaction is given by (see Equation (7))

$$\begin{aligned}\lambda_w = \frac{1}{n_2} g_1 \int \frac{d^3k_1}{(2\pi)^3} g_2 \int \frac{d^3k_2}{(2\pi)^3} \int \frac{d^3k_3}{(2\pi)^3} \int \frac{d^3k_4}{(2\pi)^3} \\ \times \delta^{(4)}(k_1^\mu + k_2^\mu - k_3^\mu - k_4^\mu) r_w f_1 f_2 (1 - f_3)(1 - f_4),\end{aligned} \tag{173}$$

where particles [1] and [3] are the incoming and outgoing neutrino and lepton, and particles [2] and [4] are the incoming and outgoing nucleons. Under the astrophysical conditions relevant for reaction networks (see, e.g., Reddy et al. 1998), we

have

$$r_w \approx (2\pi)^4 G_F^2 (g_V^2 + 3g_A^2)(1 + h_{wm} E_3), \tag{174}$$

where G_F is the Fermi coupling constant, g_V and g_A are the vector and axial vector couplings of the weak current to the nucleons, and the energy-dependent correction factor $(1 + h_{wm}E_3)$ comes from weak magnetism and recoil corrections (Horowitz 2002). Due to the large mass of the nucleons relative to the energy scale of neutrinos emitted from sites undergoing nuclear burning, we can assume there is no momentum transfer from the nucleons to the leptons. Also neglecting final state nucleon blocking, we then have

$$\lambda_w = G_F^2 (g_V^2 + 3g_A^2) g_1 \int \frac{d^3k_1}{(2\pi)^3} \int \frac{d^3k_3}{(2\pi)^3} \times f_1 (1 - f_3) 2\pi \delta(E_1 - E_3 + q_0)(1 + h_{wm} E_3), \tag{175}$$

where q_0 is the energy difference between the incoming and outgoing nucleons. The angular integrals in momentum space are trivially integrated. We have $E_i dE_i = k_i dk_i$ and the delta function gets rid of the integral over k_3. This gives

$$\lambda_w = G_F^2 (g_V^2 + 3g_A^2) \frac{g_1}{2\pi^3} \int_0^\infty dE_3 k_1 E_1 k_3 E_3 \times (1 + h_{wm} E_3) \theta(E_1 - m_1) f_1 (1 - f_3), \tag{176}$$

where $E_1 = E_3 - q_0$, $k_1 = \sqrt{E_1^2 - m_1^2}$, and $\theta(x) = 1$ if $x > 0$ and 0 otherwise.

SkyNet contains neutrino interactions on free nucleons. Currently, the following reactions are implemented:

$$\lambda_{\rm ec} : \mathrm{p} + e^- \rightarrow \mathrm{n} + \nu_e, \tag{177}$$

$$\lambda_{\rm pc} : \mathrm{n} + e^+ \rightarrow \mathrm{p} + \bar{\nu}_e, \tag{178}$$

$$\lambda_{\nu_e} : \mathrm{n} + \nu_e \rightarrow \mathrm{p} + e^-, \tag{179}$$

$$\lambda_{\bar{\nu}_e} : \mathrm{p} + \bar{\nu}_e \rightarrow \mathrm{n} + e^+. \tag{180}$$

Thus, we compute

$$\lambda_{\rm ec} = C \int_{\omega_{\rm ec}}^\infty dE\, E \sqrt{E^2 - m_e^2} (E - Q_{\rm ec})^2 (1 + E h_{wm}) \times f_e(E, \mu_e)(1 - f_{\nu_e}(E - Q_{\rm ec}, \mu_{\nu_e})), \tag{181}$$

$$\lambda_{\rm pc} = C \int_{\omega_{\rm pc}}^\infty dE\, E \sqrt{E^2 - m_e^2} (E - Q_{\rm pc})^2 \times (1 + E h_{wm}) f_p(E, -\mu_e)(1 - f_{\bar{\nu}_e}(E - Q_{\rm pc}, \mu_{\bar{\nu}_e})), \tag{182}$$

$$\lambda_{\nu_e} = C \int_{\omega_{\rm ec}}^\infty dE\, E \sqrt{E^2 - m_e^2} (E - Q_{\rm ec})^2 (1 + E h_{wm}) \times (1 - f_e(E, \mu_e)) f_{\nu_e}(E - Q_{\rm ec}, \mu_{\nu_e}), \tag{183}$$

$$\lambda_{\bar{\nu}_e} = C \int_{\omega_{\rm pc}}^\infty dE\, E \sqrt{E^2 - m_e^2} (E - Q_{\rm pc})^2 (1 + E h_{wm}) \times (1 - f_p(E, -\mu_e)) f_{\bar{\nu}_e}(E - Q_{\rm pc}, \mu_{\bar{\nu}_e}), \tag{184}$$

where $Q_{\rm ec} = -Q_{\rm pc} = m_n - m_p = 1.29333$ MeV, $\omega_x = \max(m_e, Q_x)$ for $x = $ ec or $x = $ pc, f_e and f_p are the electron and positron distribution functions with the electron chemical potential μ_e given by Equation (131), and f_{ν_e} and $f_{\bar{\nu}_e}$ are the electron neutrino and antineutrino distributions functions, which are usually Fermi–Dirac with $\mu_{\nu_e} = \mu_{\bar{\nu}_e} = 0$, but could be set to something else, too. We also use the Fermi–Dirac distribution for the electrons and positrons, hence

$$f_{e,p}(E, \mu) = \frac{1}{e^{\beta(E-\mu)} + 1}, \tag{185}$$

where $\beta = 1/T$. The factor C is given by (Arcones et al. 2010)

$$C = \frac{B \ln 2}{K m_e^5}, \tag{186}$$

where the matrix element is $B = g_V^2 + 3g_A^2 = 5.76$ and $K = 6144$ s.

Note that the factor $(E - Q_x)$ in Equations (181)–(184) is the (anti) neutrino energy. We neglect nucleon recoils so that $E_{\nu_e} = E + m_p - m_n = E - Q_{\rm ec}$ for electron capture and neutrino absorption, and for positron capture and antineutrino absorption, we get $E_{\bar{\nu}_e} = E + m_n - m_p = E + Q_{\rm ec} = E - Q_{\rm pc}$. Therefore, to compute the neutrino heating or cooling rates due to these reactions, we simply multiply the integrand by another factor of $(E - Q_x)$, and we get

$$\dot{\epsilon}_{\rm ec} = C \int_{\omega_{\rm ec}}^\infty dE\, E \sqrt{E^2 - m_e^2} (E - Q_{\rm ec})^3 \times (1 + E h_{wm}) f_e(E, \mu_e)(1 - f_{\nu_e}(E - Q_{\rm ec}, \mu_{\nu_e})), \tag{187}$$

$$\dot{\epsilon}_{\rm pc} = C \int_{\omega_{\rm pc}}^\infty dE\, E \sqrt{E^2 - m_e^2} (E - Q_{\rm pc})^3 (1 + E h_{wm}) \times f_p(E, -\mu_e)(1 - f_{\bar{\nu}_e}(E - Q_{\rm pc}, \mu_{\bar{\nu}_e})), \tag{188}$$

$$\dot{\epsilon}_{\nu_e} = -C \int_{\omega_{\rm ec}}^\infty dE\, E \sqrt{E^2 - m_e^2} (E - Q_{\rm ec})^3 (1 + E h_{wm}) \times (1 - f_e(E, \mu_e)) f_{\nu_e}(E - Q_{\rm ec}, \mu_{\nu_e}), \tag{189}$$

$$\dot{\epsilon}_{\bar{\nu}_e} = -C \int_{\omega_{\rm pc}}^\infty dE\, E \sqrt{E^2 - m_e^2} (E - Q_{\rm pc})^3 (1 + E h_{wm}) \times (1 - f_p(E, -\mu_e)) f_{\bar{\nu}_e}(E - Q_{\rm pc}, \mu_{\bar{\nu}_e}), \tag{190}$$

where the negative sign for the (anti) neutrino absorption reactions comes from the fact that in those reactions, the neutrino energies are absorbed, and they thus provide cooling instead of heating. The total neutrino heating/cooling rate is thus

$$\dot{\epsilon}_\nu = \dot{\epsilon}_{\rm ec} + \dot{\epsilon}_{\rm pc} + \dot{\epsilon}_{\nu_e} + \dot{\epsilon}_{\bar{\nu}_e}. \tag{191}$$

The integrals shown in this section are evaluated numerically in SkyNet using the adaptive QAG integration routines provided by the GNU Scientific Library (see footnote 12). As usual, all of the reaction rates and heating rates need to be multiplied by the product of reactant abundances. So, the electron capture and antineutrino absorption rates are multiplied by Y_p and the positron capture and neutrino absorption rates are multiplied by Y_n.

Alternatively, instead of computing the rates from the integrals provided here, one can also specify the rates $\lambda_{\rm ec}$, $\lambda_{\rm pc}$, λ_{ν_e}, and $\lambda_{\bar{\nu}_e}$ directly as a function of time, and SkyNet will use these externally given rates. In that case, the neutrino heating/cooling rate also has to be specified directly. This capability is useful if the (anti) neutrino absorption and emission rates are computed in a hydrodynamical simulation and the same rates should be used for the nucleosynthesis calculations in SkyNet for consistency.

ORCID iDs

Jonas Lippuner https://orcid.org/0000-0002-5936-3485
Luke F. Roberts https://orcid.org/0000-0001-7364-7946

References

Arcones, A., & Martínez-Pinedo, G. 2011, PhRvC, 83, 045809
Arcones, A., Martínez-Pinedo, G., Roberts, L. F., & Woosley, S. E. 2010, A&A, 522, A25
Arnett, D. 1996, Supernovae and Nucleosynthesis (Princeton, NJ: Princeton Univ. Press)
Arnett, W. D. 1977, ApJ, 218, 815
Arnett, W. D., & Truran, J. W. 1969, ApJ, 157, 339
Bader, G., & Deuflhard, P. 1983, NuMat, 41, 373
Barnes, J., Kasen, D., Wu, M.-R., & Martínez-Pinedo, G. 2016, ApJ, 829, 110
Bauswein, A., Goriely, S., & Janka, H.-T. 2013, ApJ, 773, 78
Bethe, H. A. 1939, PhRv, 55, 434
Blinnikov, S. I., & Panov, I. V. 1996, AstL, 22, 39
Brachwitz, F., Dean, D. J., Hix, W. R., et al. 2000, ApJ, 536, 934
Bravo, E., & García-Senz, D. 1999, MNRAS, 307, 984
Bressan, A., Marigo, P., Girardi, L., et al. 2012, MNRAS, 427, 127
Brett, S., Bentley, I., Paul, N., Surman, R., & Aprahamian, A. 2012, EPJA, 48, 184
Brock, B., Belt, A., Billings, J. J., & Guidry, M. 2015, JCoPh, 302, 591
Brown, L. S., & Sawyer, R. F. 1997, RvMP, 69, 411
Burbidge, E. M., Burbidge, G. R., Fowler, W. A., & Hoyle, F. 1957, RvMP, 29, 547
Burden, R. L., Faires, J. D., & Burden, A. M. 2015, Numerical Analysis (10th ed.; Boston, MA: Cengage Learning, Inc.)
Buss, O., Gaitanos, T., Gallmeister, K., et al. 2012, PhR, 512, 1
Chen, Y. C., Simien, C. E., Laha, S., et al. 2004, PhRvL, 93, 265003
Chugunov, A. I., Dewitt, H. E., & Yakovlev, D. G. 2007, PhRvD, 76, 025028
Clayton, D. D. 1968, Principles of Stellar Evolution and Nucleosynthesis (Chicago, IL: Univ. Chicago Press)
Coc, A., Goriely, S., Xu, Y., Saimpert, M., & Vangioni, E. 2012, ApJ, 744, 158
Cyburt, R. H., Amthor, A. M., Ferguson, R., et al. 2010, ApJS, 189, 240
Cyburt, R. H., Fields, B. D., Olive, K. A., & Yeh, T.-H. 2016, RvMP, 88, 015004
Danielewicz, P., & Bertsch, G. F. 1991, NuPhA, 533, 712
Dewitt, H., & Slattery, W. 1999, CoPP, 39, 97
Dewitt, H. E., Graboske, H. C., & Cooper, M. S. 1973, ApJ, 181, 439
Eichler, M., Arcones, A., Kelic, A., et al. 2015, ApJ, 808, 30
Engstler, S., Krauss, A., Neldner, K., et al. 1988, PhLB, 202, 179
Farouqi, K., Kratz, K.-L., Pfeiffer, B., et al. 2010, ApJ, 712, 1359
Feger, E. D. 2011, PhD Thesis, Univ. Tennessee
Fernández, R., Foucart, F., Kasen, D., et al. 2017, CQGra, 34, 154001
Fisker, J. L., Schatz, H., & Thielemann, F.-K. 2008, ApJS, 174, 261
Frankel, S., & Metropolis, N. 1947, PhRv, 72, 914
Freiburghaus, C., Rembges, J.-F., Rauscher, T., et al. 1999a, ApJ, 516, 381
Freiburghaus, C., Rosswog, S., & Thielemann, F.-K. 1999b, ApJL, 525, L121
Fuller, G. M., Fowler, W. A., & Newman, M. J. 1982, ApJS, 48, 279
Gatu Johnson, M., Zylstra, A. B., Bacher, A., et al. 2017, PhPl, 24, 041407
Gear, C. W. 1971, Numerical Initial value Problems in Ordinary Differential Equations (Engelwood Cliffs, NJ: Prentice-Hall)
Goriely, S., Bauswein, A., & Janka, H.-T. 2011, ApJL, 738, L32
Goriely, S., Hilaire, S., & Koning, A. J. 2008, A&A, 487, 767
Graboske, H. C., Dewitt, H. E., Grossman, A. S., & Cooper, M. S. 1973, ApJ, 181, 457
Guidry, M. 2012, JCoPh, 231, 5266
Guidry, M. W., Billings, J. J., & Hix, W. R. 2013a, CS&D, 6, 015003
Guidry, M. W., Budiardja, R., Feger, E., et al. 2013b, CS&D, 6, 015001
Guidry, M. W., & Harris, J. A. 2013, CS&D, 6, 015002
Harris, J., Hix, W. R., Chertkow, M. A., et al. 2014, in Proc. XIII Nuclei in the Cosmos (NIC XIII), Posters (Trieste: SISSA), 99
Harris, J. A., Hix, W. R., Chertkow, M. A., et al. 2017, ApJ, 843, 2
Hauser, W., & Feshbach, H. 1952, PhRv, 87, 366
Hayashi, C., Hōshi, R., & Sugimoto, D. 1962, PThPS, 22, 1
Heger, A., & Woosley, S. E. 2010, ApJ, 724, 341
Hillebrandt, W., Kromer, M., Röpke, F. K., & Ruiter, A. J. 2013, FrPhy, 8, 116
Hix, W. R., & Meyer, B. S. 2006, NuPhA, 777, 188
Hix, W. R., & Thielemann, F. K. 1999, JCoAM, 109, 321
Hoffman, R. D., Woosley, S. E., & Qian, Y.-Z. 1997, ApJ, 482, 951
Hofmeister, E., Kippenhahn, R., & Weigert, A. 1964, ZAp, 59, 215
Holmes, J. A., Woosley, S. E., Fowler, W. A., & Zimmerman, B. A. 1976, ADNDT, 18, 305
Horowitz, C. J. 2002, PhRvD, 65, 043001
Iben, I., Jr. 1967, ARA&A, 5, 571
Ichimaru, S., & Utsumi, K. 1984, ApJ, 278, 382
Iliadis, C., Champagne, A., José, J., Starrfield, S., & Tupper, P. 2002, ApJS, 142, 105
Itoh, N., Totsuji, H., & Ichimaru, S. 1977, ApJ, 218, 477
Itoh, N., Totsuji, H., Ichimaru, S., & Dewitt, H. E. 1979, ApJ, 234, 1079
Iwamoto, K., Brachwitz, F., Nomoto, K., et al. 1999, ApJS, 125, 439
Jones, S., Hirschi, R., Pignatari, M., et al. 2015, MNRAS, 447, 3115
José, J. 2016, Stellar Explosions: Hydrodynamics and Nucleosynthesis (Boca Raton, FL: CRC Press, Taylor and Francis)
José, J., & Hernanz, M. 1998, ApJ, 494, 680
Just, O., Bauswein, A., Pulpillo, R. A., Goriely, S., & Janka, H.-T. 2015, MNRAS, 448, 541
Käppeler, F., Gallino, R., Bisterzo, S., & Aoki, W. 2011, RvMP, 83, 157
Karypis, G., & Kumar, V. 1998, SIAM Journal on Scientific Computing, 20, 359
Korobkin, O., Rosswog, S., Arcones, A., & Winteler, C. 2012, MNRAS, 426, 1940
Langanke, K., & Martínez-Pinedo, G. 2001, ADNDT, 79, 1
Lattimer, J. M., & Swesty, F. D. 1991, NuPhA, 535, 331
Leung, S.-C., Chu, M.-C., & Lin, L.-M. 2015, MNRAS, 454, 1238
Limongi, M., & Chieffi, A. 2003, ApJ, 592, 404
Lippuner, J., Fernández, R., Roberts, L. F., et al. 2017, MNRAS, 472, 904
Lippuner, J., & Roberts, L. F. 2015, ApJ, 815, 82
Lippuner, J., & Roberts, L. F. 2017a, SkyNet: A Modular Nuclear Reaction Network Library, Zenodo, doi:10.5281/zenodo.1008754
Lippuner, J., & Roberts, L. F. 2017b, SkyNet: Modular Nuclear Reaction Network Library, Astrophysics Source Code Library, ascl:1710.005
Longland, R., Martin, D., & José, J. 2014, A&A, 563, A67
Lunney, D., Pearson, J. M., & Thibault, C. 2003, RvMP, 75, 1021
Maeder, A., & Meynet, G. 2000, ARA&A, 38, 143
Mamdouh, A., Pearson, J. M., Rayet, M., & Tondeur, F. 2001, NuPhA, 679, 337
Martin, D., Arcones, A., Nazarewicz, W., & Olsen, E. 2016, PhRvL, 116, 121101
Martin, D., Perego, A., Arcones, A., et al. 2015, ApJ, 813, 2
Mendoza-Temis, J. D. J., Wu, M.-R., Langanke, K., et al. 2015, PhRvC, 92, 055805
Meyer, B. S., & Adams, D. C. 2007, M&PSA, 42, 5215
Möller, P., Pfeiffer, B., & Kratz, K.-L. 2003, PhRvC, 67, 055802
Möller, P., Sierk, A. J., Ichikawa, T., & Sagawa, H. 2016, ADNDT, 109, 1
Müller, E. 1986, A&A, 162, 103
Mumpower, M. R., McLaughlin, G. C., & Surman, R. 2012, PhRvC, 85, 045801
Mumpower, M. R., Surman, R., McLaughlin, G. C., & Aprahamian, A. 2016, PrPNP, 86, 86
Nishimura, N., Hirschi, R., Rauscher, T., Murphy, A. S. J., & Cescutti, G. 2017, MNRAS, 469, 1752
Nishimura, N., Takiwaki, T., & Thielemann, F.-K. 2015, ApJ, 810, 109
Nollett, K. M., & Burles, S. 2000, PhRvD, 61, 123505
Nomoto, K., Iwamoto, K., Nakasato, N., et al. 1997, NuPhA, 621, 467
Orlov, A. V., Ivanchik, A. V., & Varshalovich, D. A. 2000, A&AT, 19, 375
Panov, I. V., Blinnikov, S. I., & Thielemann, F.-K. 2001, AstL, 27, 239
Panov, I. V., Korneev, I. Y., Rauscher, T., et al. 2010, A&A, 513, A61
Panov, I. V., Ptitsyn, D. A., & Chechetkin, V. M. 1995, AstL, 21, 185
Parikh, A., José, J., Sala, G., & Iliadis, C. 2013, PrPNP, 69, 225
Paxton, B., Bildsten, L., Dotter, A., et al. 2011, ApJS, 192, 3
Perego, A., Rosswog, S., Cabezón, R. M., et al. 2014, MNRAS, 443, 3134
Peskin, M. E., & Schroeder, D. V. 1995, An Introduction to Quantum Field Theory (Boulder, CO: Westview Press)
Prantzos, N., Hashimoto, M., & Nomoto, K. 1990, A&A, 234, 211
Press, W. H., Teukolsky, S. A., Vetterling, W. T., & Flannery, B. P. 2007, Numerical Recipes (3rd ed.; Cambridge: Cambridge Univ. Press)
Radice, D., Galeazzi, F., Lippuner, J., et al. 2016, MNRAS, 460, 3255
Rauscher, T., & Thielemann, F. 2000, ADNDT, 75, 1
Reddy, S., Prakash, M., & Lattimer, J. M. 1998, PhRvD, 58, 013009
Reichl, L. E. 1980, A Modern Course in Statistical Physics (Austin, TX: Univ. Texas Press)
Roberts, L. F., Kasen, D., Lee, W. H., & Ramirez-Ruiz, E. 2011, ApJL, 736, L21
Roberts, L. F., Lippuner, J., Duez, M. D., et al. 2017, MNRAS, 464, 3907
Roberts, L. F., Woosley, S. E., & Hoffman, R. D. 2010, ApJ, 722, 954
Rolfs, C., & Somorjai, E. 1995, NIMPB, 99, 297
Rolfs, C. E., & Rodney, W. S. 1988, Cauldrons in the Cosmos: Nuclear Astrophysics (Chicago, IL: Univ. Chicago Press)

Salpeter, E. E. 1954, AuJPh, 7, 373
Schatz, H. 2013, IJMSp, 349, 181
Schatz, H. 2016, JPhG, 43, 064001
Schatz, H., Aprahamian, A., Barnard, V., et al. 2001, PhRvL, 86, 3471
Schenk, O., & Gärtner, K. 2004, Future Generation Computer Systems, 20, 475
Schenk, O., & Gärtner, K. 2006, Electronic Transactions on Numerical Analysis, 23, 158
Seitenzahl, I. R., Ciaraldi-Schoolmann, F., Röpke, F. K., et al. 2013, MNRAS, 429, 1156
Seitenzahl, I. R., Townsley, D. M., Peng, F., & Truran, J. W. 2009, ADNDT, 95, 96
Shaviv, G., & Shaviv, N. J. 2000, ApJ, 529, 1054
Shaviv, N. J., & Shaviv, G. 1996, ApJ, 468, 433
Siegel, D. M., & Metzger, B. D. 2017, arXiv:1705.05473
Starrfield, S., Iliadis, C., & Hix, W. R. 2016, PASP, 128, 051001
Strohmayer, T. E., & Brown, E. F. 2002, ApJ, 566, 1045
Surman, R., McLaughlin, G. C., & Hix, W. R. 2006, ApJ, 643, 1057
Surman, R., McLaughlin, G. C., Ruffert, M., Janka, H.-T., & Hix, W. R. 2008, ApJL, 679, L117
Thielemann, F.-K., Arcones, A., Käppeli, R., et al. 2011, PrPNP, 66, 346
Thielemann, F.-K., Nomoto, K., & Hashimoto, M.-A. 1996, ApJ, 460, 408
Thielemann, F.-K., Nomoto, K., & Yokoi, K. 1986a, A&A, 158, 17
Thielemann, F.-K., Truran, J. W., & Arnould, M. 1986b, in Proc. Second IAP Workshop, Advances in Nuclear Astrophysics, ed. E. Vangioni-Flam et al. (Gif-sur-Yvette: Editions Frontieres), 525
Timmes, F. X. 1999, ApJS, 124, 241
Timmes, F. X., & Arnett, D. 1999, ApJS, 125, 277
Timmes, F. X., Hoffman, R. D., & Woosley, S. E. 2000, ApJS, 129, 377
Timmes, F. X., & Swesty, F. D. 2000, ApJS, 126, 501
Truran, J. W., Arnett, W. D., & Cameron, A. G. W. 1967, CaJPh, 45, 2315
Truran, J. W., Cameron, A. G. W., & Gilbert, A. 1966, CaJPh, 44, 563
Vlasov, A. D., Metzger, B. D., Lippuner, J., Roberts, L. F., & Thompson, T. A. 2017, MNRAS, 468, 1522
Wagoner, R. V. 1973, ApJ, 179, 343
Wanajo, S. 2013, ApJL, 770, L22
Wanajo, S., Sekiguchi, Y., Nishimura, N., et al. 2014, ApJL, 789, L39
Weaver, T. A., Zimmerman, G. B., & Woosley, S. E. 1978, ApJ, 225, 1021
Weiss, A., & Truran, J. W. 1990, A&A, 238, 178
Winteler, C. 2013, PhD thesis, Univ. Basel
Winteler, C., Käppeli, R., Perego, A., et al. 2012, ApJL, 750, L22
Woosley, S. E., Arnett, W. D., & Clayton, D. D. 1973, ApJS, 26, 231
Woosley, S. E., Fowler, W. A., Holmes, J. A., & Zimmerman, B. A. 1978, ADNDT, 22, 371
Woosley, S. E., Heger, A., Cumming, A., et al. 2004, ApJS, 151, 75
Woosley, S. E., Heger, A., & Weaver, T. A. 2002, RvMP, 74, 1015
Woosley, S. E., & Hoffman, R. D. 1992, ApJ, 395, 202
Yakovlev, D. G., Gasques, L. R., Afanasjev, A. V., Beard, M., & Wiescher, M. 2006, PhRvC, 74, 035803